EFFECT OF MANGANESE OXIDE DOPANT AND SINTERING ON THE PROPERTIES OF SCANDIA STABILIZED ZIRCONIA

NG CHUI KIM

FACULTY OF ENGINEERING
UNIVERSITY OF MALAYA
KUALA LUMPUR

2018

EFFECT OF MANGANESE OXIDE DOPANT AND SINTERING ON THE PROPERTIES OF SCANDIA STABILIZED ZIRCONIA

NG CHUI KIM

THESIS SUBMITTED IN FULFILMENT OF THE REQUIREMENTS FOR THE DEGREE OF DOCTOR OF PHILOSOPHY

FACULTY OF ENGINERING
UNIVERSITY OF MALAYA
KUALA LUMPUR

2018

UNIVERSITY OF MALAYA

ORIGINAL LITERARY WORK DECLARATION

Name of Candidate: **NG CHUI KIM** [redacted]

Registration/Matric No: **KHA120128**

Name of Degree: **Doctor of Philosophy**

Title of Project Paper/Research Report/Dissertation/Thesis ("this Work"): **Effect of manganese oxide dopant and sintering on the properties of scandia stabilized zirconia.**

Field of Study: **Materials and Manufacturing Processes**

I do solemnly and sincerely declare that:

(1) I am the sole author/writer of this Work;
(2) This Work is original;
(3) Any use of any work in which copyright exists was done by way of fair dealing and for permitted purposes and any excerpt or extract from, or reference to or reproduction of any copyright work has been disclosed expressly and sufficiently and the title of the Work and its authorship have been acknowledged in this Work;
(4) I do not have any actual knowledge nor do I ought reasonably to know that the making of this work constitutes an infringement of any copyright work;
(5) I hereby assign all and every rights in the copyright to this Work to the University of Malaya ("UM"), who henceforth shall be owner of the copyright in this Work and that any reproduction or use in any form or by any means whatsoever is prohibited without the written consent of UM having been first had and obtained;
(6) I am fully aware that if in the course of making this Work I have infringed any copyright whether intentionally or otherwise, I may be subject to legal action or any other action as may be determined by UM.

Candidate's Signature Date:

Subscribed and solemnly declared before,

Witness's Signature Date:

Name:

Designation:

ABSTRACT

Oxide ion conductors have important applications in oxygen sensors, pumps and SOFCs. The best-known oxide ion conductor is stabilized zirconia with exclusive ionic conductivity at elevated temperature. An understanding of the impact from the use of dopant on the zirconia ceramic is critical for tailoring the fabrication and high temperature operational stability of these devices. The conventional sintering method is time and energy consuming, in contrast to traditional approaches to heat transfer based on radiation and convection, rapid microwave heating allows volumetric heating, thus a potential alternative sintering route to provide accelerated densification with limited grain growth.

This research work investigated the effect of manganese oxide (MnO_2) dopant and sintering on the properties of ceria-doped scandia stabilized zirconia (10Sc1CeSZ). Commercially available 10Sc1CeSZ ceramic powder was compared with the powder synthesized via solid state sonication-ball milling method. The results showed that all 10Sc1CeSZ sintered compacts prepared from commercial powder had pure cubic phase, with better resulting mechanical and electrical performance compared to synthesized powder. The effect of MnO_2 additions on the properties of 10Sc1CeSZ was investigated and the results showed that the addition up to 1 wt% had negligible effect on the mechanical properties of the ceramic. The samples containing up to 1 wt% MnO_2 attained above 97.5 % relative density, Vickers hardness of 13-14 GPa and fracture toughness of ~3 $MPam^{1/2}$. In addition, it was revealed that the 0.5 wt% MnO_2 addition was beneficial in suppressing the cubic zirconia grain growth i.e. the highest average grain size was measured at 4.9 μm when sintered at 1550 °C as compared to 9.9 μm measured for the undoped zirconia when sintered at the same temperature. On the other hand, the addition of 5 wt% MnO_2 was found to be detrimental to the densification and

properties of the zirconia, particularly when sintered at higher temperatures. This was attributed to the accelerated grain growth of the doped samples, i.e. the grain size increased by twofold, to 18.6 μm when sintered at 1550 °C. In addition, the influence of rapid sintering via microwave technique at low temperature regimes of 1300 °C and 1350 °C for 15 minutes on the properties of undoped 10Sc1CeSZ was evaluated. It was found that both sintering processes yielded highly dense samples with a minimum theoretical density of 97.5%. All sintered pellets had pure cubic phase and possessed high Vickers hardness (13-14.6 GPa) and fracture toughness (~3 $MPam^{1/2}$). SEM microstructures revealed that the grain size varied from 2.9-9.9 μm for the conventional-sintered samples. In comparison, the grain size of the microwave-sintered zirconia was maintained below 2 μm. EIS study showed that both the bulk and grain boundary resistivity of the zirconia decreases with increasing test temperature regardless of sintering methods. However, the grain boundary resistivity of the microwave-sintered samples was higher than the conventional-sintered ceramic at 600 °C and reduced significantly at 800 °C thus resulting in the enhancement of electrical conduction. A sintering mechanism involving preferential grain boundary local heating was proposed for enhanced densification and the resulting sintering properties of the zirconia ceramic. MnO_2 was found to be as an effective additive to scavenge siliceous phase at the grain boundary.

ABSTRAK

Konduktor ion oksida mempunyai aplikasi penting dalam sensor oksigen, pam dan SOFCs. Konduktor ion oksida yang paling terkenal adalah stabil zirkonia dengan kekonduksian ionik eksklusif pada suhu tinggi. Pemahaman tentang kesan daripada penggunaan pendopan pada seramik zirconia adalah kritikal untuk melaraskan pembuatan dan kestabilan operasi suhu tinggi untuk alat-alat ini. Cara pembakaran konvensional adalah satu proses yang memakan masa dan tenaga, berbeza dengan pembakaran tradisional yang melibatkan haba pemindahan berdasarkan radiasi dan perolakan, pemanasan gelombang mikro pesat membolehkan pemanasan isipadu, dengan itu adalah proses pensinteran alternatif yang berpotensi untuk memberikan pemadatan pesat dengan pertumbuhan bijian terhad.

Kerja penyelidikan ini menyiasat kesan pendopanan oksida mangan (MnO_2) dan pensinteran kepada sifat-sifat ceria-scandia stabil zirconia (10Sc1CeSZ). Serbuk komersial 10Sc1CeSZ seramik telah dibandingkan dengan serbuk yang disintesis melalui kaedah sonication-bola pengilangan. Hasil kajian menunjukkan bahawa semua 10Sc1CeSZ kompak tersinter yang disediakan daripada serbuk komersial mempunyai fasa padu tulen, dan mengakibatkan prestasi mekanikal dan elektrik yang lebih baik berbanding dengan serbuk yang disintesis. Kesan penambahan MnO_2 kepada sifat-sifat 10Sc1CeSZ telah disiasat dan keputusan menunjukkan bahawa penambahan sehingga 1wt% mempunyai kesan yang boleh diabaikan pada sifat-sifat mekanikal seramik. Sampel yang mengandungi sehingga 1wt% MnO_2 mencapai lebih dari 97.5% ketumpatan relatif, Vickers kekerasan 13-14 GPa dan patah keliatan ~3 $MPam^{1/2}$. Di samping itu, ia telah mendedahkan bahawa penambahan 0.5wt% MnO_2 adalah bermanfaat dalam menghalang pertumbuhan bijirin padu zirconia dengan saiz butiran purata tertinggi diukur pada 4.9 μm apabila disinter pada 1550°C, berbanding dengan

9.9 μm yang diukur untuk undoped zirkonia apabila disinter pada suhu yang sama. Sebaliknya, penambahan 5wt% MnO_2 didapati memudaratkan pemadatan dan sifat-sifat zirconia, terutamanya apabila disinter pada suhu yang lebih tinggi. Ini disebabkan oleh pertumbuhan bijian dipercepatkan bagi sampel yang dicampurkan dengan dopan, iaitu saiz butiran meningkat sebanyak 2 kali ganda, mencapai 18.6μm apabila disinter pada 1550°C. Di samping itu, pengaruh pensinteran pesat melalui teknik ketuhar gelombang mikro pada rejim suhu rendah 1300°C dan 1350°C selama 15 minit kepada sifat undoped 10Sc1CeSZ telah dinilai. Ia telah mendapati bahawa kedua-dua proses pensinteran menghasilkan sampel yang sangat padat dengan kepadatan teori minimum 97.5%. Semua pelet tersinter mempunyai fasa padu tulen dan mempunyai kekerasan yang tinggi Vickers (13-14.6 GPa) dan keliatan patah (~3 $MPam^{1/2}$). SEM mikrostruktur mendedahkan bahawa saiz butiran berbeza dari 2.9 kepada 9.9 μm bagi sampel konvensional-tersinter. Sebagai perbandingan, saiz bijian zirkonia gelombang mikro tersinter itu dikekalkan di bawah 2 μm. Kajian EIS menunjukkan bahawa kedua-dua kerintangan pukal dan sempadan bijian zirconia berkurangan dengan peningkatan suhu ujian untuk kedua-dua kaedah pensinteran. Walau bagaimanapun, kerintangan sempadan bijian untuk sampel tersinter gelombang mikro adalah lebih tinggi daripada seramik konvensional-tersinter di 600°C dan dikurangkan dengan ketara di 800°C sehingga mengakibatkan peningkatan pengaliran elektrik. Satu mekanisme pensinteran melibatkan keutamaan bijirin pemanasan tempatan sempadan telah dicadangkan untuk peningkatan pemadatan dan sifat-sifat pensinteran terhasil daripada seramik zirconia itu. MnO_2 didapati sebagai bahan tambahan yang berkesan untuk menghapuskan sisa fasa bersilika di sempadan bijian.

ACKNOWLEDGEMENTS

First and foremost, I would like to express my profound gratitude to my supervisors, Professor Ir. Dr. Ramesh Singh and Associate Professor Ir. Dr. Tan Chou Yong for giving me the opportunity to pursue PhD study under their guidance. I am deeply indebted to both of my supervisors for their enormous help and support throughout my PhD research journey in the University of Malaya. It is a big honour to be able to work with them, who have contributed significantly in the field of advanced ceramics.

I am deeply grateful to Professor Andanastuti Muchtar and the associates working in the Institute of Fuel cell, Universiti Kebangsaan Malaysia (UKM), who have given me the maximum convenience and help on the experimental and electrical testing work in the SOFC laboratory. Special thanks to Dr. Mahendra Rao Somalu and Mr. Muhammed Ali S.A. who assisted in the data analysis of the electrical conductivity measurement.

I would also like to thank the faculty, staffs and students at the Centre of Advanced Manufacturing and Material Processing (AMMP), especially Dr. Ali Asghar Niakan and Dr. Kelvin Chew Wai Jin, Dr. Tan Yoke Meng, Dr. Sutharsini Ubenthiran, Dr. Teh Yee Ching, and Mr. Chong Feng Duan, for their invaluable assistances during the course of my study.

I am also grateful for the financial support provided by the Ministry of Science, Technology & Innovation, University of Malaya, and Tunku Abdul Rahman University College which enabled me to complete my work.

Finally, I would like to extend my utmost gratitude to my parents, my husband, and all of my family members and friends for their help, tremendous support, continuous encouragement and patience during the years of my study.

TABLE OF CONTENTS

LIST OF FIGURES

LIST OF TABLES

LIST OF SYMBOLS AND ABBREVIATIONS

3Y-TZP		3 mol% yttria stabilized zirconia
10ScSZ	:	10 mol% scandia stabilized zirconia
10Sc1CeSZ	:	1 mol% ceria-10 mol% scandia stabilized zirconia
AFC	:	Alkaline fuel cell
CaSZ	:	Calcia-stabilized zirconia
CGO	:	Gadolinia-doped ceria
CSO	:	Samarium doped ceria
DKKK	:	Daiichi Kigenso Kagaku Kogyo
DMFC	:	Direct methanol fuel cell
EIS	:	Electrochemical Impedance Spectroscopy
GNP	:	Graphene platelet
HDPE	:	High density polyethylene
IT-SOFC	:	Intermediate temperature- solid oxide fuel cell
KOH	:	Potassium hydroxide
LSGM	:	Strontium and magnesium doped lanthanum gallate
MCFC	:	Molten carbonate fuel cell
NO_x	:	Nitrogen oxide
PAFC	:	Phosphoric acid fuel cell
PECS	:	Pulsed electric current sintering
PEMFC	:	Polymeric electrolyte membrane fuel cell
PSZ	:	Partially-stabilized zirconia
ScSZ	:	Scandia stabilized zirconia
SDC	:	Samaria-doped ceria
SOFC	:	Solid oxide fuel cell

SPS	:	Spark plasma sintering
SO_x	:	Sulphur oxide
WC	:	Tungsten carbide
YSZ	:	Yttria-stabilized zirconia

LIST OF APPENDICES

CHAPTER 1: INTRODUCTION

1.1 General Introduction

Current energy supply systems are mainly based on the combustion of fossil fuels (Biresselioglu & Yelkenci, 2016). The environmental problems caused by burning of fossil fuels include acid gas emissions, air quality deterioration, and global warming. In order to conserve energy resources and reduce CO_2 emission into the atmosphere, efforts have been focused on developing highly efficient electricity generation and transportation technology.

In a fuel cell, the chemical energy is directly converted to electrical energy from a variety of fuels such as natural gas or hydrogen. In comparison to conventional combustion technology, fuel cells produce no emissions of nitrogen oxide (NO_x), sulfur oxide (SO_x), or hydrocarbon pollutants (Stambouli & Traversa, 2002). It can achieve high system efficiency in excess of 50 % from direct chemical to electrical energy conversion and up to 90 % with heat recovery (Badwal, 2001).

Fuel cells appear to be one of the promising alternative energy conversion devices to generate sustainable electric power, in which the hydrogen can be produced from a renewable energy source, through the use of solar panel, a wind turbine or a hydroelectric turbine (Cook, 2002). It can provide energy for rural areas without the need of transporting electricity through transmission lines, therefore obviates the need for electrical grids in remote locations (Mekhilef et al., 2012).

A fuel cell consists of three main components, a fuel electrode (anode), an oxidant electrode (cathode), and an electrolyte. Fuel cells generate electricity and heat through the electrochemical reaction of converting hydrogen and oxygen into water, which is actually a reversed electrolysis reaction (Cha et al., 2006).

Overall reaction: 2 H_2 (gas) + O_2 (gas) → 2 H_2O + energy (1.1)

Fuel cell can be categorized into six different groups depending on the choice of fuel and electrolyte (Perry & Fuller, 2002; Kirubakaran et al., 2009):

i) Proton electrolyte membrane fuel cell (PEMFC)

ii) Alkaline fuel cell (AFC)

iii) Direct methanol fuel cell (DMFC),

iv) Phosphoric acid fuel cell (PAFC)

v) Molten carbonate fuel cell (MCFC)

vi) Solid oxide fuel cell (SOFC)

These fuel cells operate at different temperatures. PEMFC (~100 °C), AFC, DMFC and PAFC (~ 200 °C) were developed at lower temperatures, while MCFC (~650 °C) and SOFC (800 °C ~ 1000 °C) operate at elevated temperatures (Kirubakaran et al., 2009). The high temperature operation of MCFC and SOFC made the internal reforming of the fuel within the fuel cell possible and reduces the complexity of the system. This will increase the efficiency compared to the lower temperature variants.

Solid Oxide Fuel Cell (SOFC) is the most efficient high temperature fuel cell electrical generator that can run on a variety of fuels, from hydrogen to hydrocarbon. It uses metal oxide solid ceramic electrolytes to allow the transport of oxygen vacancy (O^{2-}) from the cathode to the anode. The O^{2-} ionic conduction requirement for the ceramic electrolyte necessitates high operating temperatures (800- 1000 °C) to ensure adequate ionic conduction in the electrolyte (Mahato et al., 2015). The high temperature operating environment promote fast reaction kinetics, therefore does not require the use of noble metal that could limit the applicability of SOFC due to the scarcity of resources

and high price issue in mass production (Stambouli & Traversa, 2002). It also allows reforming of hydrocarbon (CO, CH_4, gasoline, etc.) fuels within the fuel cell.

There is worldwide interest in the development and commercialization of fuel cells for vehicles and portable electric devices. Transportation applications require fuel cells to have lower operating temperature with higher mechanical and thermal shock resistance (Gao et al., 2010).

1.2 Problem statement

High temperature SOFC operation makes great demands on materials and requires very careful selection on issues concerning sealing of the cells, compatibility of thermomechanical properties between electrolyte and electrode, and stability of individual components (Barsoukov & Macdonald, 2005; Orera & Slater, 2009). In order to reduce manufacture cost and improve long-term stability of SOFCs, reduction of the operating temperature of SOFCs to an intermediate temperature range of 600–800 ^{o}C is found to be an effective approach, especially for transportation application. As a result, recent development emphasis has been on improving material property or modifying processing routes to reduce the working temperature of the electrolyte material.

The solid oxide electrolyte is one central component that determines the operational characteristics of the fuel cell systems (Figueiredo & Marques, 2013). Therefore, one of the effective approaches to lower the operating temperature of SOFC is to adopt electrolyte materials of high oxygen-vacancy concentration, thus high ionic conductivity. This would subsequently reduce the cost by allowing the use of cheaper interconnectors, gas manifolds, and sealant materials.

Strontium and magnesium doped lanthanum gallate (LSGM) and ceria based electrolytes have been shown to exhibit high ionic conductivity, but are found to have inferior chemical stability in reducing environments (Fergus, 2006). Zirconia based ceramics doped with lower valence metal oxide (divalent or trivalent metal oxides) has high ionic conductivity, high mechanical and chemical stability, compatibility towards other components used in the SOFC and with lower electronic conductivity in oxidizing environment, thus offer the best possible choice as SOFC electrolyte.

However, the works on the most widely used yttria stabilized zirconia (YSZ) show that power density decreases quickly with decreasing temperatures. To obtain a SOFC operating at or lower than 700 °C, there is a clear need to replace yttria with a different stabilizer that possesses higher ionic conductivity at low temperatures. Literature has reported a promising, although less widely used stabilizer for zirconia is scandia, which has higher ionic conductivity than YSZ (Badwal & Foger, 1996; Singhal, 2000).

The ionic conductivity of scandia stabilized zirconia (ScSZ) is twice that of YSZ due to similar ionic radius of Sc^{3+} (0.087 nm) and Zr^{4+} (0.084 nm) that leads to lower internal stress and lower activation energy, and hence results in 100 K lower operating temperatures for a comparable conductivity (Haering et al., 2005). Co-doping of ScSZ with small amount of other oxides such as 3 mol% ytterbium oxide (Chiba et al., 1996), 1- 2 mol% bismuth oxide (Hirano et al., 2003; Sarat et al, 2006; Bai et al., 2008), 3 mol% iron oxide (Bohnke et al., 2014), 1 mol% dysprosium oxide (Grosso et al., 2016), and in particular 0.5-1 mol% ceria (Lee et al., 2005; Kumar et al., 2016), resulted in improved phase stability and enhanced electrical performance.

Processing techniques can greatly influence the mechanical and electrical properties of zirconia ceramics and importantly the sintering methods adopted for microstructural control and densification play an important role. The conventional sintering often

requires long duration of holding time at high temperatures for the removal of residual pores, often produced zirconia ceramics with coarse-grained structures thereby adversely affecting the sintering properties (Rajeswari et al., 2010). More efforts in the low temperature accelerated sintering are imperative to make the electrolyte fabrication process feasible in large scale SOFC production.

Conventional heating requires the heat to be transferred from the surface to the core of the material whereas microwave sintering resulted in volumetric heating and thereby a promising technique for uniform and fast firing of the ceramic. It involves the absorption of microwave field to cause molecular vibrations and generates heat through direct electromagnetic to thermal energy conversion (Sutton, 1989; Agrawal, 2006; West, 2007). Previous studies on microwave sintering of various types of ceramics such as hydroxyapatite (Nath et al., 2006), alumina (Lefeuvre et al., 2010), zirconium phosphate (Dey et al., 2013), 3Y-TZP (Kim et al., 2013), and YSZ (Mazaheri et al., 2009; Rajeswari et al., 2010; Thridandapani et al., 2015; Singh et al., 2016) showed promising results in terms of enhancing densification and homogeneity at lower temperatures or shorter holding times. The use of the microwave systems allowed reducing the length of the sintering cycle to a few minutes, compared to several hours necessary with a traditional heating system. This implies that microwave sintering is the prospective energy saving alternative in processing of ceramics.

One of the main limitations of oxide ion conductors as SOFC electrolytes is the undesirable phase transformation caused by impurities. It is reported that phase destabilization induced by manganese, boron, or silicon was observed in calcia/ yttria stabilized zirconia (Beekmans & Heyne, 1976; De Florio & Muccillo, 2004; Kishimoto et al., 2009; Mahapatra et al., 2012). The manganese diffusion from the cathode took place during the heat treatment of cell fabrication in air; other impurities were found to

be transferred from other components or processing equipment (Shimazu et al., 2011; Mahapatra et al., 2012). These impurities were found to react with the stabilizers, leading to cubic phase destabilization and phase transformation into tetragonal symmetry. It is therefore necessary to investigate the reactions between electrolyte material and minor impurities.

1.3 Objectives of the research

The objectives of present research are as follows:

1. To investigate and compare the mechanical and electrical properties of synthesized compact produced via solid state synthesis method and commercially available scandia stabilized zirconia ceramic.
2. To examine the effect of manganese oxide doping on the sintering properties of scandia stabilized zirconia ceramic.
3. To evaluate the microwave sintering behavior of undoped and MnO_2-doped scandia stabilized zirconia ceramic relative to conventional pressureless sintering.

1.4 Scope of the research

The aims of this present work are two folds. Firstly, the experimental work was carried out to compare the sintering properties of synthesized and commercial 1 mol% ceria-doped 10 mol% scandia stabilized zirconia (10Sc1CeSZ) powders. The synthesized zirconia ceramic powder was prepared by solid state route using sonication and milling process. Subsequently, powder that provided better properties would be studied further. The influence of additions of different amount of manganese oxide

(MnO_2) dopant on the densification, phase stability and mechanical properties of the 10Sc1CeSZ ceramic was then investigated.

Secondly, the influence of rapid microwave heating process at low sintering temperature on the densification and microstructure development of the undoped and MnO_2-doped 10Sc1CeSZ zirconia ceramics were investigated, and the associated mechanical properties and electrical conductivities were evaluated for potential use as electrolyte material in Intermediate-Temperature SOFC (IT-SOFC).

Hence, in summary, the ultimate goal of the research is to produce a dense scandia stabilized zirconia ceramic with high mechanical properties and electrical conductivity that are suitable for use as electrolyte in IT- SOFC application.

1.5 Structure of the thesis

Chapter 1 consists of an introduction to the thesis objectives and background information on the area of fuel cells, doping effect and sintering methods.

Chapter 2 provides an insight on the types of fuel cell, progress on the materials used in SOFCs, followed by a detail study on the previous works that have been performed on the technical challenges of the processing of SOFC, the influence of different types of dopants and sintering techniques for oxide ion conductors for IT-SOFC.

Chapter 3 presents detailed information on experimental methods adopted for this research and elaborates the equipment and materials used in this work.

The results obtained from this study are discussed in Chapter 4, which includes evaluation on the effect of dopants and sintering on the mechanical and ionic property of scandia stabilized zirconia ceramics.

Finally, in chapter 5, this thesis concludes the current research findings, in light of the various areas of investigation undertaken in this thesis; and some suggestions for future work.

CHAPTER 2: LITERATURE REVIEW

2.1 Introduction to Fuel Cells

In recent decades, research has intensified to develop commercially viable fuel cells as a cleaner and more efficient source of electricity as tantalizing alternatives to combustion engines, due to geopolitical influence and the increased pressures from the use of fossil fuels on the environment (Haile, 2003).

A fuel cell is an energy conversion device that uses reverse electrolysis reactions to convert chemical energy directly into electrical energy and heat without the need for direct combustion as an intermediate step. They convert hydrogen, or hydrogen containing fuels (H_2, CH_4, natural gas) and oxygen (O_2, air) into water to produce electricity. A fuel cell was first constructed by William Grove and Christian Friedrich in 1839 using two platinum electrodes with a diluted sulfuric acid electrolyte (Grove, 1839).

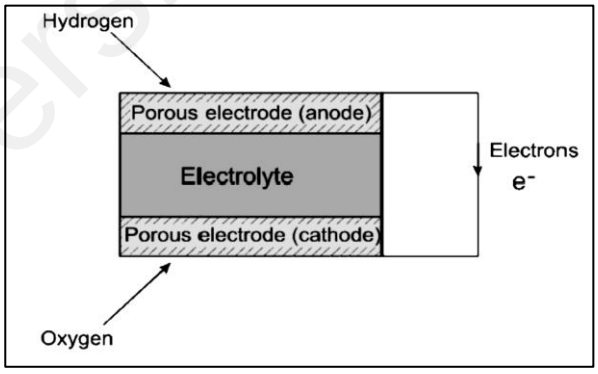

Figure 2.1: Schematic diagram showing the general operating principles of a fuel cell (Ormerod, 2003).

A fuel cell consists of an ion conducting electrolyte, a cathode, and an anode, as shown schematically in Figure 2.1. Hydrogen and oxygen reactants are supplied into the anode and cathode compartments. There is an overall chemical driving force for the

oxygen and the hydrogen to react to produce water. Direct hydrogen-oxygen combustion is prevented by an electrolyte medium that separates the hydrogen and oxygen reactants. The ion conducting, but electronically insulating electrolyte serves as a barrier to gas diffusion, but will let protons or oxide ions migrate across it, while the electron travel round an external circuit, producing electric power (Ormerod, 2003).

The two electrochemical half-cell reactions occur at the anode and cathode for proton conducting electrolyte are:

$$\text{Cathode: } \tfrac{1}{2}O_2 + 2H^+ + 2e^- \rightarrow H_2O \quad (2.1)$$

$$\text{Anode: } H_2 \rightarrow 2H^+ + 2e^- \quad (2.2)$$

The analogous half-cell reactions for ion conducting electrolyte depicted in Figure 2.2 are as follows:

$$\text{Cathode: } \tfrac{1}{2}O_2 + 2e^- \rightarrow O^{2-} \quad (2.3)$$

$$\text{Anode: } H_2 + O^{2-} \rightarrow H_2O + 2e^- \quad (2.4)$$

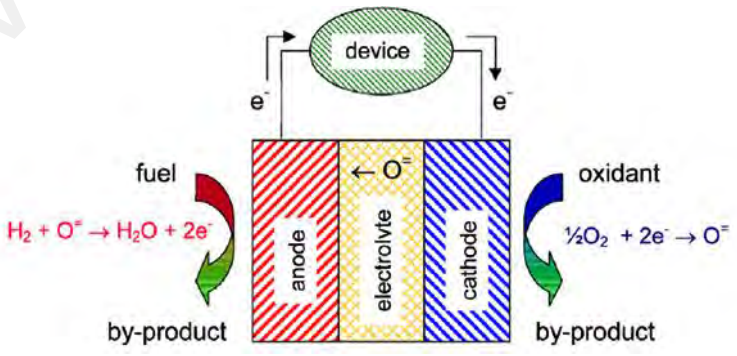

Figure 2.2: Schematic of a fuel cell comprised of an ion conducting electrolyte, an anode and a cathode. The overall chemical reaction is $H_2 + \frac{1}{2}O_2 \rightarrow H_2O$ (Haile, 2003).

A fuel cell has physical components and characteristics that are similar to those of a typical battery, i.e. electrochemical combinations of reactants to generate electricity. Their main difference is a battery will run down or require recharging when the chemical reactants stored within the battery are consumed or discharged, while a fuel cell is able to operate as long as fuel and oxidant are supplied to the electrodes (Behling, 2012).

Fuel cell offers many advantages over traditional energy conversion systems including high conversion efficiency, virtually silent operation and if hydrogen is derived from electrolysis instead of extracted from fossil fuels there are zero pollutant emissions. If the electricity to break water down into hydrogen and oxygen in a electrolysis process uses renewable energy sources such as wind, solar, geothermal, nuclear, or hydropower, then the electrical power produced can be truly sustainable (Cook, 2002; Hoffmann & Dorgan, 2012).

2.2 Types of Fuel Cells

Fuel cells are classified into six major categories based on the choice of electrolyte as presented in Table 2.1, which include alkaline fuel cell (AFC), polymeric electrolyte membrane fuel cell (PEMFC), direct methanol fuel cell (DMFC), phosphoric acid fuel cell (PAFC), molten carbonate fuel cell (MCFC), and solid oxide fuel cell (SOFC).

The type of electrolyte material determines the applicable operating temperature range and the type of migrating ion of a fuel cell. The specific operating characteristics would dictate the types of fuels that can be used in the fuel cell (Revankar & Majumdar, 2014).

Table 2.1: Characteristics of Various Types of Fuel Cell (Kirubakaran et al., 2009; Stambouli & Traversa, 2002).

Type	Fuel	Operating temperature (°C)	Electrolyte	Charge carrier
AFC	Hydrogen	50-200	KOH	OH^-
PEMFC	Hydrogen	70-100	Polymer	H^+
DMFC	Methanol	60-200	Polymer	H^+
PAFC	Hydrogen	200	Phosphoric acid	H^+
MCFC	Hydrocarbon, alcohol	650	Molten carbonate	CO_3^{2-}
SOFC	Hydrocarbon, alcohol	800-1000	Solid oxide	O^{2-}

AFC, PEMFC, DMFC and PAFC are the fuel cells that could operate in the temperature range of 50- 200°C, which is considerable low compared to the MCFCs and SOFCs that operate in the temperature range of 650-1000°C (Kirubakaran et al., 2009). Fuel cells that have low operating temperature require relatively expensive pure hydrogen to be supplied to the anode. The cost and complexity of the system would be increased with the need to use an external reformer to convert hydrocarbon or alcohol fuels to hydrogen (Steele & Heinzel, 2001).

In contrast, high-temperature fuel cells such as MCFCs and SOFCs are attractive because they do not need expensive noble metal catalysts and could use a wide range of fuels. It also produces high exhaust gas temperature, which greatly enhance the system efficiencies of the fuel cell system with the ability to cogenerate heat and electric power (Revankar & Majumdar, 2014). The main disadvantage of MCFC is that the electrolyte which consists of a mixture of carbonates such as potassium carbonates (K_2CO_3) and lithium carbonates (Li_2CO_3) have low melting temperature of about 500 °C and are very corrosive. The corrosive and volatile species in the electrolyte adversely impacts the fuel cell life (Holland et al., 2007, Revankar & Majumdar, 2014).

2.3 Solid Oxide Fuel Cell (SOFC)

2.3.1 Introduction to SOFC

Among the possible fuel cell types, it is generally believed that SOFCs hold the most promise for future medium and large power applications (Kirubakaran et al., 2009).

SOFCs are the only fuel cells that use a solid electrolyte, and therefore this will solve the electrolyte-management problems presented with other fuel cell types (Perry & Fuller, 2002). SOFCs offer clean and pollution free operation as with other fuel cells, with the exceptional fuel flexibility which can operate on multiple fuels, including natural gas fuel. Owing to the utilization of high operating temperatures, it is possible to reach power production efficiency of 60 % for single cycle and up to 90 % efficiency for total systems (Badwal, 2001).

Table 2.2: Comparison of emission from SOFC and conventional power generation (Hart et al., 2000)

Emission	SOFC (g/kWh)	Conventional (g/kWh)	Reduction in emissions through the use of an SOFC system (g/kWh)
CO_2	623	794	171
CO	0.038	0.43	0.392
NMHC	0.16	0.19	0.03
CH_4	0.43	0.57	0.14
NO_X	0.078	1.02	0.942
SO_X	0.016	0.33	0.314
PM	0.0093	0.01	0.0007

Table 2.2 summarizes the emission produced from a SOFC unit and a conventional power generation system. The result shows that SOFC system emits low levels of pollutants. The emissions of CO, NO_x, and SO_x were reduced by more than one order of

magnitude, while non-methane hydrocarbon (NMHC), methane, CO_2, and particulate matter (PM) were reduced by 7- 25%, as compared to conventional technology.

A SOFC consists of a dense, oxygen ion conducting electrolyte sandwiched between two porous electrodes, with planar or tubular geometries in stack designs, as illustrated in Figure 2.3.

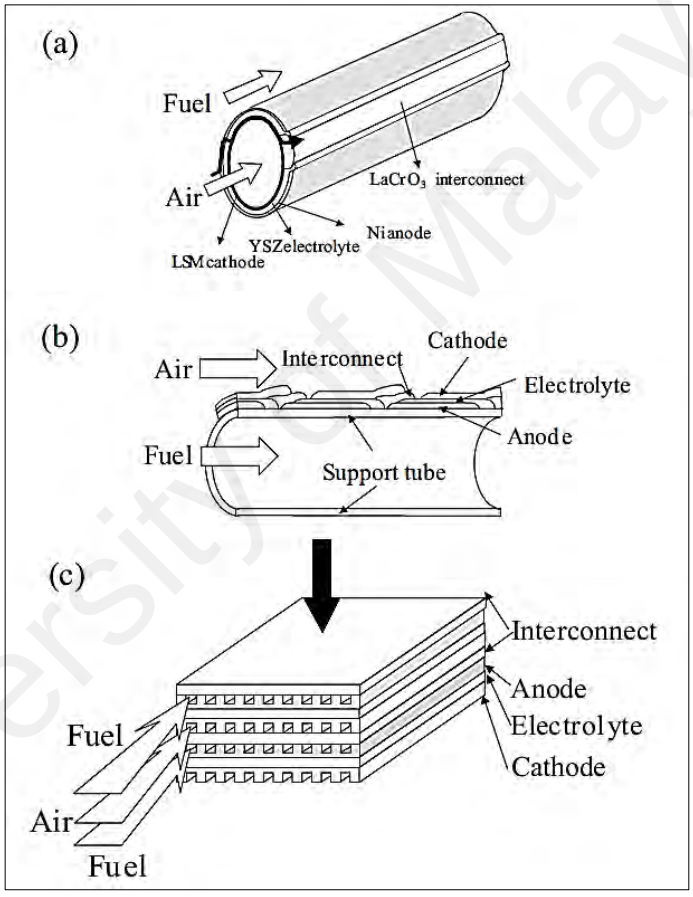

Figure 2.3: **Schematic view of tubular and planar SOFC stacks, materials, and mass flow. (a) Tubular (b) Segment-type tubular (c) Planar (co-flow type), counter-flow-type or cross flow-type planar stacks are not shown for simplicity (Yokokawa et al., 2001).**

The conventional SOFCs are generally operated at high temperatures (> 800 °C) due to the poor ionic conductivity of electrolytes. However, such high operating temperature

causes material degradation problems in the other cell components, such as the hermetic seals and interconnects, thereby obstructing the full commercialization of SOFCs. (Charpentier et al., 2000; Badwal, 2001; Wincewicz & Cooper, 2005).

To compensate for the poor ionic conductivity at intermediate temperatures, and to a strong cathode polarization, different approaches considered include the development of better electrolyte and electrode materials, besides reducing the thickness of electrolytes (Charpentier et al., 2000; Singhal & Kendall, 2003; Sun & Stimming, 2007; Sun et al., 2010).

2.3.2 Material requirements for SOFC components

The materials for different cell components in SOFCs have their specific electrical, chemical, and thermal requirements. Cathode and anode must be of porous structure with high electronic conductivity while electrolyte is of dense structure with high ionic conductivity. All the components must have adequate chemical and structural stability at high temperatures during SOFC fabrication or operation, and have matching thermal expansion among different SOFC components (Singhal, 2000).

Figure 2.4 shows the cross-section of a Siemens Westinghouse SOFC, in which different level of porosity of the two electrodes and the electrolyte can been seen clearly.

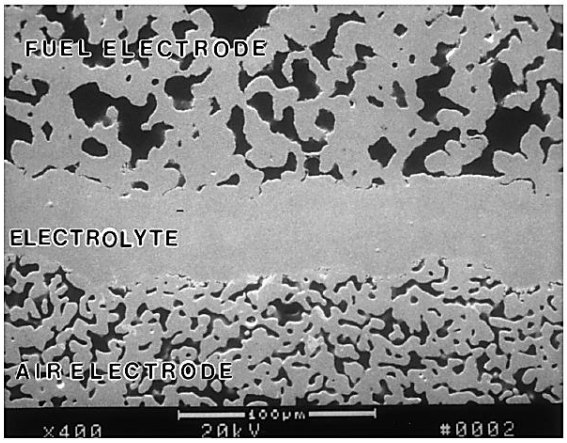

Figure 2.4: **Microstructure of a cross-section of Siemens Westinghouse SOFC (Singhal, 2000)**

2.4 Solid electrolyte materials

The solid electrolyte is one central component that determines the operational temperature of the fuel cell. The function of the electrolyte in a SOFC is for conducting ions between the electrodes, for the separation of the reacting gases and for the internal electronic conduction blocking, forcing the electrons to flow through the external circuit.

Design of new electrolytes includes manipulation of ionic defects concentration and mobility, ionic transport of point defects in various types of structures, dislocations, grain boundaries, and heterostructure interfaces (Figueiredo & Marques, 2013).

There are three types of electrolytes that differ by the ion transport mechanism: anionic, protonic and mixed ionic. However, most of the high temperature fuel cells operate via oxygen ion (O^{2-}) conduction from the air electrode to the fuel electrode. This conduction occurs because of the presence of oxygen ions vacancies, so the material requirements for electrolytes to be used in SOFC must have unoccupied anionic sites in the crystallites. The energy required for the oxide ion migration from one site to the neighbouring unoccupied equivalent site must be small (Taroco et al., 2011).

The following summarize the required properties of the electrolyte materials for SOFC (Singhal & Kendall, 2003; Goodenough, 2003; Revankar & Majumdar, 2014):

(1) High oxide-ion conductivity (0.01 $S.cm^{-1}$ at operating temperature).

(2) Low electronic conductivity to prevent high voltage loss and oxygen leakage.

(3) High density to avoid gases from permeating from one side of the electrolyte to the other side.

(4) Thermodynamic stability over a wide range of temperatures and oxygen partial pressure.

(5) Compatible coefficient of expansion with adjoining electrodes and other cell components from ambient temperature to cell operating temperature.

(6) Reliable mechanical properties, with fracture resistance greater than 400 MPa at room temperature.

(7) Negligible chemical interaction with electrode materials both during processing and service to avoid formation of blocking interface phases.

(8) Good sinterability for their applications as gas tight membranes for very thin thickness.

On the basic of these requirements, three electrolyte systems namely zirconia and ceria fluorites, and lanthanum gallate ($LaGaO_3$)-based perovskites have been widely investigated for SOFCs. These materials allow the formation of anion vacancies by aliovalent doping. Several popular electrolyte materials investigated including yttria stabilized zirconia (YSZ), gadolinium- or samarium doped ceria (CGO or CSO), and magnesium-doped lanthanum gallate (LGSM) (Jacobson, 2009).

2.4.1 Zirconia-based electrolytes

Stabilized zirconia ceramic, which has the fluorite-type structure as shown in Figure 2.5, was first experimented in a fuel cell by Baur & Preis (1937), although it had previously been employed as the electrolyte in the Nernst-lamp (Nernst, 1901). The oxygen vacancies generated when trivalent rare earths or divalent alkaline earth metals are introduced into the host material, not only stabilizes the cubic fluorite phase, but also enhances its ionic conductivity (Orera & Slater, 2009).

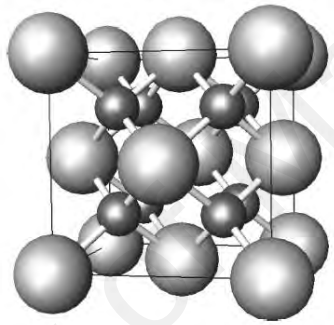

Figure 2.5: Fluorite structure adopted by stabilized ZrO_2 and CeO_2 (large spheres= Zr/Ce, small spheres=O) (Orera & Slater, 2009).

One oxygen vacancy is created for every one mole of trivalent yttria dopant incorporated. The defect formation reaction expressed in Kroger-Vink notation as (Singhal, 2000):

$$Y_2O_3 \xrightarrow{ZrO_2} 2Y'_{Zr} + 3O^x_o + V_{\ddot{o}} \qquad (2.5)$$

Oxygen-ion transport in the zirconia lattice is via a lattice-hopping mechanism, in which the oxide ions leap from hole to hole due to an oxygen concentration gradient that drive the ion transport from cathode towards anode (Kee et al., 2008).

The conductivity of these solid solutions increases with increasing dopant content and then decreases sharply due to defect interactions or ordering (Kee et al., 2008). The formation of defect associates binds some oxygen vacancies, and thus reduces the mobility of oxygen vacancies, making them unavailable for conduction (Guo, 2003).

In the case of yttria, the optimum dopant concentration is 8 mol % Y_2O_3, with ionic conductivity of approximate 0.01 $S.cm^{-1}$ at 1000 °C. The stabilization of cubic phase of zirconia ceramics with lower valence cations increases the mobile oxygen vacancies, and also prevents polymorphic transformation from cubic to tetragonal and monoclinic crystal structure, which could cause significant volume changes that resulted in mechanical failures in sintered bodies (Figueiredo & Marques, 2013).

Table 2.3 shows the mechanical properties of various solid oxide electrolytes measured with an applied load of 500 mN. The results indicate that 8 mol % yttria stabilized zirconia (YSZ) exhibited higher mechanical properties compared to all 10- 20 mol% gadolinia-doped ceria (GDC) samples, with the mechanical property values of GDC decreased as the gadolina content increased.

Table 2.3: **Young's modulus, E, and hardness, H, fracture toughness, K_{Ic} of YSZ (Y_2O_3 8 mol%) 10 GDC (Gd_2O_3 10 mol%), 15 GDC (Gd_2O_3 15 mol%), 20 GDC (Gd_2O_3 20 mol%) electrolytes with an applied load of 500 mN (adapted from Morales et al., 2010)**

Sample	E (GPa)	H (GPa)	K_{Ic} (MPa $m^{1/2}$)
YSZ	223 ± 7	14.2 ± 0.7	1.79 ± 0.11
10GDC	202 ± 3	11.8 ± 0.5	1.47 ± 0.12
15GDC	192 ± 4	11.1 ± 0.3	1.39 ± 0.11
20GDC	186 ± 3	10.5 ± 0.4	1.27 ± 0.13

Consequently, YSZ has been most successfully employed as the electrolyte for SOFCs. It has excellent properties as an electrolyte, although one major drawback is the necessity of an elevated temperatures of 800-1000 °C for sufficient oxygen ion mobility, with consequent problems in high temperature sealing and thermal mismatch of its cell components (Orera & Slater, 2009).

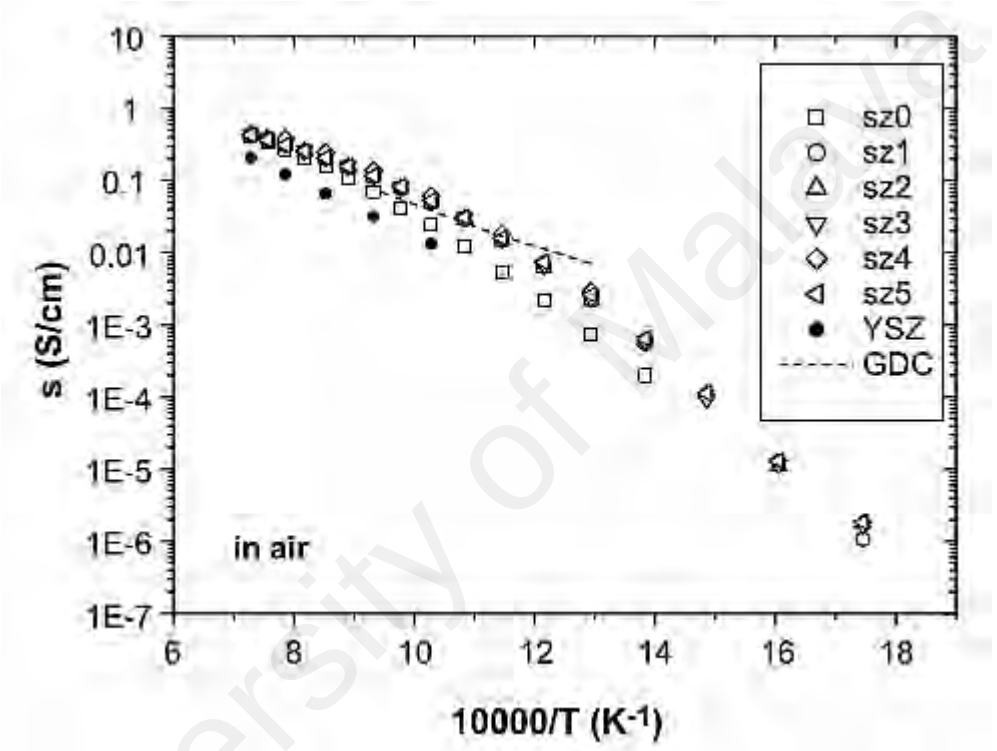

Figure 2.6: Temperature dependence of the electrical conductivity of YSZ (Y_2O_3 8 mol%), GDC (Gd_2O_3 10 mol%) and as-sintered 10Sc1CeSZ samples (SZ0-1250 °C – SZ5-1550 °C) measured by DC four-probe method (Lee et al., 2005).

Scandia stabilized zirconia has the highest ionic conductivity among the zirconia systems, about twice that of the yttria-stabilized zirconia (Badwal, 2001). This can be evidenced in the Arrhenius plot of electrical conductivity depicted in Figure 2.6. The electrical conductivities of all 1 mol% ceria-doped scandia stabilized zirconia (SZ) samples were higher than the 8 mol% yttria-stabilized zirconia (YSZ) at all sintering temperature ranges, which has conductivity comparable to the Gadolinium doped

ceria (GDC), which is known to be the strong candidate material for intermediate or low temperature electrolytes (Lee et al., 2005).

2.4.1.1 Scandia stabilized zirconia ($Sc_{0.1}ZrO_2$)

Scandia stabilized zirconia exhibits highest conductivity among the zirconia ceramic systems, as depicted in Table 2.4. This is due to Sc^{3+} has the closest size with Zr^{4+}, therefore the scandia doping in the zirconia lattice induces the smallest internal stress in the crystal structure and consequently the lowest activation energy for oxygen ion conduction (De Florio et al., 2004; Taroco et al., 2011). Zirconia ceramic with 7 and 13 mol% scandia addition exhibited high values of the ionic conductivity with a maximum at 10 mol% scandia (Haering et al., 2005).

Table 2.4: Values of ionic conductivity and activation energy of zirconia stabilized with different cation dopants (adapted from De Florio et al., 2004)

Dopant	Content (mol %)	σ_i at 1000°C (10^{-2} S.cm^{-1})	Activation energy (kJ.mol^{-1})
Y_2O_3	8	10.0	96
Sm_2O_3	10	5.8	92
Yb_2O_3	10	11.0	82
Sc_2O_3	10	25.0	62

Defect associates observed in high dopant concentration reduces the electrolyte conductivity due to mobility of oxygen ions is hindered. To prevent the detrimental effect of defect association, Haering et al. (2005) introduced the co-doping of titania in scandia stabilized zirconia ceramics and reported that 2 mol% TiO_2 was able to stabilize the cubic phase. However, the ionic conductivity of scandia stabilized zirconia decreases significantly with the addition of titania.

Figure 2.7 shows that at 600 °C, the ionic conductivity of 1 mol% ceria in 10 mol% scandia stabilized zirconia (1Ce10ScSZ) is highest (approximate 0.02 $S.cm^{-1}$) among all the other co-dopants investigated for scandia stabilized zirconia systems.

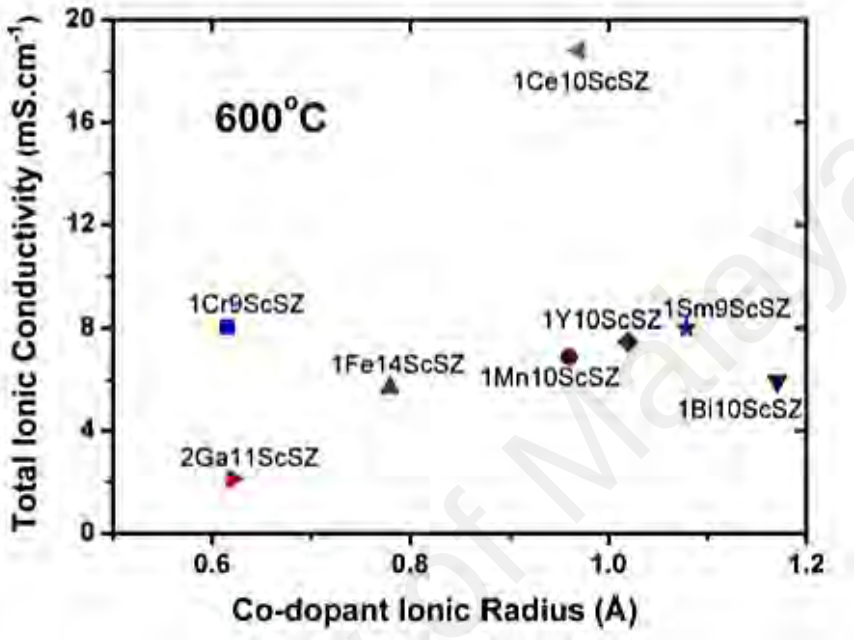

Figure 2.7: Selected total conductivity values reported in the literature at 600 °C plotted against the ionic radius of the co-dopant (Omar et al., 2012).

Figure 2.8 shows that the Young's modulus of the $Sc_{0.1}Ce_{0.01}ZrO_2$ (10Sc1CeSZ) ceramics sintered from the powders produced by two different manufactures namely Daiichi Kigenso Kagaku Kogyo (DKKK) and Praxair. Room temperature Young's modulus of the cubic DKKK 10Sc1CeSZ ceramics was reported to be 217.7±0.6 GPa, which is comparable with that of YSZ (around 220 GPa) reported by Morales et al. (2010). The lower Young's modulus observed in Praxair zirconia samples (188.2 ±2.8 GPa) were ascribed to the higher porosity of the ceramic.

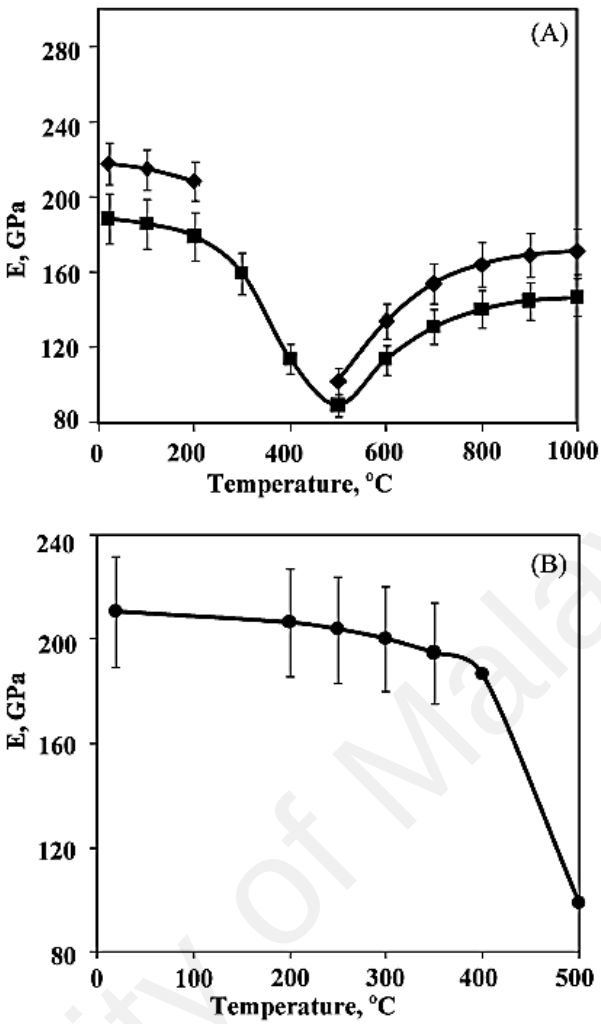

Figure 2.8: Young's modulus vs. temperature of the (A) cubic phase sintered from Praxair (–■–) and DKKK (–♦–) powders, and (B) the rhombohedral DKKK (–●–) $Sc_{0.1}Ce_{0.01}ZrO_2$ ceramics (Orlovskaya et al., 2010).

All the cubic 10Sc1CeSZ samples in Figure 2.8 (A) shows a significant softening and stiffening behavior when the temperatures were increased from 300-1000 °C, which was accompanied by a substantial fluctuation in Young's modulus. Rhombohedral phase was found to be stable up to 400 °C with minimum loss of stiffness and then showed a drastic reduction at 500 °C, as depicted in Figure 2.8 (B) (Orlovskaya et al., 2010). The changes of mechanical properties in zirconia-based ceramics at intermediate temperatures can be attributed to phase change (Kushi et al., 2009). It is apparent from Figure 2.8 that the rhombohedral phase of the zirconia ceramics demonstrated similar

stiffness with the cubic phase at 500 °C, signifying that a rhombohedral to cubic phase transition has occurred.

Figure 2.9 shows that the hardness of the DKKK and Praxair samples increased with increasing sintering temperatures. It indicates that a high sintering temperatures of 1500 °C is needed to achieve high density and to sustain mechanical integrity of the zirconia samples.

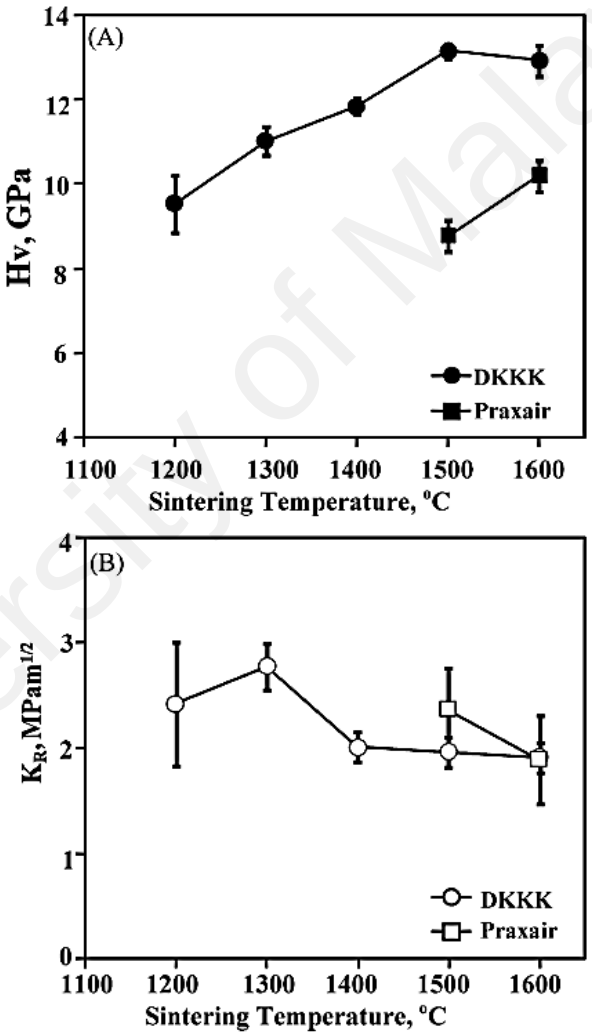

Figure 2.9: Hardness (A) and indentation fracture resistance (B) vs. sintering temperature for DKKK and Praxair $Sc_{0.1}Ce_{0.01}ZrO_2$ ceramics (Orlovskaya et al., 2010).

2.4.2 Ceria-based electrolytes

Like zirconia ceramics, ceria exhibits a fluorite-type structure with ionic conductivity of an order of magnitude greater than that of stabilized zirconia ceramics (except for scandia stabilized zirconia) due to larger ionic radius of Ce^{4+} than Zr^{4+}, which produces a more open structure through which oxygen vacancies can easily migrate, therefore can operate at low temperatures (Haile, 2003).

Ceria-based ionic conductor is normally doped with gadolina (CGO) or samaria (SDC) for the creation of requisite oxide ion vacancies to deliver high ionic conductivity (Kharton et al., 2001). Among them, Gd^{3+} has the lowest ionic radius mismatch with Ce^{4+}, therefore CGO exhibit superior ionic conductivity at low temperatures (Kazlauskas et al., 2012)

However, ceria based ceramics exhibit inferior chemical stability and has high electronic conductivity at low oxygen partial pressure, owing to the ceria cations are partly reduced from Ce^{4+} to Ce^{3+} under reducing atmosphere of the cell at elevated temperatures (Elyassi et al., 2009). This mixed conductivity leads to a diminution of the open circuit voltage available from the fuel cell due to partial internal short circuit, decreasing the fuel conversion efficiency (Figueiredo & Marques, 2013). The reduction of Ce^{4+} has been shown to be almost negligible at temperatures below 500°C in $Ce_{0.8}Gd_{0.2}O_{1.9}$, therefore stabilized ceria is a potential candidate for low temperature fuel cells (Doshi et al., 1999).

2.4.3 Lanthanum gallate-based electrolytes

Perovskites have the general structural formula ABO_3, in which A is a rare-earth, alkaline-earth, or alkali metal ion and B is a transition-group metal ion (Tejuca & Fierro, 2000). Their mixed conductivity, which results from oxygen vacancies, and their simultaneous electronic conductivity eliminate the need for external circuits and electrodes for oxygen separation system (Elyassi, 2009).

Nevertheless, for fuel cell applications, the electronic conductivity of the solid electrolyte should be minimized to improve efficiency. Perovskites, such as $SrCoO_3$, $SrFeO_3$, $LaCoO_3$, $LaFeO_3$, $LaGaO_3$, along with compounds that result from their single- or double-site substitutions, have been studied extensively for SOFC (Liu et al., 2006).

The perovskite, $LaGaO_3$, can be doped with strontium and magnesium, $La_{1-x}Sr_xGa_{1-y}Mg_yO_3$ (LSGM), to produce a material with good low-temperature oxygen-ion conductivity. LSGM has higher conductivity than stabilized zirconia electrolytes and does not have a reducible ion, like Ce^{4+}, and thus is superior to CGO for use in reducing conditions. However, LSGM is less stable with the anode, resulting in the formation of an insulating phase, $LaNiO_3$, at the anode– electrolyte interface (Joshi et al., 2004).

2.5 Effects of dopants

The ability to manipulate defect structure in crystal lattice through doping has triggered extensive research on engineering ceramics. The effects of doping through aliovalent impurity substitutions have been widely explored for oxide-ion solid electrolytes to generate high concentration of anion vacancies through ionic

compensation mechanism, in which additional charges involving vacancies or interstitials (ionic compensation) are created to preserve charge balance (West, 2007).

2.5.1 Aliovalent doping

Aliovalent doping involves the partial substitutions of lower or higher valence dopants in the host structure to generate high concentration of point defects, thereby altering the diffusion rates and the sintering behaviors of ceramics (De Jonghe & Rahaman, 2003).

Figure 2.10 show that pure MO_2-type ceramics has high concentration of electronic defects with strong dependence on oxygen partial pressures. The blue arrow in the inset diagram shows the ionic conductivity dominating electronic conductivity over a narrow oxygen partial pressure where intrinsic ionic defects are dominant ($[O_i^{''}] = [V_O^{\cdot\cdot}]$).

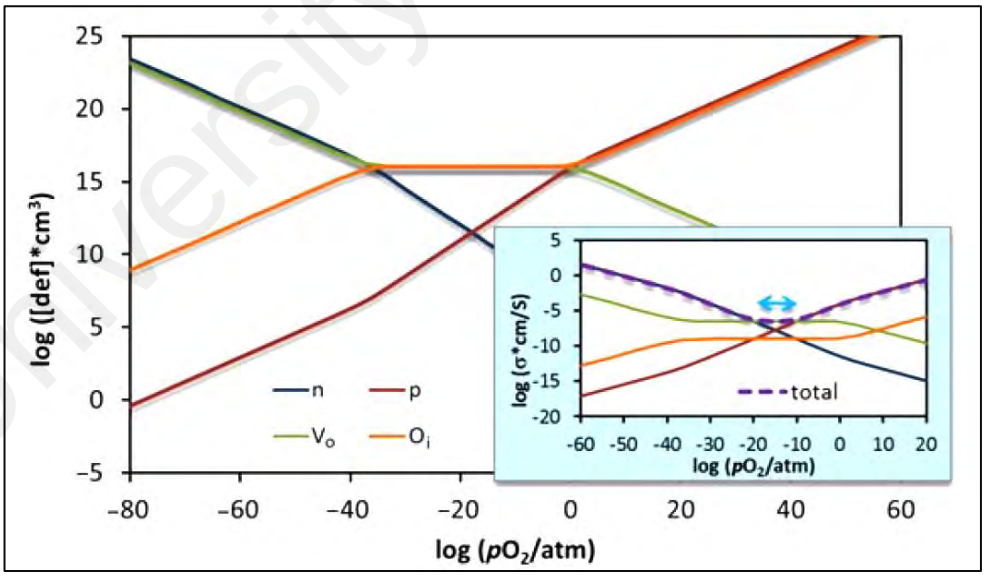

Figure 2.10: Schematic defect and related conductivity (inset) diagrams for one pure MO_2-type oxide with dominant anti-Frenkel defects (Figueiredo & Marques, 2013).

Figure 2.11 depict the impact of aliovalent doping with lower valance dopants to increase oxygen vacancies concentration and electrical conductivity over an extended

oxygen partial pressure range. The blue arrow in the inset of the diagram shows that the ionic conductivity dominating electronic conductivity over a large fraction of oxygen partial pressure where positive oxide vacancies are created to balance the negative dopant charge ($[F'_M] = 2[V_O^{\cdot\cdot}]$). This shows that the stability and ionic conductivity of oxide ceramics can be manipulated by point defects generated through aliovalent doping (Figueiredo & Marques, 2013).

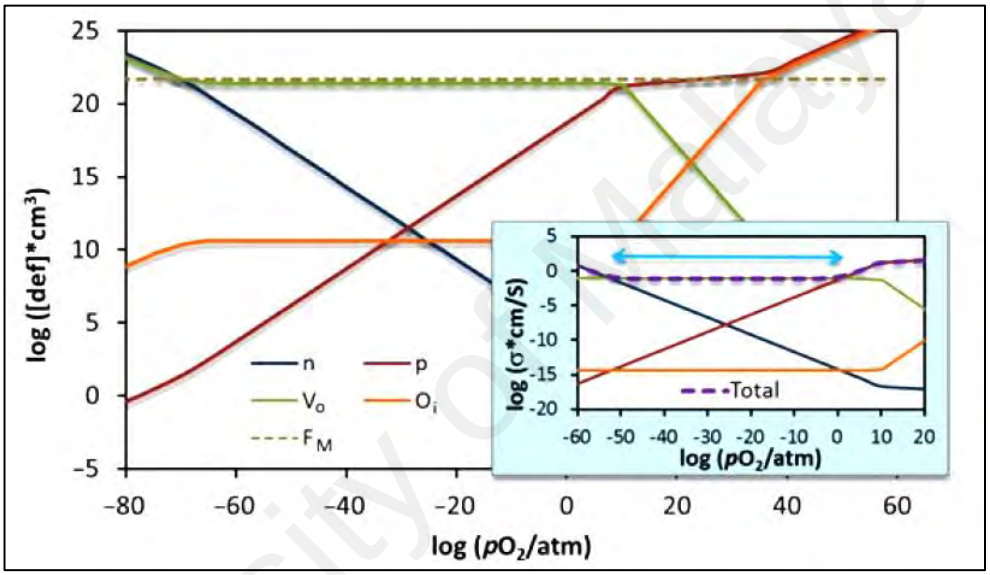

Figure 2.11: Schematic defect and related conductivity (inset) diagrams for one MO_2-type oxide with anti-Frenkel defects, doped with a trivalent cation (F_M) to generate oxide vacancies (V_O) (Figueiredo & Marques, 2013).

The oxygen vacancy transport properties of ionic ceramics within a large range of temperature and oxygen partial pressure follow the equation (Mori et al., 2008):

$$J = MC\nabla\mu, \tag{2.6}$$

where J is the flux of atoms along the grain boundary, M is the atomic mobility along the grain boundary, C is the vacancy concentration, and μ (the gradient in the chemical potential between the particle necks and a free surface) is the driving force for sintering.

Dopants can increase one or more of the above parameters to lower the sintering temperature. M can be affected by the dopants through liquid phase formation that increases the atomic mobility due to capillary effects. In addition, the dopant segregation to the grain boundaries causes the formation of a second phase. These factors can greatly contribute to the lowering of the sintering temperature of an electrolyte (Mori et al., 2008).

2.5.2 Co-doping

Recent works on co-doping showed promising results since the structural ordering seems to be avoided (Figueiredo & Marques, 2013). Various sintering additives on the cubic zirconia, mostly yttria-stabilised zirconia (YSZ) have been reported (Flegler et al., 2014).

Table 2.5 summarizes the recent research works that were carried out in relation to the use of various dopants as sintering aids or stabilizers in zirconia-based ceramic electrolytes, including binary/ ternary substitutions. The effect of the dopants or stabilizers on the mechanical integrity and cubic phase stabilizations of zirconia-based ceramics were investigated for potential use as electrolytes for intermediate temperatures SOFCs .

Yb_2O_3 (Lee et al., 2001), Dy_2O_3 (Maiti et al., 2009) and $InO_{1.5}$ (Piva et al., 2017) were employed as potential substitute for stabilizers in zirconia ceramics. Ytterbia stabilized zirconia and dyprosia stabilized zirconia were found to be an attractive material as electrolyte, with comparable ionic conductivity with YSZ. In contrast, destabilization of cubic phase caused by indium volatilization observed in indium oxide stabilized zirconia limits its applications for SOFC application.

Table 2.5: **Collations of the use of various dopants as sintering aids or stabilizers in zirconia-based electrolytes.**

Host	Dopants	Content	Sintering capability	Ionic conductivity	Reference
8YSZ	Al_2O_3	1 mol%	Good	Good*	Lee et al.(2000)
ZrO_2	Yb_2O_3	8 mol%	Good	Good	Lee et al. (2001)
8YSZ	Al_2O_3	0.7, 2, 4 wt%	Good	Fair*	Hassan et al. (2002)
3Y-TZP	Fe_2O_3	20 vol%	Good	Poor	Boukamp et al. (2003)
ScSZ	Bi_2O_3	1 mol%	Good	Good	Hirano et al. (2003)
8YSZ	Sc_2O_3	1- 5 mol%	Fair	Good	Kondoh et al.(2003)
10YSZ	Sc_2O_3	1- 5 mol%	Fair	Good	Kondoh et al.(2003)
8YSZ	B_2O_3	10-50 wt%	Good	Poor	De Florio&Muccillo(2004)
ZrO_2	$Y_x + Sc_{11-x}$	x=0-11 wt%	Fair	Good	Politova & Irvine (2004)
ZrO_2	Y+(N,Sc,Yb)	<4 mol%	Good	Good*	Lee et al. (2006)
10ScSZ	MnO_2	1 mol%	Good	Good	Peck et al. (2007)
11ScSZ	Mn_2O_3	2 mol%	Good	Good	Lei & Zhu (2007)
10Sc1CeSZ	Li_2CO_3	3 mol%	Good	Good	Mori et al.(2008)
8YSZ	Al_2O_3	20 wt%	Fair	Good	Kumar et al. (2008)
ZrO_2	Dy_2O_3	8-10 mol%	Good	Good	Maiti et al. (2009)
8YSZ	TZP	10-30 vol%	Good	Poor	Li & Ren (2011)
3YSZ	Fe_2O_3	3 mol%	Good	Poor	Kravchyk et al.(2012)
10ScSZ	Sc,In,Yb,Y, Gd,Sm	1 mol%	Good	Good	Omar et al. (2012)
ScSZ	Al_2O_3	0.25- 5 wt%	Good	Good*	Guo et al. (2013)
7ScSZ	Fe_2O_3	3 mol%	Good	Good	Bohnke et al. (2014)
10ScSZ	CeO_2	0.5-5 mol%	Poor	Good	Dasari et al. (2014)
12.5CaSZ	Mn_3O_4	0.1-0.5 mol%	Good	Good	Huang et al. (2014)
YSZ	TiO_2	5- 30 mol%	Good	Poor	Colomer et al.(2016)
YSZ	CeO_2	5-15 wt%	Poor	Good	Maurya et al. (2016)
10ScSZ	Dy_2O_3	1 mol%	Good	Good	Grosso et al.(2016)
xSc1CeSZ	Sc_2O_3	x= 5-11 mol%	Poor	Good	Kumar et al.(2016)
ZrO_2	$InO_{1.5}$	17.4 & 22.2 mol%	Good	Poor	Piva et al.(2017)
6ScSZ	CeO_2	1-2 mol%	Poor	Good	Kubrin et al.(2017)
4ScSZ	CeO_2	1-2 mol%	Poor	Good	Kubrin et al.(2017)

* larger dopant content leads to lower bulk conductivity caused by the formation of insulating second phase or increased dopant-defect association.

Several publications have addressed the indispensable efforts to improve mechanical integrity on yttria-stabilized zirconia ceramics. Hassan et al. (2002) added 0.7 mol% alumina to YSZ and recorded enhanced densification in the zirconia ceramic at low sintering temperature of 1400 °C. Similar trend was reported by Boukamp et al. (2003) with the addition of 20 vol% Fe_2O_3 in 3Y-TZP, which reached 96 % relative density when sintered 1150 °C for 2 hours. De Florio & Muccillo (2004) found that B_2O_3 that melts at 460 °C could effectively aided in reducing porosity in 8YSZ. The addition of TZP was also reported to lower the sintering temperature of YSZ (Li & Ren, 2011). The densification, strength, and fracture toughness increased with increasing TZP contents, with a maximum at 20 vol%, existed as the second phase in the YSZ for strengthening and toughening effect of the solid solution. However, the addition of >20 vol% of YTZP recorded lower mechanical properties, attributed to grain growth. Another study by Kravchyk et al. (2012) reported 3 mol% Fe_2O_3 in YSZ reduced sintering temperature to 1450 °C to achieve 98 % density, compared to 1600 °C for 87 % density in pure YSZ, and limits the grain growth. High amount of TiO_2 (5- 30 mol%) was added to YSZ to achieve a near to full relative density (99.9 %) at low sintering temperature of 1500 °C, as compared to 93 % in undoped YSZ (Colomer et al., 2016).

In contrast to enhanced sintering behavior, the doping of the yttria-stabilized zirconia ceramics in these published works demonstrated destabilization of cubic phase. High monoclinic or tetragonal content caused loss of ionic conductivity, which led to electronic conductivity.

Small addition of alumina dopant (< 2 mol%) has been reported to improve stability and ionic conductivity in zirconia ceramics (Lee et al., 2000; Hassan et al., 2002; Guo et al., 2013), which could be attributed to its scavenging effect on siliceous phase at grain boundaries. But larger alumina contents would lead to higher bulk resistivity. However,

a contradicting result presented by Kumar et al. (2008) showed that 20 wt% alumina in 8YSZ exhibited an increased bulk conductivity, which was correlated as space charge effect with reduced charge carriers that leads to enhancement in their mobility.

Several dopants have been added to obtain dense scandia stabilized zirconia ceramics with suitable properties at lower sintering temperatures, which include Bi_2O_3 (Hirano et al., 2003), MnO_2 (Peck et al., 2007), Mn_2O_3 (Lei & Zhu, 2007), Li_2CO_3 (Mori et al., 2008), Gd_2O_3 and Sm_2O_3 (Omar et al., 2012), Fe_2O_3 (Bohnke et al., 2014), Dy_2O_3 (Grosso et al., 2016). These dopants have been found to effectively stabilize cubic phase of ScSZ and hence showed improved ionic conductivity. 12 mol% calcia-stabilized zirconia (12.5 CaSZ) also reported to demonstrate enhanced densification to 96.8% relative density when doped with up to 0.5 mol% Mn_3O_4, and obtained stabilization of the cubic phase when the Mn_3O_4 was added to 0.3 mol% (Huang et al., 2014).

The influence of ceria additions on the mechanical properties YSZ and ScSZ have been studied by Dasari et al. (2014), Maurya et al. (2016), Kumar et al. (2016) and Kubrin et al. (2017). High CeO_2-additions were found to cause expansion of the zirconia host lattice and considerably impaired their densification and mechanical properties. On the other hand, low ceria doping (0.5- 1 mol%) exhibited enhanced conductivity with imposed higher cubic symmetry in all the host crystal lattice of zirconia ceramics, reducing the tendency to form the tetragonal phase. This is attributed to larger ionic size of Ce^{4+} compared to that of host cations (Zr^{4+}) and stabilizers (Sc^{3+}), thus increases the tendency to form the eight-fold coordination with oxygen rendering stability to cubic fluorite structure.

A similar co-doping approach for improving the ionic conductivity of fluorite-structured electrolytes using Y_2O_3- Sc_2O_3 was employed by Kondoh et al. (2003) and Politova and Irvine (2004). The two different cations played a different role in the

material system. Sc^{3+} addition aims to improve the ionic conductivity due to its similar ionic radius with Zr^{4+}, thus minimizing cation-defect associations; while Y^{3+}, on the other hand, was introduced because its larger ionic radius fully stabilizes the fluorite structure and avoided phase transition to a lower-symmetry phase observed in pure ScSZ. However, co-doping of Y-N, Y-Sc, and Y-Yb in ZrO_2 undergo a pronounced conductivity deterioration at low temperatures (<500°C) due to strong vacancy-vacancy interactions (Lee et al., 2006).

2.6 Fabrication of SOFC

The fabrication routes of SOFC are generally divided into two categories: wet ceramic routes and gas-phase routes. The four wet ceramic manufacturing routes (screen printing, slurry painting, tape casting, and calendaring) involve a high temperature sintering process, while the two most common gas-phase manufacturing routes, Electrochemical Vapour Deposition (EVD) and Physical Vapour Deposition (PVD) do not require a sintering step, as illustrated in Figure 2.12.

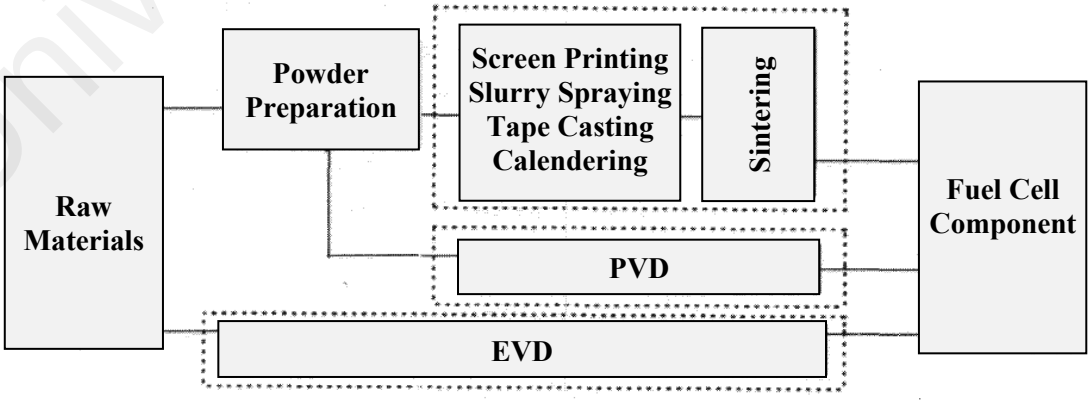

Figure 2.12: SOFC fabrication processes (Hart et al., 2000)

Wet ceramic routes use simpler and less energy intensive equipment as compared to EVD and PVD, because the gas phase techniques requires large high vacuum chambers and power sources. The energy requirement to produce YSZ electrolyte for all the manufacturing processes mentioned was less than 20 $kWhm^{-2}$, except for EVD, which has the highest energy consumption of 100 $kWhm^{-2}$ (Hart et al., 2000). Table 2.6 shows a comparison of various fabrication techniques in terms of equipment, set-up cost, and energy requirement.

Wet ceramic routes are favored due to cost aspects and simple equipment set-up, even though high temperature sintering might be required.

Table 2.6: Comparison of various fabrication techniques in terms of equipment, set-up cost, and energy requirement.

	Equipment	Set-up cost	Energy requirement
Wet ceramic routes	Simple	Inexpensive	Low
PVD	Complex	Expensive	Low
EVD	Complex	Expensive	High

2.6.1 Rapid sintering

The use of conventional methods to consolidate ceramic powder compacts often leads to grain growth due to the extended sintering time. There are challenging demands for new and improved processing techniques to produce finer microstructures and enhanced physical and mechanical properties. Unconventional electromagnetic-field assisted powder consolidating techniques have good potential to induce fast densification and controlling grain growth to produce high-quality homogeneous and crack free ceramics (Olevsky et al., 2007; Menezes & Kiminami, 2008). Electromagnetic-field assisted sintering includes spark plasma sintering, two electrode-method sintering, and microwave sintering (Raj et al., 2011).

Figure 2.13 summarises the recent progress of various rapid sintering techniques applied on zirconia ceramics for which sintering techniques are later discussed in this chapter.

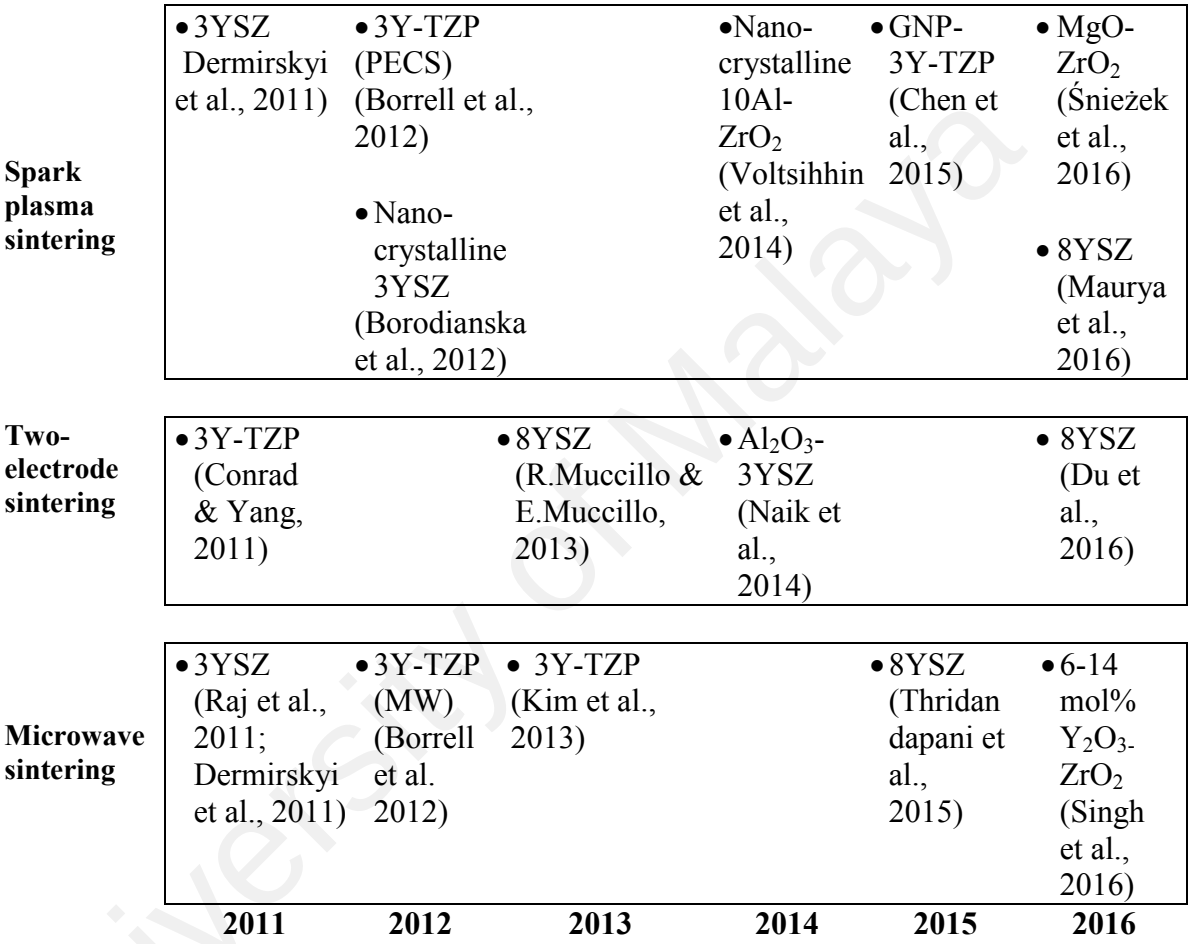

Figure 2.13: Recent progress of various rapid sintering techniques applied on zirconia ceramics studied via spark plasma sintering, two-electrode sintering, and microwave sintering.

2.6.2 Spark Plasma Sintering (SPS)

Spark plasma sintering (SPS) or pulsed electric current sintering (PECS) is one of the processes that involves the use of electric discharge or current to aid in the sintering of ceramic powder (Munir et al., 2006). This current activated sintering process enable

high heating rate by applying simultaneously a uniaxial pressure and a pulsed (and/or dc) electric current that induce electrical discharges at the powder particles surfaces within a conducting die (usually graphite), which caused simultaneous resistance heating (Borodianska et al., 2012). SPS has been used to realize high heating rates and obtain high final density couple with high mechanical properties for the sintered bodies.

SPS was used to sinter nanocrystalline 3YSZ ceramic at 800-1100 °C with a small applied pressure of 40 MPa, with a heating rate of 80 °C/min and 30 minutes dwell time (Borodianska et al., 2012). Voltsihhin et al. (2014) fabricated 10 vol% Al_2O_3 nano-fibres reinforced ZrO_2 by SPS with near full density (93% of theoretical density) at sintering temperature of 1100 °C with a heating rate of 100 °C/min and 5 minutes dwell time, while the sample produced by conventional sintering technique at 1300 °C for 1 hour had a densification degree of 74% only. A 90.6% increase in hardness and a 40.6% increase in elastic modulus were observed in these Al_2O_3- ZrO_2 composites (Voltsihhin et al., 2014).

Chen et al. (2015) produced 0.01-0.05 wt% graphene platelets (GNPs) reinforced 3Y-TZP composites by SPS. The 0.01 wt% GNP/ 3Y-TZP composites exhibited the highest relative density of 99.4% and reached the maximum fracture toughness of 15.3 $MPa.m^{1/2}$. Śnieżek et al. (2016) investigated MgO–ZrO_2 ceramic composites by applying SPS at 1600 °C with a pressure of 100 MPa reported stabilization of ZrO_2 by MgO due to liquid phase sintering.

In another work by Demirskyi et al. (2011), two rapid heating techniques, SPS and 2.45 GHz microwave heating were used to sinter 3 mol% yttria stabilized zirconia to 800- 1200 °C under a pressure of 40 MPa, at a heating rate of 80 °C/min. The maximum dwell time was 20 minutes. Both sintering methods demonstrated similar material push-

out from direct field-induced effect at 800- 850 °C. Liquid phase were reported to be forced out from the particle's core to form a small sphere outside the initial large spheres (Demirskyi et al., 2011).

On the other hand, Maurya et al. (2016) has analyzed the mechanical properties of 8YSZ ceramic prepared by SPS at 1250 °C with a holding time of 5 minutes, under compaction pressure of 30 MPa. The 8YSZ pellets possessed lower elastic modulus and hardness (~28% and 44% reduction, respectively) when compared to that of conventional sintering, which was attributed to the lower extent of sintering, demonstrated by the bigger pore size observed along the grain boundary. The discrepancy in the mechanical properties of conventional sintered and spark plasma sintered 8YSZ ceramics was attributed to the inter-particle friction in SPS that may have restricted complete densification during sintering in the ceramic.

Borrell et al. (2012) compared the effect of three different types of sintering techniques on the densification of 3Y-TZP. The author revealed that 3Y-TZP sintered by PECS has higher density compared to conventional sintering, and was comparable to the microwave sintered samples. However, the surface of the 3Y-TZP samples were found to turn into black color after PECS sintering at 1300-1400 °C, which was a sign of carbon diffusion from carbon rich atmosphere and graphite die. Heat treatment involving high temperatures (> 800 °C) with long holding time (> 2 hours) was needed to eliminate the carbon contamination (Borrell et al., 2012).

2.6.3 Two-electrode sintering

In a flash sintering, densification of ceramics is expected to occur in just a few seconds. It has been reported that flashing sintering involved the application of an

electric field to a pre-heated ceramic compact through rapid resistive (Joule) heating at grain boundaries (Cologna et al., 2010, Ji et al., 2017). This can be achieved by employing a two-electrode sintering in which a small dc or ac electric field is applied with two electrodes connected to both ends of the sample. Increased sintering rate and corresponding refined grain size can be attained when the electric current flows through the sample, while it is heated in an furnace which controls the sample temperature independently (Conrad & Yang, 2011; Raj et al., 2011). Local Joule heating raises the sample temperature and the ionic conductivity of the ceramics follows the typical Arrhenius behavior (Du et al., 2016). Flash sintering takes place from the abrupt increase in the electrical conductivity of the ceramic materials in the presence of strong electric fields at low furnace temperatures of ~1000 °C (Naik et al., 2014, Du et al., 2016).

Conrad & Yang (2011) sintered 3Y-TZP by applying constant dc field strengths of 1.7- 50 Vcm^{-1} for both binder bake-out and subsequent sintering stage. Significant enhancement in the sintering rate with increasing applied field strength up to 20 Vcm^{-1} was attributed to suppressed grain growth through the interaction of the electric field with the space charge at the grain boundaries (Conrad & Yang, 2011). 8YSZ ceramic flash sintered by applying ac voltages up to 70 Vcm^{-1} in the 800-1000 °C range for 5 seconds showed inhibited grain growth with intergranular pores (R. Muccillo & E. Muccillo, 2013).

On the other hand, Naik et al. (2014) carried out two-electrode flash sintering on undoped alumina and 50 vol% alumina- 3YSZ composites. Both materials were first heated at 600 °C for 1 hour to remove the binder. This was followed by flash sintering in a furnace that was ramped with heating rate of 10 °C min^{-1} to 1060 °C under an electrical field of 150 Vcm^{-1}. Undoped alumina was found to be immune to flash

sintering at electric field up to 1000 Vcm^{-1}. Alumina-doped 3YSZ ceramic on the hand recorded larger grain sizes, which is in contrast to the retarding effect of the field on grain growth during two electrode sintering observed in other works (Naik et al., 2014). 8YSZ was flash sintered by Du et al. (2016) using 50 Vcm^{-1} electric field and reported no significant differences between the densification and electrical properties of conventionally and flash sintered samples, except for larger average grain size observed in the flash sintered samples.

2.6.4 Microwave sintering

Microwave sintering is another promising electromagnetic-field assisted method of sintering. Microwave energy is a form of electromagnetic energy, with the wavelength ranging from 1 m to 1 mm, which corresponds to a frequency range of 300 MHz to 300 GHz. It is an effective self-heating technique in which a dielectric material couple with microwave field and the heating is accomplished by absorbing electromagnetic energy volumetrically. It allows densification with short holding time owing to rapid heating rates (Agrawal, 2006; Oghbaei & Mirzaee, 2010). A comparison between conventional and microwave heating patterns is illustrated in Figure 2.14, showing the reversed temperature gradient in microwave heated sample.

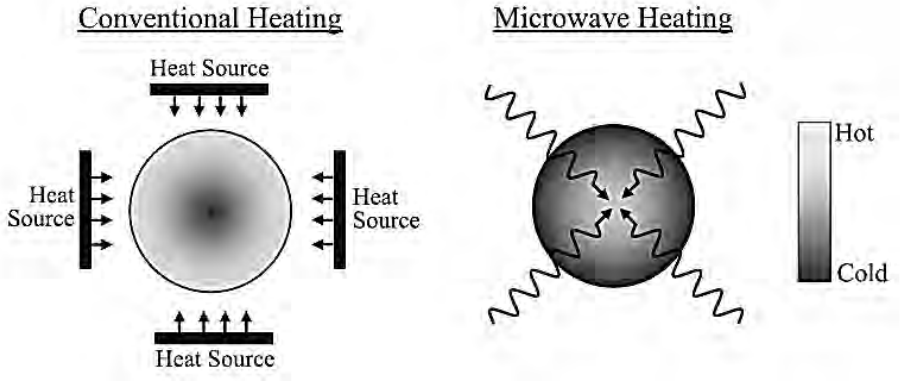

Figure 2.14: Conventional and microwave induced heating patterns (Bhattacharya & Basak, 2016).

The most commonly used frequencies for domestic and commercial heating purposes are 915 MHz and 2.45 GHz, which are in one of the industrial, scientific and medical (ISM) radio bands reserved for non-communication purposes (Das et al., 2009; Chandrasekaran et al., 2012). The two frequencies also correspond to significant penetration depth following Equation (2.7). The penetration depth into the conductors at a given frequency of the microwave radiation depends on the conductivity and permeability of the material (Bhattacharya & Basak, 2016).

$$d = \sqrt{\frac{1}{\pi f \sigma \mu}} \tag{2.7}$$

Where d= penetration depth, f= frequency of the radiation, σ= conductivity of the material, μ= permeability of the material.

Therefore, microwave process operating at 2.45 GHz would produce samples with the interior hotter than surface because of heat loss from the surface, while for higher frequencies such as 30 GHz and 83 GHz show an inverse temperature profile due to reduced skin depth that caused skin or crust sintering as the microwave penetration depth decreases with increasing its frequency (Birnboim et al., 1998).

A two way hybrid microwave heating with susceptors is shown in Figure 2.15. Heat generation due to microwave-susceptor and the microwave-material interactions are used to overcome the reversed thermal gradient in microwave heating (Bhattacharya & Basak, 2016).

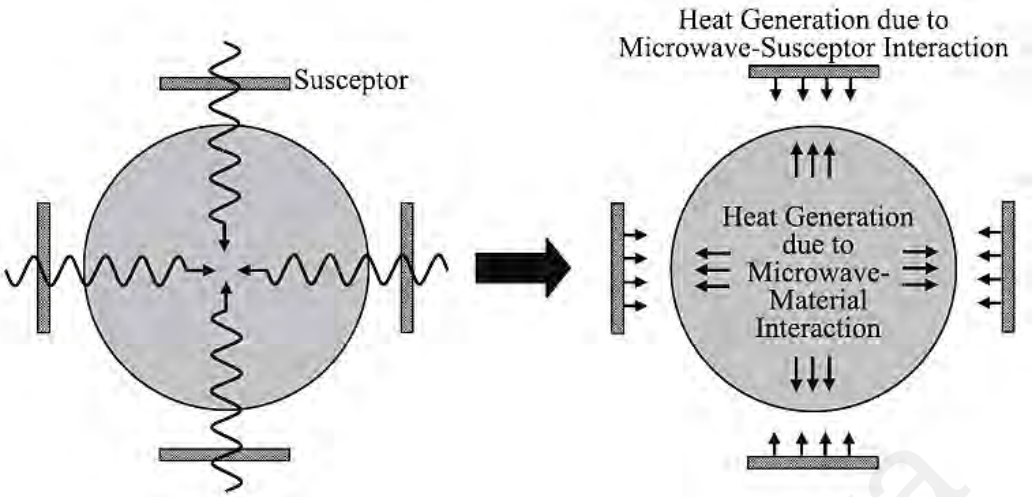

Figure 2.15: Two-way hybrid microwave heating with susceptors (Bhattacharya & Basak, 2016).

Comparison of the microwave hybrid sintering processes of Y-TZP with conventional sintering process with respect to the sintering time, production cycle, and energy consumption are presented in Figure 2.16. The rapid sintering process during microwave hybrid sintering (with SiC tubular susceptor) was able to raise the production rate with reduced sintering time and production cycle, and at the same time lower the energy consumption due to shorter heating time (Zhao et al., 2000).

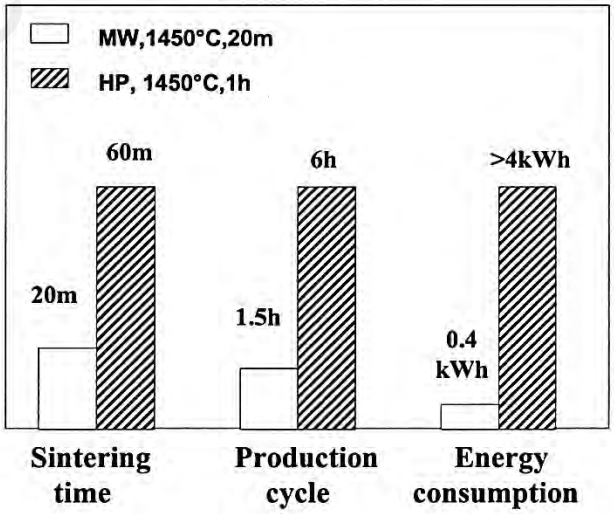

Figure 2.16: Comparison between microwave hybrid sintering (MW) and conventional sintering (HP) of Y-TZP (Zhao et al., 2000)

Table 2.7 shows the effect of microwave assisted sintering on phase composition, microstructure and densification of various inorganic materials. Microwave assisted sintering were found to produce samples that are superior to conventional resistance furnace sintering, especially on ceramic materials.

Table 2.7: Few examples of effect of microwave assisted sintering on phase composition, microstructure, chemistry, and densification of various inorganic materials ([1]Kesapragada et al., 2003; [2]Breval et al., 2005; [3]Souto et al., 2007; [4]Wang et al., 2007; [5]Lefeuvre et al., 2010; [6]Padmavathi et al., 2011; [7]Dey et al., 2013)

Material	Micowave heating		Phase/ Microstructure/ Chemistry	Densification	Ref.
	Temp/Dwell time (°C)	Susceptor			
LSGM	1.5–2.25 kW/ 20 -30 mins	SiC	~95% theoretical density with a fine grained microstructure and without the presence of other phases.	Good	(1)
WC/Co	1300-1450°C/ 10 mins	No	W not dissolved in Co/ Smaller WC grains and finer Co binders/ More uniform distribution of Co binder.	Good	(2)
SiO_2-Al_2O_3	1.25 kW/ 20 mins	SiC	Homogeneous, finer grain size/ Elongated grains.	Good	(3)
ZnO	1296°C/ 15 mins	No	Pure ZnO/ Homogeneous ZnO rod structures	-	(4)
Al_2O_3	1300/1600 °C/ 30 mins	Lossy ceramics	Homogeneous/ Nanopowders fill the space between grains of bigger size.	Good	(5)
Al-Mg-Si-Cu alloy	590°C/ 1 hour	No	No intermetallic Mg_2Si/ Inhomogeneous/ Larger melt fraction at grain boundary	Fair	(6)
Na-Zr-P/ Ca-Zr-P	1100-1250°C/ 1 hour	No	Crystallinity increase/ Inhomogeneous / Na rich liquid phase at grain boundary	Good	(7)

This is evidenced in the microwave sintering of Lanthanum gallate doped with alkaline rare earths (LSGM) powders by applying 1.5 to 2.25 kW for 20 to 30 minutes with SiC as susceptors. High theoretical density of 95% and fine grained microstructure (~2- 3μm) without any undesirable phase was reported when the LSGM was microwave sintered using 1.75 kW of microwave power for 20 minutes (Kesapragada et al., 2003).

Microwave sintering process of 6-12 wt% cobalt- tungsten carbide (WC/Co) ceramic composite carried out by Breval et al. (2005) at the sintering temperature ranges from 1300- 1450 °C for 10 minutes produced more uniform distribution of cobalt binder in the WC/Co composite, with higher hardness and better corrosion resistance recorded in microwave sintered samples as compared to conventional sintered samples. A large amount of tungsten was found to dissolve into cobalt binder in conventional heating.

Microwave sintering of ceramic was also reported to be favorable in a work reported by Wang et al. (2007), in which ZnO was microwave sintered at 1296 °C for 15 minutes with an extremely fast heating rate of 500 °C /min. The rapid heating process produced pure ZnO with homogeneous rod structures coupled with good electrical properties. However, there was no densification result presented for the sintering of ZnO.

In another microwave sintering of ceramic work reported by Lefeuvre et al. (2010), two step microwave heating was applied to alumina of different granulometries, a 10 vol% nano-sized Al_2O_3 powder in micro-sized Al_2O_3 matrix. The samples were heated to 1300 °C for 30 minutes, in the first sintering step, which was then followed by heating to 1600 °C and hold for another 30 minutes. The heating rate for both sintering steps was 100 °C/ min. A homemade lossy ceramic was used as the susceptor to provide infrared heating to the surface of the compact particles. The microwave sintered samples attained near full densification (98 %) with uniform microstructure, which was

attributed to the redistribution of nanoparticles to fill the voids between grains of bigger size (Lefeuvre et al., 2010).

Souto et al. (2007) sintered aluminosilicate, SiO_2-Al_2O_3 using microwave furnace. The samples attained 97 % of theoretical density and displayed homogeneous microstructure by applying 1.25 kW of power for 20 minutes, which can only be obtained at a firing temperature of 1650 °C and a dwell time of 2 hours in conventional sintering (Souto et al., 2007).

Al-1Mg-0.85Si-0.25Cu alloy was microwave sintered at 590 °C for 1 hour at a heating rate of 22 °C /min, as compared to 5 °C /min in conventional furnace, resulted in 58% reduction in processing time. Supersolidus liquid phase sintering (SLPS) occurred in both sintering modes. Inhomogeneous microstructure produced owing to larger melt fraction observed at grain boundary from microwave processing. No intermetallic Mg_2Si was found in microwave sintered samples due to insufficient time for intermetallic phase precipitation (Padmavathi et al., 2011).

Sodium zirconium phosphate and calcium zirconium phosphate ceramics were microwave sintered at 1100-1250 °C for 1 hour, and obtained higher density compared to samples conventional sintered at 1350 °C for 2 hours. Formation of pores at grain boundaries was suggested to be caused by sodium-rich liquid phase penetrating the grain boundaries (Dey et al., 2013).

2.6.4.1 Microwave sintering of zirconia ceramics

3Y-TZP was sintered by microwave heating at 1300-1400 °C with a heating rate of 30 °C/min and a holding time of 10 minutes (Borrell et al., 2012). The microwave

method produced fully dense (99.9 %) samples at 1400 °C with more homogeneous microstructures compared to the sample conventionally sintered at the same temperature. Another work reported by Kim et al. (2013) on 3Y-TZP also demonstrated similar result, in which close to full density were obtained from the microwave sintered samples at 1450-1500 °C for 20 minutes, with a heating rate of 50 °C/min.

A similar observation was made by Singh et al. (2016) during sintering of 6- 14 mol% Y_2O_3-ZrO_2 by microwave processing and conventional processing at 1400 °C for 20 minutes and 4 hours, respectively. Both samples achieved the same degree of densification and bulk conductivity, indicating microwave is the better alternative in processing of YSZ in terms of energy and time saving without compromising the product quality.

Thridandapani et al. (2015)'s work on microwave sintering of 8YSZ showed full densification at 1300 °C. The enhancement in diffusion along grain boundaries was attributed to preferential heating of the grain boundaries by electric field. Raj et al. (2011) postulated that local Joule heating from microwave radiation raises the temperature at the grain boundaries of 3YSZ, resulting from high values of dielectric loss and the electrical resistance of grain boundaries. Dermirskyi et al. (2011) suggested that the reversed thermal gradient caused local melting and material push-out from hot inside to cold outside of the 3YSZ spherical particles.

2.7 Summary

The ceramic electrolyte is the key component that determines the efficiency of the solid oxide fuel cell. In summary, the development of ceramic electrolyte material of SOFC aims to satisfy five basic requirements: (1) high density, (2) compatibility of

thermal expansion, (3) chemical stability, (4) high ionic conductivity, (5) mechanical and structural stability. In order to widen their applications in the new technologies associated with energy generation, the enhancement in mechanical and structural stability, as well as electrical conductivity is urgently demanded.

Reducing the operating temperature to below 800 °C could prevent undesirable phase formation of its components and save more energy; therefore it has become the new aim in SOFC development. The operating temperature of SOFC is largely governed by the electrolyte material, but the electrical conductivity of solid oxide electrolytes have been found to decrease significantly when the operating temperature is reduced. Therefore, developing high ionic conductivity electrolyte materials with good mechanical and chemical stability is the main technological limitation in commercialising the Intermediate Temperature-SOFCs (IT-SOFCs).

The disadvantage of easy reduction and high reactivity in ceria-based ceramics and difficulty to minimize electronic conductivity in perovskite structure justified a moderate interest in these types of ceramics for IT-SOFC. Scandia stabilized zirconia is the preferred ceramic oxide candidates because of its advantages in terms of CTE match with other SOFC components, highest ionic conductivity among zirconia ceramics, and exceptional chemical stability at reducing environment at intermediate temperatures. Improving processing techniques and addition of dopants could be reliable tool to optimise the mechanical and electrical properties of electrolytes.

Previous studies indicate that the improvement on solid oxide electrolyte materials is linked to possibilities of doping to modify the microstructure and the properties of the ceramic oxide. In order to further improve the electrolytes, co-doping has been used intensively in recent years and was found to effectively enhance the mechanical integrity and ionic conductivity of fluorite-structured electrolytes. Various metal oxides

have been added as sintering aids to facilitate the sintering and increase the stability of the ceramic materials, as well as possibility to hinder grain growth during sintering. Continual effort is therefore still worth in developing co-dopants for use in low temperature co-firing of zirconia-based components for IT-SOFC fabrication. Material design based on the studies of doped systems may offer a way forward in the development of IT-SOFC.

Other than selection of proper material system, producing solid electrolyte with appropriate mechanical and electrical properties has been a main challenge for SOFC fabrication. The optimization of the processing and fabrication procedure is crucially important and it is a challenging area of research.

One problem concerning conventional sintering of solid electrolyte, notably zirconia ceramics, typically requires thermal cycles of several hours to attain full density and stabilized crystal structure, but on the other hands would lead to rapid grain growth and hence poor mechanical stability. In order to obtain fine grains and high stability in zirconia ceramics, a rapid heating technique should be employed for sintering. Field assisted sintering technique is one of the fast sintering technique that is effective in satisfying both criterion for the processing of zirconia ceramic for intermediate temperature SOFC electrolyte applications.

Spark plasma sintering can achieve extremely high heating rates by direct heating from the Joule effect. However, this process is constrained by difficulty in controlling the extent of sintering and diffusion of carbon from the carbon rich atmosphere and graphite die.

Two-electrode sintering is able to quickly densify conductive ceramic particle compacts in seconds in response to an applied electric fields, despite difficulty in

controlling porosity and grain size due to larger thermal gradients in material and the prolong time needed for ramping to the flash sintering temperature regime in a conventional furnace.

Microwave sintering exploits fast heating rates from volumetric heating to allow the rapid consolidation of various materials and promotes fine microstructure. For microwave transparent materials such as zirconia ceramics, which has low dielectric loss properties at low temperatures, susceptors may be used to raise the specimen temperature to a regime where it is receptive to microwave heating. The microwave heating is able to accelerate densification and thus reduce the production time.

Clearly, the development of proper electrolyte materials for SOFC still remains a challenge. Future research will encompass additional studies on material selection, further work on different processing, especially of lower temperature fabrication routes, and the relationship of these techniques to electrolyte performance must be discussed in detail.

CHAPTER 3: EXPERIMENTAL TECHNIQUES

3.1 Introduction

This chapter provides the details on the experimental studies conducted on scandia stabilized zirconia ceramics, which include the process of incorporating dopant into zirconia ceramics and producing zirconia compacts via conventional and microwave heating techniques. Powder synthesis, sintering set-ups and measurement techniques, as well as associated test parameters will be reported.

Major measurements or studies conducted on the scandia stabilized zirconia ceramics are mechanical tests, electrochemical characterization, microstructural investigation and chemical analysis.

3.2 Powder preparation

3.2.1 Synthesizing ceria-doped scandia stabilized zirconia powder

This research started with employing solid state reaction technique to synthesize 1 mol % ceria-doped 10 mol % scandia stabilized zirconia (10Sc1CeSZ). The synthesized powders would be used to prepare pellets for sintering and then compare the mechanical and electrical properties with the compacts prepared from a commercially available 10Sc1CeSZ powder.

3.2.1.1 Mixing of reactants

10Sc1CeSZ powder was synthesized by mixing and mechanical milling of the following high purity oxide powders: 89 mol% zirconium oxide (Sigma Aldrich, 99% purity, 5μm), 10 mol % scandium oxide (Stanford Materials, 99.99% purity, 2-5 μm), 1 mol % cerium oxide (Sigma Aldrich, 99.9% purity, < 25 nm). A 100 g powder were

weighted in the appropriate amount as tabulated in Table 3.1 and then poured into a beaker for mixing in an ultrasonicator.

Table 3.1: Weight of reactant mixtures for a 100 g batch of 10Sc1CeSZ powder

Material	Weight (g)
Zirconium oxide, ZrO_2	87.61
Scandium oxide, Sc_2O_3	11.02
Cerium oxide, CeO_2	1.37

The 10Sc1CeSZ powder was thoroughly mixed ultrasonically in ethanol for 30 minutes to form a uniform dispersion. The mixture of the reactants was then placed inside a high density polyethylene (HDPE) bottle together with 5 mm diameter partially-stabilized zirconia (PSZ) balls. The bottle was then rotated for 1 hour on a table-top ball milling machine at 600 rpm. The effect of tumbling motion with milling balls is to reduce the average particle size of the reactants in addition to achieve an intimate mixture (West, 2007).

3.2.2 Doping of 10Sc1CeSZ with MnO_2

After comparing the difference between synthesized and commercial 10Sc1CeSZ powders in terms of phase stability and sintering properties, commercial powder demonstrated better properties. Further studies will be all based on commercial powder.

The commercially available 10Sc1CeSZ powder was supplied by Daiichi Kigenso Kagaku Kogyo (DKKK), Japan. According to the powder specifications provided by DKKK, the powder had a total impurity concentration of less than 0.1 wt%, comprised of small amount of various impurities (SiO_2, Fe_3O_4, TiO_2, Na_2O and CaO), as

shown in Table 3.2. The 10Sc1CeSZ powder had a specific surface area of 11.1 m^2/g and an average particle size of 0.53 μm.

Table 3.2: Specifications of commercially available 10Sc1CeSZ powder supplied by Daiichi Kigenso Kagaku Kogyo.

	Analytical value (weight %)									
ZrO_2+HfO_2	Sc_2O_3	CeO_2	Al_2O_3	SiO_2	Fe_2O_3	TiO_2	Na_2O	CaO	H_2O	Ig. loss
87.6± 0.5	11± 0.5	1.4± 0.2	-	0.02	0.01	0.01	0.01	0.01	-	-

3.2.2.1 Mixing of reactants

Varying amounts of high purity manganese (IV) oxide (0.5, 1 and 5 wt. %) (R&M Chemicals, UK) were doped into 10Sc1CeSZ powder via attrition milling in ethanol. Ethanol was used as the mixing medium to prevent coalescence of the powder particles during milling.

Mixtures of MnO_2 and 10Sc1CeSZ were diluted with ethanol and ultrasonically mixed for 30 minutes. Subsequently, the mixtures were subjected to attritor milling to break the agglomerates. The milling process was carried out in a 750 cc zirconia grinding tank at 450 rpm for 1 hour with 2 mm diameter zirconia milling media using an attritor mill (Szegvari attritor system, Union Process Inc., USA). The agitator system of the attritor mill consists of a plastic coated stainless steel agitator shaft with zirconia agitator arms, while the grinding tank is enclosed in a water cooled cast aluminum jacket with polymer-coated spout ring.

After the milling process, the slurry was filtered to remove the milling media, and then the wet powder was dried in an oven at 60 °C overnight. The dried cake

obtained was crushed and ground into loose powder using a mortar and pestle. The powder was then sieved through a 212 μm stainless steel mesh sieve to pulverize the soft aggregation.

3.3 Powder pressing and compaction

In the preparation of samples, 3 and 4 g of the undoped and MnO_2-doped 10Sc1CeSZ powder was uniaxially pressed at 5 MPa in a steel mold and die set to make disc samples (20 mm diameter) and bar samples (32 mm x 13 mm), respectively. The green compacts were then subjected to cold isostatic pressing (CIP) at 200 MPa for 1 minute. Prior to sintering, the mass, height and diameter measurements were taken for sample volume/ mass determinations.

3.4 Sintering

The sintering behavior of 10Sc1CeSZ samples prepared via conventional and rapid microwave heating process was investigated in this study.

3.4.1 Conventional sintering

The conventional heating was performed in air in a tube furnace (LT Furnace, Malaysia) at various temperatures ranging from 1300 °C to 1550 °C, at 50 °C intervals, with 2 hours holding time at a heating rate of 10 °C/min. A heating profile for the sintering process employed in this study is shown in Figure 3.1. The samples were heated up to the isothermal sintering stage at 1300 – 1550 °C with a dwell time of 2 hours, during which majority of the densification and microstructure development took place, which was then followed by a slow cooling in furnace.

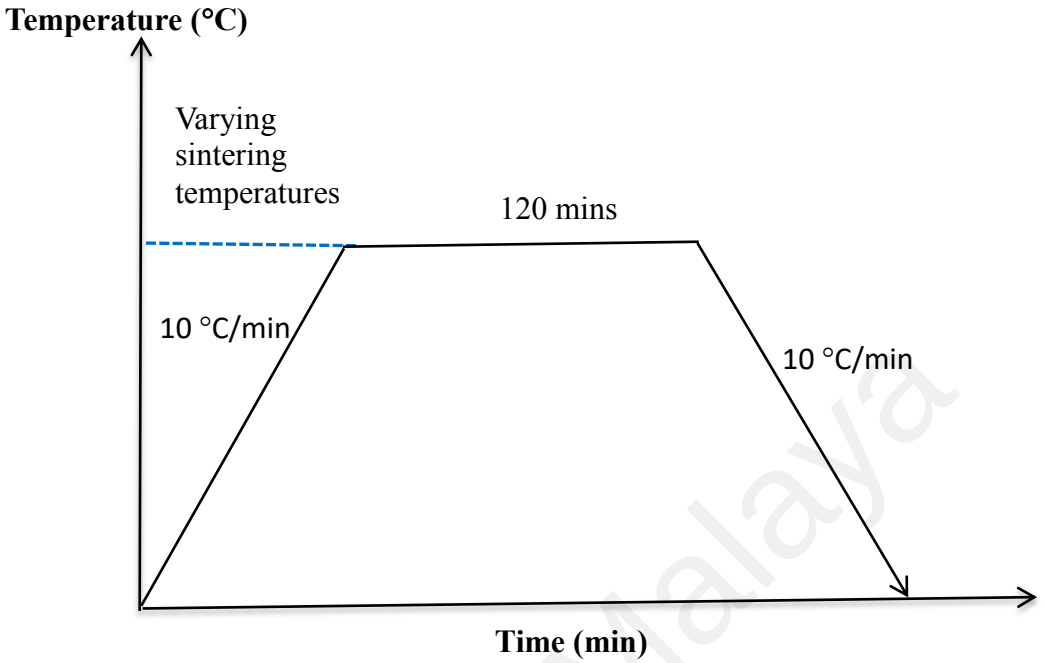

Figure 3.1: Conventional sintering profile adopted for the firing of green bulk zirconia samples.

The development of microstructure during sintering is affected by fusion process between particles. Quenching is employed to freeze the stage of fusion at high temperature to investigate the particle diffusion and bonding process in sintering stages (German et al., 2009).

In this work, a quenching experiment on 10Sc1CeSZ samples were carried out at 1200 °C by removing the sample rapidly from a furnace and cooling it by using ice cool water. The samples subjected to the rapid cooling procedure were found to be able to freeze the microstructural features that could provide an understanding of sintering kinetics and this knowledge can be used to improve the ceramic materials design.

3.4.2 Microwave sintering

For comparison purpose, selected zirconia were microwave sintered at 1300 °C and 1350 °C for 15 minutes at a heating rate of 30 °C/min. in a 2.45-GHz 2-kW microwave furnace (DeltaMF, China).

Due to dielectric loss increases with the sample temperature, the spontaneous heating with microwave needs to be spurred by using a susceptor such as silicon carbide (SiC) (Raj et al., 2011). Susceptors can help to improve the energy efficiency of microwave processing by providing a two-way heating to raise the temperature of the microwave transparent materials to a regime where it becomes susceptible to microwave heating, as well as reducing heat losses from the surface of the material (Bhattacharya & Basak, 2016). SiC is an excellent microwave-coupling material with a loss factor value of 180 at 800 °C, whereas zirconia ceramics transform to an excellent microwave absorbing material only at temperatures above 500 °C, with a much lower loss factor of less than 10 at 600 °C, and increased to 93 at 1200 °C (Bhattacharya & Basak, 2016; Zhao et al., 2000).

The microwave sintering was carried out by positioning evenly-spaced SiC rods in the picket-fence arrangement around the zirconia ceramic samples within a casket of an alumina based insulation in microwave furnace.

3.5 Characterization

3.5.1 Brunauer–Emmett–Teller (BET) surface area

The particle size analysis is important to provide better insight for discernment and understanding of the sintering behavior in the particulate materials processing and the

associated properties of the ceramics. The surface area of a material can be determined by measuring the volume of nitrogen gas adsorbed at various low-pressure levels by the sample.

The specific surface area of all the scandia stabilized powders was measured using the single point Brunauer–Emmett–Teller **(**BET) method on a Micrometrics (Tristar II) surface area analyzer by nitrogen gas adsorption at 77 K in accordance to ASTM D 3663-03 (2008). The samples were outgassed at 90 °C for at least 1 hour with dry nitrogen purge. The BET equivalent particle diameter, d_{BET} was estimated by assuming monodisperse, spherical and non-aggregated particles using Equation 3.1 (Heel et al., 2009):

$$\text{Average particle size, } d_{BET} = \frac{6}{\rho S_{BET}} \tag{3.1}$$

where ρ is the theoretical density of 10Sc1CeSZ, and S_{BET} is the BET specific surface area.

3.5.2 Density measurement

The density of the sintered compacts was measured by the water immersion technique based on the Archimedes principle. An analytical balance (Shimadzu AY220, Japan) was used in this work. The temperature of the water was controlled at 25°C. The density of the specimen was calculated by using Equation 3.2:

$$\rho = \frac{M}{M - M_w} \text{ x } \rho_w \tag{3.2}$$

where ρ is the density of specimen, M is the weight of specimen in air, M_W is the weight of specimen submerged in distilled water, and ρ_W is the density of water taken as 0.99676 g/cm^3.

The relative density was then determined through dividing the determined density by the theoretical density of the scandia stabilized zirconia ceramics (5.74 g/cm^3).

3.5.3 X-Ray Diffraction (XRD)

X-ray diffraction measurements were used to characterize the crystallographic structures of both 10Sc1CeSZ powder and sintered samples.

The phase analysis by X-ray diffraction (XRD) of the ceramics was carried out using a PANalytical Empyrean (The Netherlands) X-ray diffractometer with CuK_α as the radiation source (λ = 1.5406 Å) operated at 45 kV, 40 mA, a step size of 0.02° over a 2θ = 20°- 80°, with 60 seconds scan step time. Phase identification was accomplished by comparison with JCPDS-ICDD (Joint Committee of Powder Diffraction Standard – International Centre for Diffraction Data) files #89-5485, #89-5486, #01-083-0940, #01-083-1376 corresponding to cubic, rhombohedral, monoclinic and tetragonal phases respectively. The details of the JCPDS-ICDD reference files are attached in the Appendix A.

3.5.4 Microstructural evolution and grain size measurement

Scanning electron microscope (SEM) was used to characterize the grain size and morphology of the synthesized powders and sintered powder compact of 10Sc1CeSZ samples. Prior to the SEM analysis, the cylindrical sintered samples were grinded using

240-1200 grit SiC sandpaper and then polished to mirror finish using diamond paste with grits ranging from 3 μm and 1 μm. Samples were placed in an isolated alumina crucible to prevent cross contamination and thermally etched at temperature 50 °C lower than the sintering temperatures at 10 °C/min with 30 minutes holding time, to reveal the grain boundaries.

Microstructure characterization was performed by using scanning electron microscopy for acquiring images of surface and cross-section microstructure of the zirconia ceramics. The quenched samples were fractured manually to observe the cross-section view. Field-emission scanning electron microscope (Zeiss Auriga FESEM, Germany) was used to observe the morphology of nanosized-powders, for its improved resolution and minimized sample charging, while SEM (Phenom Pro SEM, Netherland) was used on polished and thermally etched sintered pellets, operating at 5- 20 kV. The samples were mounted on an aluminum stub using carbon tape. Micrographs were taken between magnifications of x1K to x50K. During these observations, energy dispersive X-ray spectroscopy (EDS) quantitative analyses were performed in order to analyse the chemical composition and detect the presence of impurities.

Grain size measurements were performed on SEM micrographs using the Mendelson line intercept method with at least 50 intercepts per micrograph, in accordance ASTM E112-96, and a stereographic projection factor of 1.56 (Mendelson, 1969; ASTM E112-96, 2004).

3.6 Mechanical testing

Mechanical property plays a crucial role in sustaining the structural safety and integrity of advanced ceramic components during its operation. High fracture toughness and low Young's modulus are found to be favourable in preventing crack propagation

induced by thermal stress (Zhang et al., 2013). The Vickers hardness indentation fracture test has been a popular experimental technique to characterize the fracture resistance of brittle materials. The cracks generated from the Vickers hardness indentation is used to compute fracture toughness with the crack lengths in inverse proportion to toughness. The technique is a non-destructive, simple and convenient way to determine hardness and fracture toughness, with minimal machining during sample preparation.

3.6.1 Vickers hardness

Figure 3.2 shows the two most common types of cracks geometry generated from the indentation. One is the halfpenny shaped crack system (also called median or radial-median crack system) and the other is the Palmqvist crack system. If one polishes away the surface layers, the median cracks would remain connected to the corner of the diagonal while the Palmqvist cracks would become detached (Barsoum, 2002).

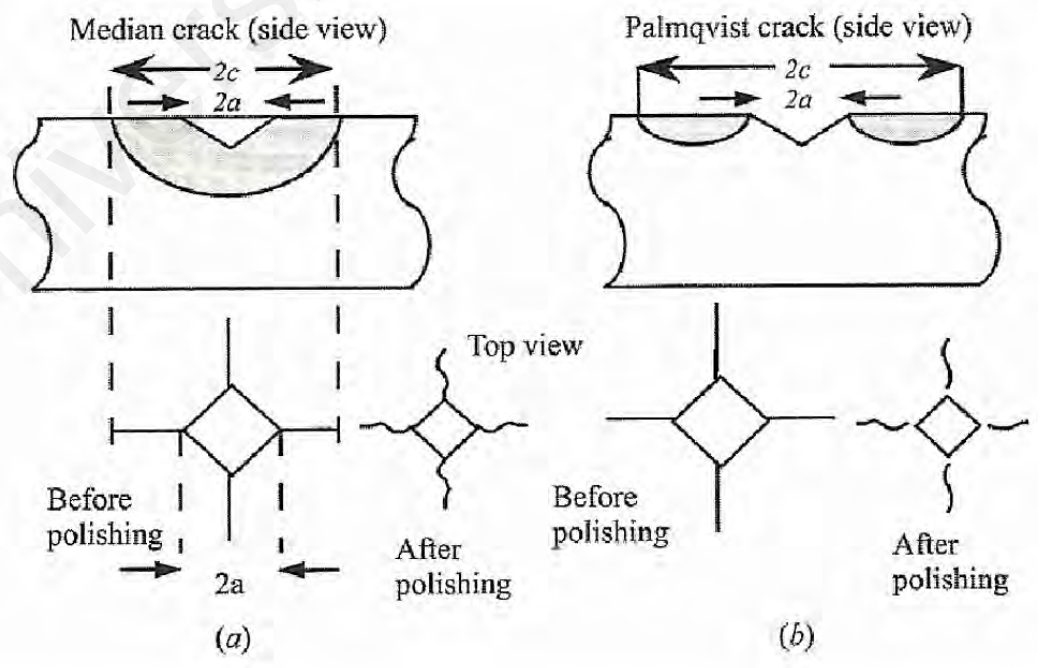

Figure 3.2: Two types of crack geometries induced by Vickers hardness indentation (Barsoum, 2002).

Vickers hardness test involves the measurement of a square-based pyramid diamond indenter pressed into a polished surface by a fixed load in accordance to ASTM C1327-08 (ASTM C1327-08, 2008) standard. In this study, the diagonal lengths of the indentation were made on the mirror-polished samples using a Mitutoyo Vickers hardness tester (AVK-C2) at an applied load of 10 kgf with a dwell time of 10 seconds. For each sample, at least five (5) indentations were used to obtain the average hardness and standard deviation value. The diagonal size of the resultant indentation on the surface of the test sample was measured with the help of an optical microscopy after unloading and the Vickers hardness value was calculated as the ratio of the applied load to the pyramidal contact area, as shown in Equation 3.3:

$$Hv = 1.854\ \frac{F}{d^2} \tag{3.3}$$

where H_V is the Vickers hardness; F is the indentation load; and d is average diagonal length of the resultant impression (shown as '2a' in Figure 3.2).

3.6.2 Fracture toughness

The fracture toughness (K_{Ic}) value of sintered samples was then determined from the Vickers hardness indentation measurement, by measuring the crack lines emanated from the four corners of the pyramidal indentation. The crack lengths were immediately measured after the indentation to prevent slow crack growth after unloading. The cracks in the zirconia ceramic samples were found to be of palmqvist type with low crack-to-indent ratio size (L/a < 3), and no spalling observed at the indentation imprints. K_{Ic} was computed using the Equation 3.4 derived by Niihara et al. (1982):

$$\left(\frac{K_{Ic}\varphi}{H_V\, a^{1/2}}\right)\left(\frac{H_V}{E\varphi}\right)^{2/5} = 0.035\,\left(\frac{L}{a}\right)^{-1/2} \tag{3.4}$$

where K_{Ic} is the fracture toughness, Hv is the Vickers hardness, E is the Young's modulus, a is the half length of the average diagonal, L is the average crack length= (L_1 +L_2 +L_3 +L_4)/4 and φ is the constraint factor which is taken as 3 (Evans & Charles, 1976).

3.6.3 Young's modulus

The Young's modulus by sonic resonance was determined for rectangular bar samples (32 mm x 13 mm x 4 mm) using a commercial testing instrument (GrindoSonic: MK5 "Industrial", Belgium) according to ASTM E1876-09 (ASTM E1876-09, 2009). The equipment permits determination of the resonant frequency of a sample by monitoring and evaluating the vibrational harmonics of the sample. The sample was placed over 2 supporting rubber cylindrical rods and lined up with a transducer. The frequency was obtained by striking the samples mechanically using a small hammer to generate singular elastic tapping. The modulus of elasticity or Young's modulus was calculated using experimentally determined resonant frequency as shown in Equation 3.5:

$$E = 0.9465\left(\frac{mF^2}{w}\right)\left(\frac{L}{t}\right)^3 T \tag{3.5}$$

$$T = 1 + 6.585\left(1 + 0.0752\mu^2\right)\left(\frac{t}{L}\right)^2 - 0.868\left(\frac{t}{L}\right)^4 - \frac{8.34\left(1 + 0.2023\mu + 2.173\mu^2\right)\left(\frac{t}{L}\right)^4}{1 + 6.338\left(1 + 0.1408\mu + 1.53\mu^2\right)\left(\frac{t}{L}\right)^2} \tag{3.6}$$

E = Young's modulus

m = Mass of bar

F = Fundamental resonant frequency of bar in flexural (Hz)

w = width of bar

L = Length of bar

t = Thickness of bar

T = Correction factor for fundamental flexural mode to account for finite thickness of bar

μ= Poisson ratio, taken as 0.23 for stabilized zirconia (Shackelford et al., 2016)

3.7 Electrochemical Impedance Spectroscopy

Electrochemical Impedance Spectroscopy (EIS) is one of the most effective methods to evaluate the conductivity of ionic conductor. Electrochemical impedance is usually measured by applying an AC potential to an electrochemical cell and then measuring the current through the cell to characterize distinct regions of a sample according to their electrical relaxation times (Irvine et al., 1990). Different components of a material are normally characterized by a parallel resistance (R) and a capacitance (C) from the dielectric data directly extracted from the measured complex impedance, $Z(\omega) = Z'(\omega) + jZ''(\omega)$. The characteristic relaxation time or time constant, τ, of each parallel RC element is given by the product of R and C:

$$\tau = RC \tag{3.7}$$

$$\omega_{max} RC = 1 \tag{3.8}$$

Where R values are obtained from the intercepts on the Z' axis, C values are obtained by applying Equation 3.8. ω_{max} is the angular frequency at maximum of each semicircle ($\omega_{max} = 2\pi f$).

The magnitude of the excitation signal applied in the EIS system is usually small (1-10 mV) to ensure that the electrode's response is in a pseudo-linear potential region, as shown in Figure 3.3, causing no destructive damage to the electrode (Revankar & Majumdar, 2014; Yuan et al., 2009).

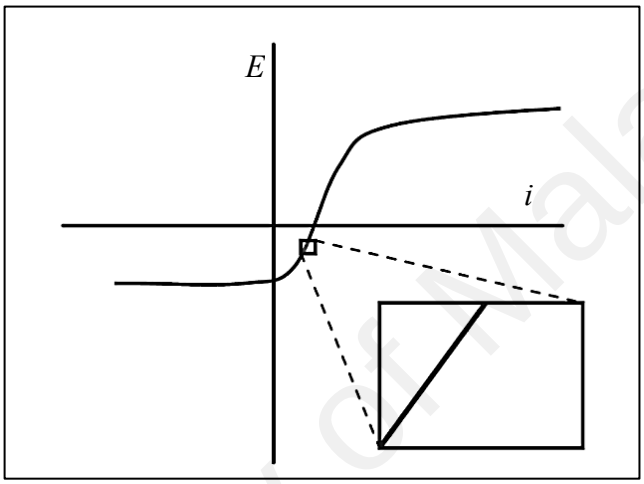

Figure 3.3: E-i curve showing pseudo-linearity (Revankar & Majumdar, 2014).

In this work, Electrochemical Impedance Spectroscopy (Metrohm Autolab EIS, Switzerland) potentiostat was used to measure the AC impedance spectra of the sintered pellets at the temperature range of 600- 800 °C. For this purpose, the cylindrical edges of the zirconia pellets were masked with tape and a commercial silver conductive paint (RS 186-3-596) was deposited onto each of the circular faces, and fired at 150 °C for 30 minutes to ensure a good bond between the sample surfaces and the silver electrode. The choice of electrode depends on the temperature of investigation and the type of conductivity that is being investigated. Platinum and gold electrodes perform well at high temperatures, but they are relatively blocking to oxygen at lower temperatures.

Therefore silver electrodes are chosen because they have lower electrode impedance (Barsoukov & Macdonald, 2005).

Each silver electrode-coated sample was sandwiched between platinum gauze and then connected to two electrodes via platinum wires to a frequency response analyzer (Autolab AUT 302 FRA). The cell fixture containing the Pt/Electrolyte/Pt was subsequently loaded into a tube furnace (CTF 12/65/550 Carbolite, UK) where two-point impedance test were performed in the temperature range from 600-800 °C in air. At each measuring temperature, the specimen was thermally stabilized for 1 hour before EIS impedance measurement. The impedance diagrams were recorded over a frequency range of 0.1 Hz to 1 MHz, at an 10 mV AC peak-to-peak sinusoidal potential. By imposing the small amplitude sinusoidal voltage, the electrode potential will have a perturbation near the equilibrium electrode potential. When it comes to a steady state, the amplitude and phase variation of responded current signal was measured at the preset frequency range.

The measured AC impedance data, plotted as Nyquist graphs, which reflects the relationship between the real part (resistive, Z') and imaginary part (capacitive, Z") of the impedance in the complex plane within the frequency range, was fitted using the Nova software. The bulk and grain boundary resistance were subsequently obtained from equivalent circuit fitting of parallel RQ (R-Resistance, Q-Constant Phase Element) in series and the specimen conductivity was computed.

The influence of the grain boundary conductivity in the total conductivity can be evaluated through the blocking factor (α_R) defined from the impedance diagram parameters by: (Rajeswari et al., 2011)

$$\alpha_R = \frac{R_{gb}}{R_g + R_{gb}} \tag{3.9}$$

where R_g and R_{gb} are grain and grain boundary resistivities respectively. This factor gives the fraction of the electric carriers being blocked at the impermeable internal surfaces, under the measuring conditions, with respect to the total number of electric carriers in the sample.

CHAPTER 4: RESULTS AND DISCUSSION

4.1: Introduction

The first part of the study in this chapter compared the mechanical and electrical properties of sintered 10Sc1CeSZ compacts prepared from commercially available powder and the powder synthesized via solid state reaction. The second part of this chapter discussed the effect of additions of different amount of MnO_2 dopants on the densification, phase stability and mechanical properties of the 10Sc1CeSZ ceramics prepared by attritor milling using mechanochemical mixing method. The last part of this chapter discussed the microwave sintering behavior of 10Sc1CeSZ ceramics relative to conventional sintering.

4.2: Part 1: Comparison between commercial and synthesized 10Sc1CeSZ samples

The following results present the comparison between the microstructural changes, phase stability, mechanical and electrical properties of commercially available 10Sc1CeSZ and the synthesized zirconia ceramics produced via solid state reaction. After a detail comparison was made between the two powders, the powder with higher phase stability and better sintering properties was adopted for the experimental works in the subsequent parts of this research.

4.2.1: Particle size analysis and powder surface morphology

The BET specific surface area and the average particle size of the 10Sc1CeSZ samples are summarized in Table 4.1.

Table 4.1: BET specific surface area and average particle size of commercial and synthesized 10Sc1CeSZ ceramic powder.

10Sc1CeSZ powder	Commercial	Synthesized
BET specific surface area (m^2/g)	11.53	11.48
Average particle size, d_{BET} (nm)	90.65	91.09

The result revealed that the commercial starting powder, which was a commercially available powder obtained from Daiichi Co. Ltd. Japan, had a BET surface area of 11.53 m^2/g, which is in agreement with the specification supplied by Daichii (11.1 m^2/g). However, in contrast to the submicron size (0.53 μm) stated in the supplier's specification, there was a much smaller average particle size of 90.65 nm observed in the as-received powder. The 10Sc1CeSZ powder synthesized through solid state ball milling process had recorded a similar specific surface area of ~11.5 m^2/g and average particle size of ~91.1 nm.

SEM micrographs in Figure 4.1 (a) shows the particle morphologies of the commercial 10Sc1CeSZ powder, revealing the presence of soft spherical agglomerates of ~30-80 μm in diameter; while Figure 4.1 (b) shows that the synthesized powder consisted of loose agglomerates with randomly distributed flakes of ~10-20 μm in length.

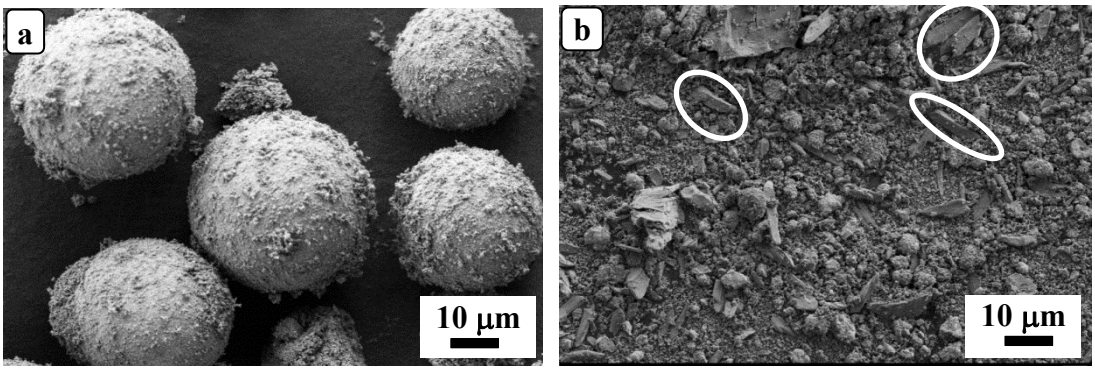

Figure 4.1: SEM micrographs of (a) commercial, (b) synthesized 10Sc1CeSZ powders. The white circle marking in (b) indicating scandia flakes.

Close-up views of the synthesized powder in Figure 4.2 show that the loose agglomerates were in polygonal structure while the flakes-type particles were in the thick plate-like structure. The results of EDS analysis of the synthesized powder in Figure 4.3 indicate that the loose agglomerates of polygonal-shaped particles were mainly pure zirconia while the flaky particles had high scandia content.

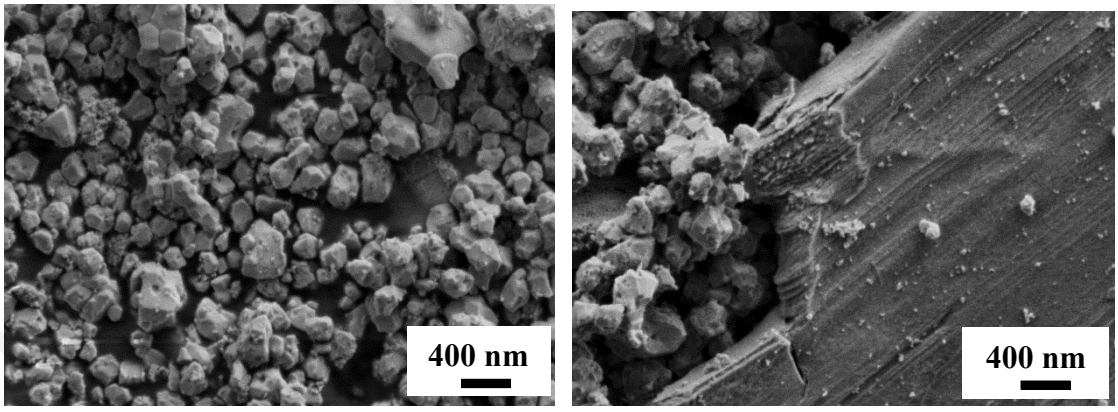

Figure 4.2: Close-up view of FESEM micrographs of synthesized 10Sc1CeSZ powder showing zirconia polygon particles (left image) and scandia flakes in plate-like structure (right image).

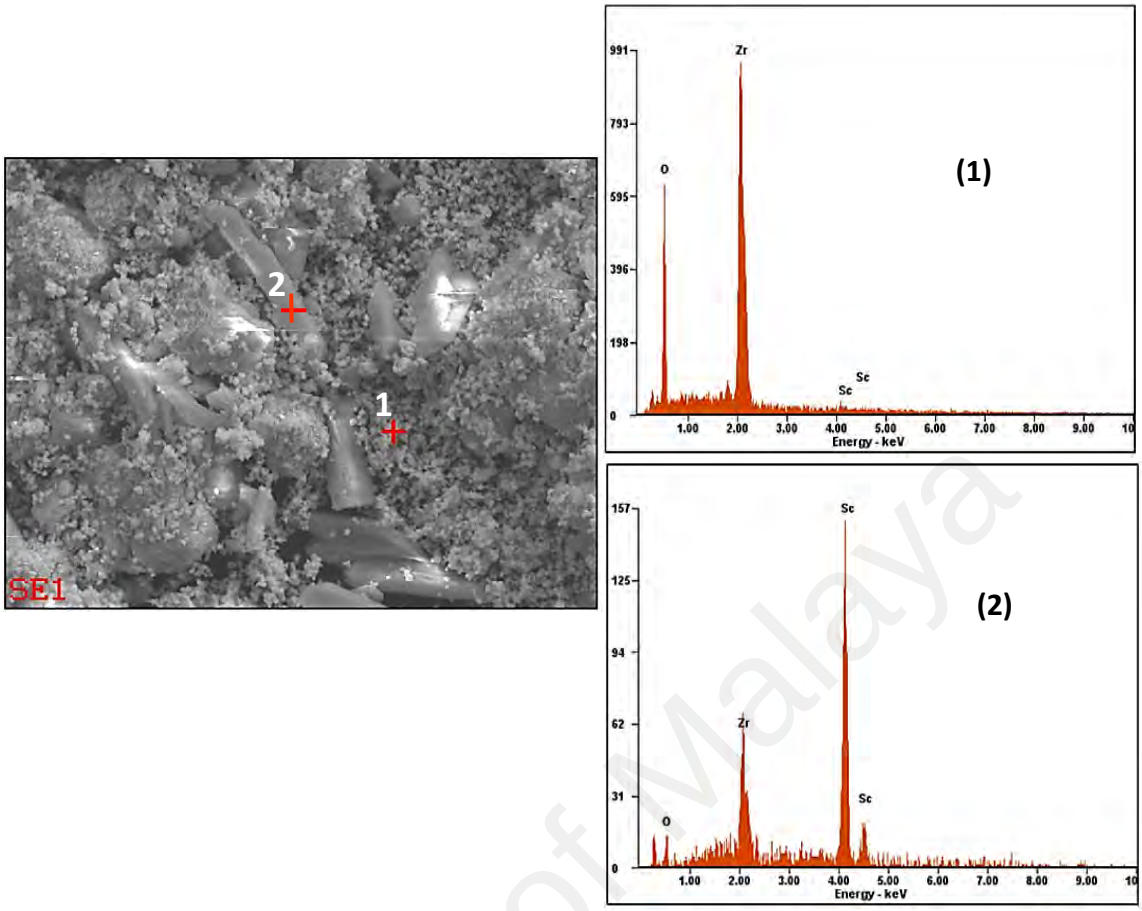

Figure 4.3: EDS analysis on the loose agglomerates (point 1) of synthesized 10Sc1CeSZ powder showing high zirconia content and on a flaky structure (point 2) showing high scandia content.

4.2.2: X-Ray Diffraction (XRD)

Characterizations of crystalline structures of commercial and synthesized 10Sc1CeSZ samples were carried out using XRD to investigate the phase stability of the ceramics.

The XRD plots of the commercial and synthesized 10Sc1CeSZ powders and sintered samples after sintering at 1400 °C to 1550 °C for 2 hours are shown in Figure 4.4 and Figure 4.5, respectively. The crystalline phases were identified by comparing the XRD peaks of the ceramics to that of cubic (JCPDS file: 01-089-5485), rhombohedral (JCPDS file: 01-089-5486), and monoclinic (JCPDS file: 01-083-0940) zirconia phase.

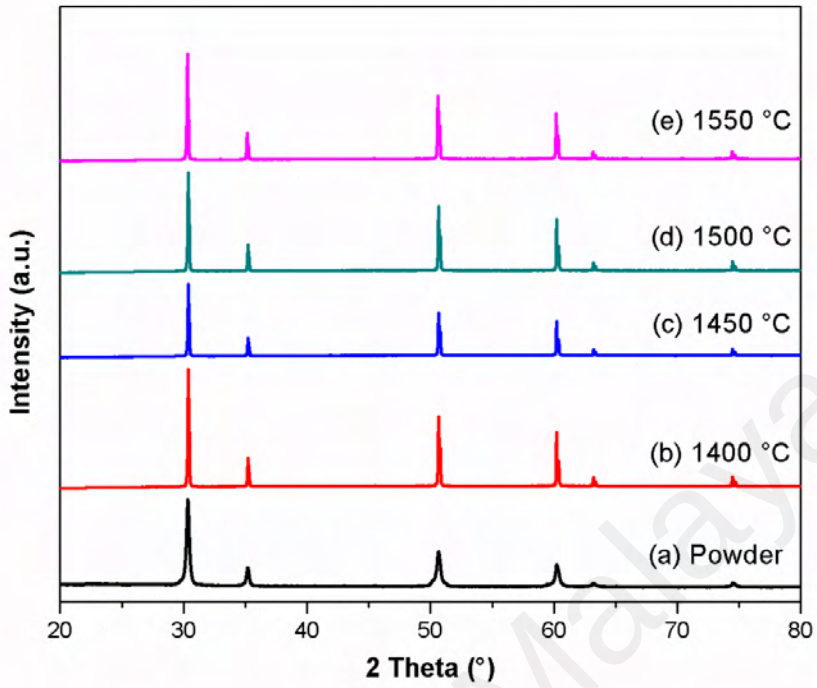

Figure 4.4: The XRD diffractograms of commercial 10Sc1CeSZ powder and compact samples sintered from 1400 °C to 1550 °C for two hours.

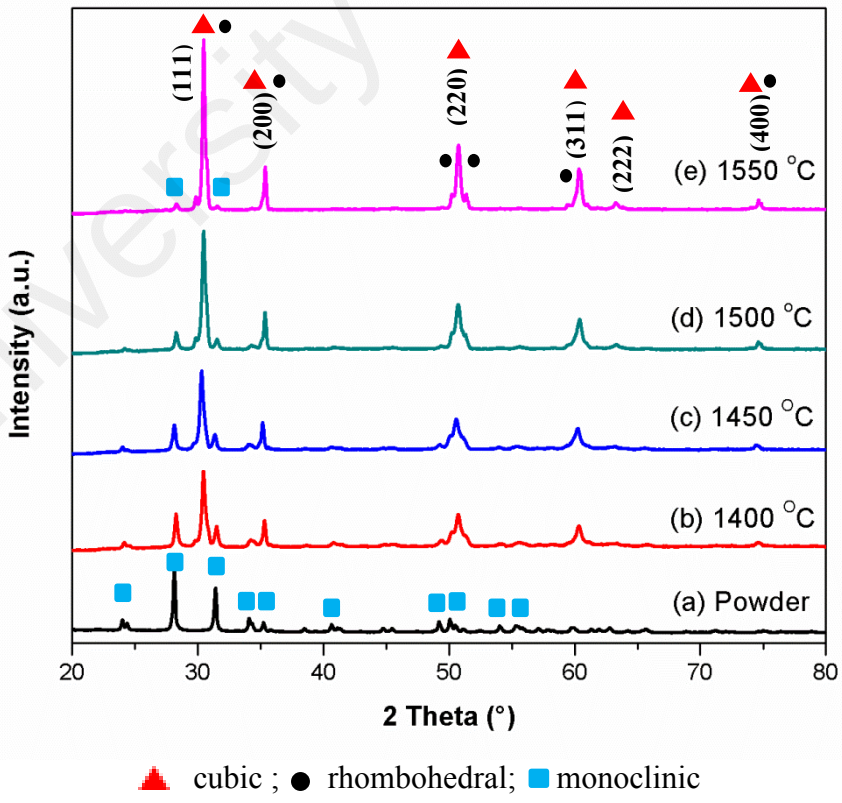

Figure 4.5: The XRD diffractograms of synthesized 10Sc1CeSZ powder and compact samples sintered from 1400 °C to 1550 °C for two hours.

The XRD traces of commercial 10Sc1CeSZ powder and all the sintered compacts in Figure 4.4 revealed pure cubic form regardless of sintering temperature. Badwal et al. (2000) and Haering et al. (2005) reported mixed cubic and rhombohedral phase for undoped 10 mol% scandia stabilized zirconia (10ScSZ) ceramics in their previous studies. Laguna-Bercero et al. (2009) and Liu et al. (2010) reported that the addition of ceria in scandia stabilized zirconia ceramic was found to be able to stabilize the cubic phase at room temperature and suppressed the rhombohedral phase. This is elucidated as the bigger Ce^{4+} cations form eightfold coordination with the O^{2-} anions to create oxygen vacancies within the zirconia ions to stabilize the cubic phase (Mizutani et al., 1999; Ukai et al., 2001; Liu et al., 2010).

On the other hand, the XRD results in Figure 4.5 reveal that synthesized 10Sc1CeSZ powder was in pure monoclinic (space group P21/c) zirconia phase; while its sintered compacts exhibited cubic (space group Fm-3m) phase with some minor peaks detected belongs to monoclinic and rhombohedral (space group R-3) phase, indicating insufficient stabilizing oxides in the zirconia lattice to produce a fully stabilized zirconia ceramic. However, the secondary phase signals were found to reduce with increasing sintering temperatures. It can be seen from Figure 4.5 that as the sintering temperature increases, the cubic phase becomes more prominent as identified from (111), (200), (220), (311), (222), (400) planes, while rhombohedral and monoclinic phase diminishes, suggesting that scandium and cerium atoms have been incorporated into the zirconia lattice to form cubic solid solution at higher temperatures.

4.2.3: Density Measurement

The density measurement was carried out to compare the sinterability of the samples prepared from the commercial and synthesized powders. The relative density is calculated based on the theoretical density of 5.74 g/cm^3 (Rosten et al., 2006). The density results indicated that all the sintered compacts prepared from commercial 10Sc1CeSZ powder were able to achieve ~98 – 99 % relative density (bulk density ~ 5.6- 5.7 g/cm^3), whereas sintered compacts prepared from synthesized powder were only able to attain ~ 82- 87 % relative density (bulk density ~ 4.7 – 5.0 g/cm^3) in the entire range of 1400 °C to 1550 °C sintering temperatures. This demonstrated that commercial powder had higher sinterability.

4.2.4: Microstructural Evolution

SEM micrographs of the commercial and synthesized 10Sc1CeSZ samples sintered at 1450°C and 1550 °C in air for 2 hours are shown in Figure 4.6. It can be seen that the grains were completely developed in the commercial 10Sc1CeSZ ceramic samples when sintered at 1450 °C and 1550 °C, as shown in Figure 4.6 (a-b). The soft spherical agglomerates in the as-received commercial powder consisted of an aggregate of finer particles (Figure 4.1) and were homogeneously packed to maximize particle contacts in the powder compacts, thus creating many grain boundaries and short diffusion paths for rapid matter transport during sintering (De Jonghe & Rahaman, 2003).

By contrast, the microstructures in Figure 4.6 (c-d) show that the grain boundaries were not fully developed for the compact samples prepared from synthesized powder under the same sintering conditions. Figure 4.6 (c) reveals that the sintering process was in the initial stage of densification when the zirconia ceramic sample was sintered at

1450 °C, while Figure 4.6 (d) shows that grain coarsening started to become significant when the sintering temperature was increased to 1550 °C, accompanied by reduction of closed and isolated pores. Randomly distributed pores observed in the synthesized samples might be created due to large scandia flakes that caused the powders to be loosely compacted and eventually affects the sinterability of the green compacts. This was manifested by the low relative density (below 90% of theoretical density) as depicted in the density measurement.

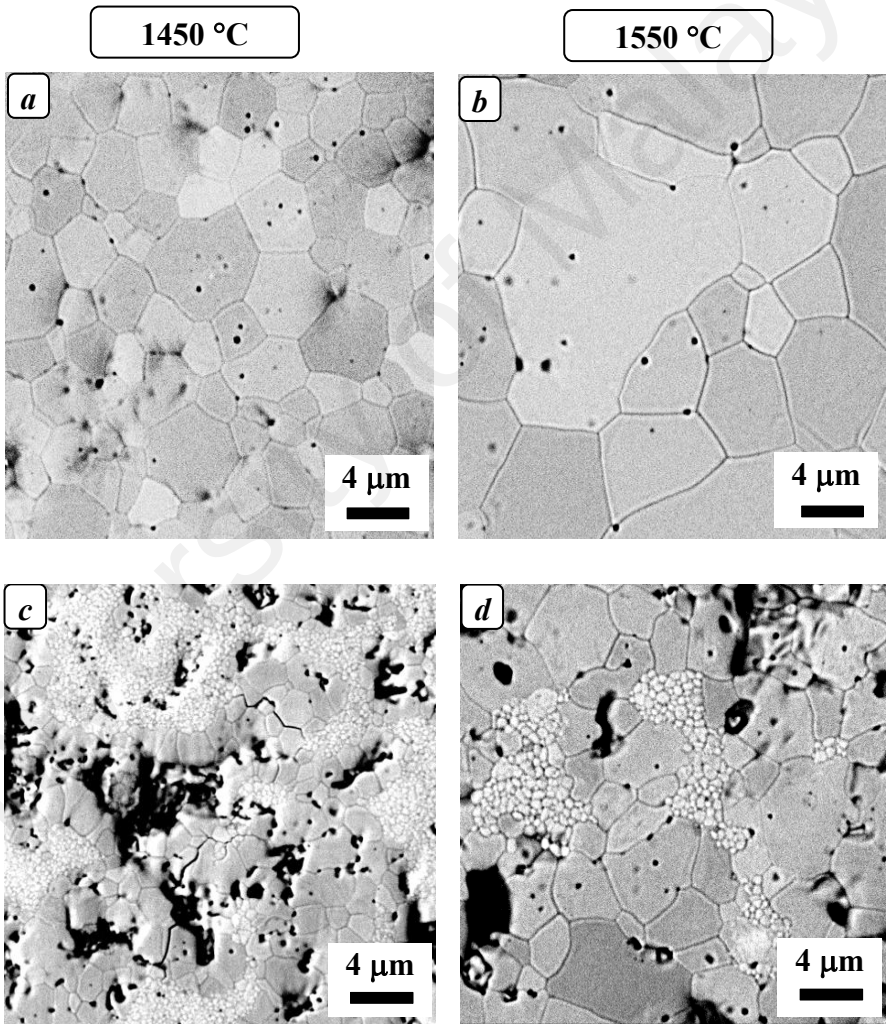

Figure 4.6: SEM micrographs of commercial (a to b), and synthesized (c to d) 10Sc1CeSZ ceramics sintered at 1450 °C and 1550 °C for 2 hours.

4.2.5: Mechanical Properties

The mechanical property trends of the 10Sc1CeSZ samples were in agreement with their density trends. The Vickers hardness and Young's modulus values of the sintered compacts prepared from synthesized powder vary from 4.6- 6.0 GPa and 110-140 GPa, respectively, which were found to be lower than the values of samples prepared from commercial powder that recorded a higher Vickers hardness and Young's modulus values of 13-13.5 GPa and 180-200 GPa, respectively. The mechanical properties of 10Sc1CeSZ ceramics prepared from the commercial powder were comparable with the reported values of YSZ in the literature (Morales et al., 2010), the most widely investigated electrolyte material for SOFCs (Orera & Slater, 2009).

4.2.6: Electrochemical Impedance Spectroscopy (EIS)

Recent research on SOFC has been focusing on reducing the operating temperature to 500 – 800 °C to eliminate the need to use the expensive material for interconnects and heat exchangers and to reduce thermal degradation (Brandon et al., 2004; Jacobson, 2009). For scandia stabilized zirconia system, studies have shown that the rhombohedral phase would transform to cubic phase at about 550 °C (Haering et al., 2005; Sarat et al., 2006). Cubic phase has a more open structure compared to rhombohedral phase which would increase the mobility of oxygen vacancies. Therefore, better electrical conductivity would be expected when the scandia stabilized zirconia ceramics are tested at 550 °C and above.

Figure 4.7- 4.8 show the EIS impedance spectra in Nyquist plots for 10Sc1CeSZ ceramics prepared from commercial and synthesized powder, respectively. The impedance spectra were recorded at three different temperatures, 600 °C, 700 °C, and

800 °C, after each sample was stabilized at the specific temperatures for one hour. The EIS impedance measurement data are presented in the form of imaginary, Z″ (capacitive) against real, Z′ (resistive) impedances. To identify the constituent component of a material, different regions of the electrical system are usually characterized according to their electrical relaxation times by a parallel resistance and capacitance (RC) to extract the R and C values of each semicircle on the impedance plots (Irvine et al., 1990).

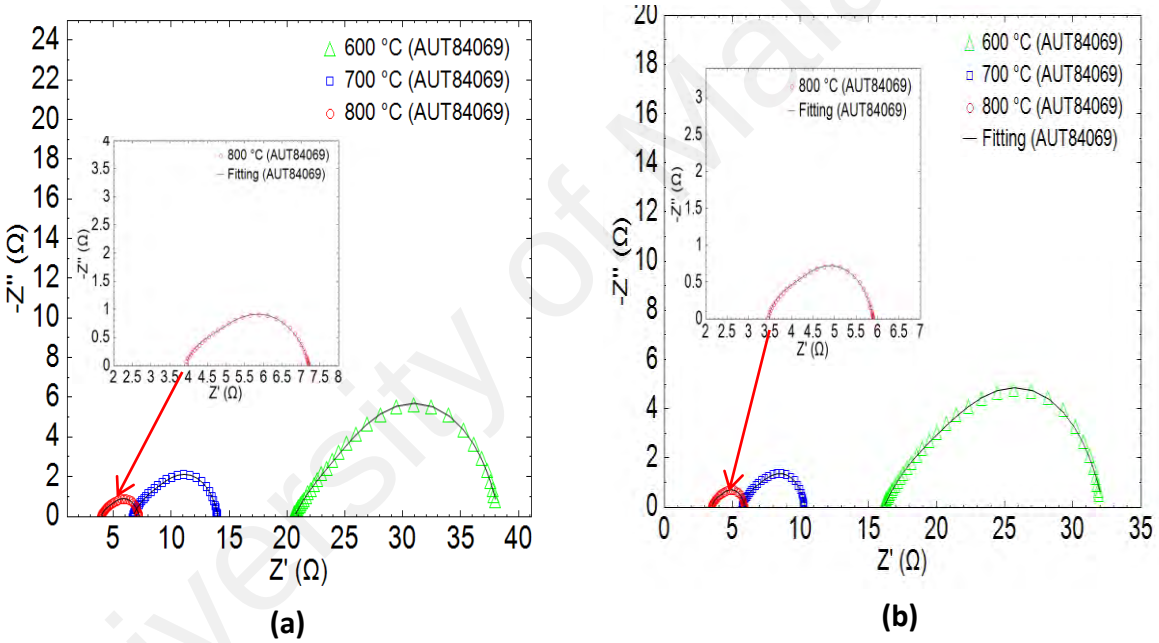

Figure 4.7: Nyquist plots taken at varying temperatures for 10Sc1CeSZ samples prepared from commercial powder sintered at (a) 1500 °C, (b) 1550 °C.

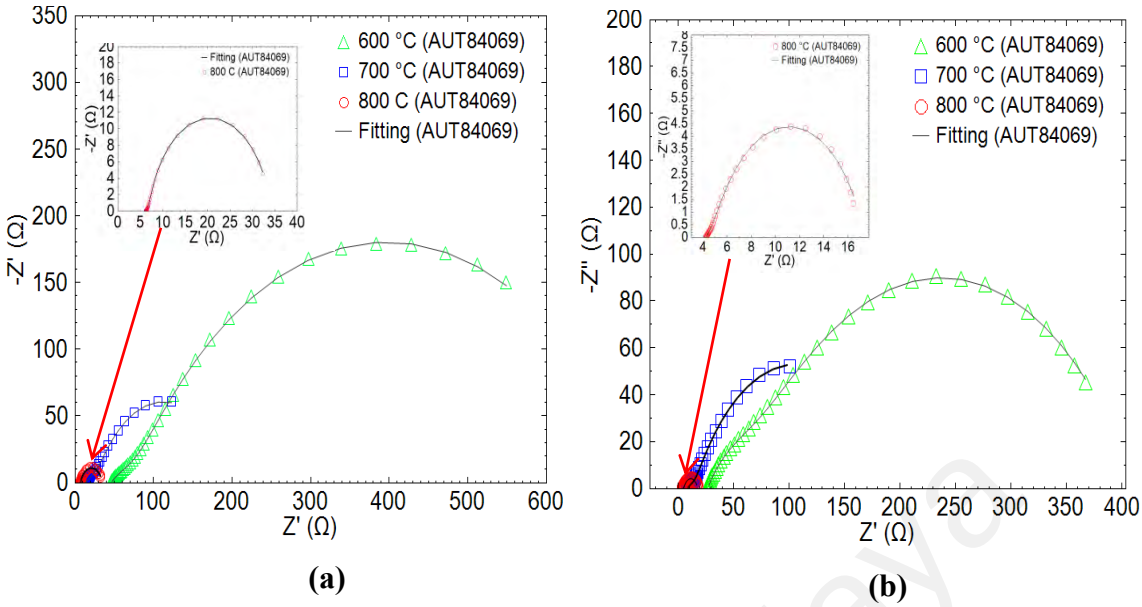

Figure 4.8: Nyquist plots taken at varying temperatures for 10Sc1CeSZ samples prepared from synthesized powder sintered at (a) 1500 °C, (b) 1550 °C.

In this study, depressed arcs instead of ideal semicircles were observed in the impedance spectrum, signifying non-ideal capacitive behavior due to the distribution of currents and electroactive species (Lvovich, 2012). Each depressed arc is therefore fitted with a parallel resistance and constant phase element (R-Q) to replace the ideal capacitive property. The associated R values obtained from the high frequency intercepts on the real axis are attributed to the bulk resistance of the sample, the intermediate frequency arcs are attributed to grain boundary resistance, and the low frequency arcs are attributed to the electrode resistance. It can be observed that the bulk impedance obtained at high frequency incepts of all 10Sc1CeSZ samples reduced with increasing operating temperatures, indicating improved bulk conduction at higher temperatures.

Figure 4.9 shows the blocking factor for 10Sc1CeSZ compacts sintered at 1400 °C to 1550 °C, depicting the grain boundary resistivity contribution of both samples when measured at 600 °C, 700 °C, and 800 °C. High blocking factor in the low sintering

temperature range (1400- 1450 °C) for samples prepared from commercial powder shown in Figure 4.9 (a) implied that smaller grain size resulted in higher proportion of grain boundary area and hence higher grain boundary resistivity. It can be seen that the grain boundary blocking effect became less pronounced when measured at 800°C, signifying improved grain boundary conductivity at higher operating temperature.

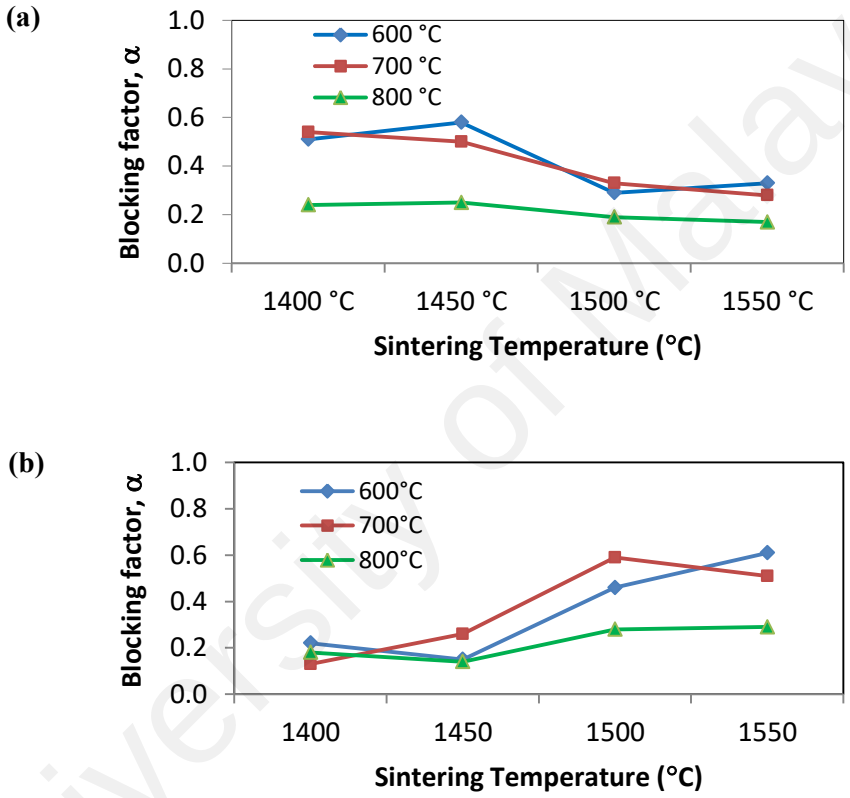

Figure 4.9: Block factor (α_R) measured at 600 °C, 700 °C, and 800 °C for 10Sc1CeSZ samples prepared from (a) commercial, (b) synthesized powders sintered at 1400 °C to 1550 °C.

In contrast, the results in Figure 4.9 (b) shows that the samples prepared from synthesized powder had lower blocking factor when sintered at 1400 - 1450 °C, caused by high bulk resistivities. This was due to the samples produced from synthesized powder were not fully dense with low sintering temperatures. However, the blocking factors were observed to increase with higher sintering temperatures, indicating better

bulk conductivities when the samples became denser at higher sintering temperatures. Both bulk and grain boundary resistances decreased with increasing operating temperatures, which could be explained from the defects dissociation with the cations, in which oxygen vacancies are able to be freed from the attachment to cations for conduction at higher temperature (Haering et al., 2005; Zhang et al., 2007).

Figure 4.10- 4.11 show the temperature dependence electrical conductivities of 10Sc1CeSZ ceramics prepared from synthesized and commercial powder, respectively, based on the Arrhenius equation $\sigma T = A \exp(\frac{-E_a}{kT})$. The total electrical conductivity, $\sigma = (\frac{L}{RA})$ was calculated based on the resistances obtained from the equivalent circuit, where R = bulk resistance and grain boundary resistance, L = sample thickness, and A = contact surface area between the sample and the electrode.

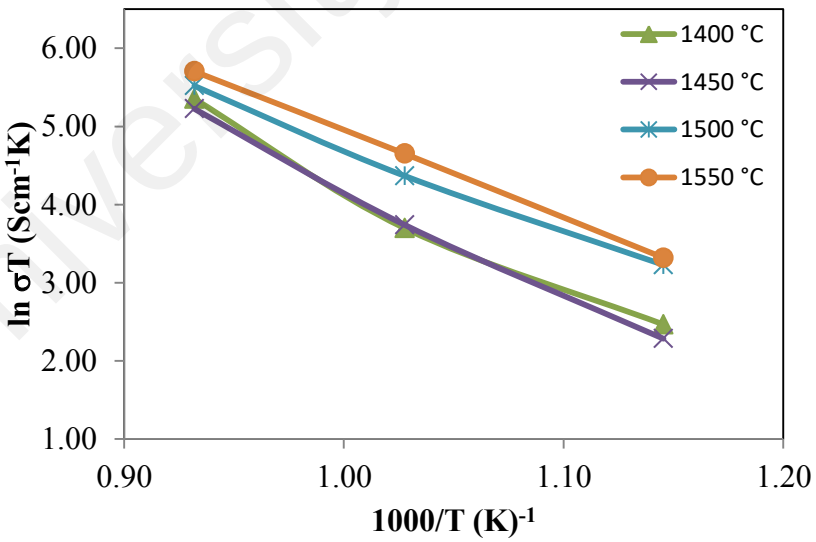

Figure 4.10: Arrhenius Plots depicting temperature dependencies of electrical conductivities for commercial 10Sc1CeSZ samples with silver paste electrodes.

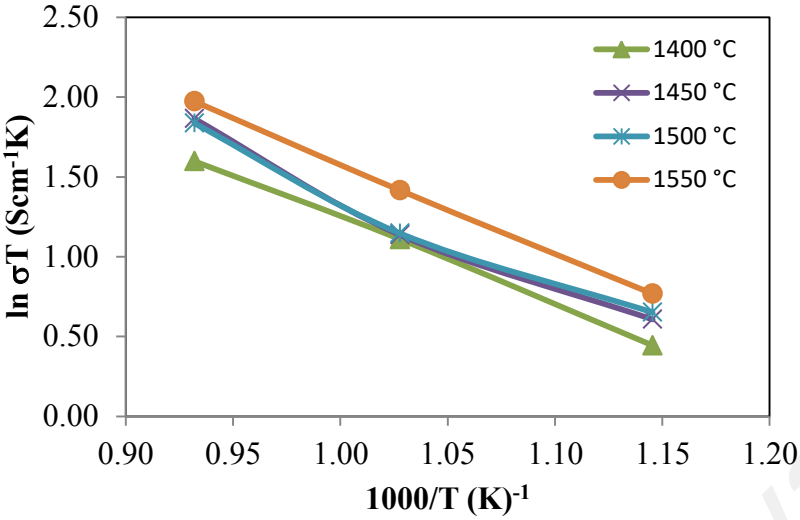

Figure 4.11: Arrhenius Plots depicting temperature dependencies of electrical conductivities for synthesized 10Sc1CeSZ samples with silver paste electrodes.

Electrolyte should have ionic conductivities of higher than 0.02 S/cm at 700 °C for high output performance in SOFC application (Hiwatashi, 2009). All the 10Sc1CeSZ samples prepared from synthesized powder showed an ionic conductivity value of less than 0.02 S/cm at 700 °C except for the sample sintered at 1550 °C, which recorded a conductivity of 0.03 S/cm at 700 °C and increased to 0.09 S/cm at 800 °C. This is comparable with the results reported in previous studies carried out on the scandia stabilized zirconia (Haering et al., 2005; Liu et al., 2010). The conductivity of the 10Sc1CeSZ samples prepared from commercial powder were found to be higher than the synthesized one and this indicated that cubic phase exhibits higher conductivities than rhombohedral phase.

4.3: Part 2: Comparison between undoped and MnO_2-doped 10Sc1CeSZ samples

This section explains the effect of manganese oxide (MnO_2) additions (0, 0.5, 1 and 5 wt%) on the densification, phase stability, and properties of ceria-doped scandia stabilized zirconia (10Sc1CeSZ) ceramic. Commercial powder would be employed in all the subsequent part of this research owing to its better sintering properties compared to synthesized powder as deliberated in the earlier study.

4.3.1: Particle size analysis and powder surface morphology

The BET specific surface areas and the average particle size of the undoped and MnO_2-doped 10Sc1CeSZ samples are summarized in Table 4.2.

Table 4.2: **BET specific surface area and average particle size of undoped and MnO_2-doped 10Sc1CeSZ ceramics**

MnO_2 addition (wt%)	**0**	**0.5**	**1**	**5**
BET specific surface area (m^2/g)	11.53	12.88	11.85	11.97
Average particle size, d_{BET} (nm)	90.65	81.17	88.23	87.31

The results indicated that all MnO_2-doped powders showed higher specific surface area as compared to the undoped powder. The BET surface area was at a maximum of 12.88 m^2/g for 0.5 wt% MnO_2 doped zirconia (i.e. 11.7% higher than the undoped ceramic), while the 1 and 5 wt% MnO_2 additions had produced specific surface area of ~3 to 4 % higher than the undoped powder.

Figure 4.12 and 4.13 show the low and high magnification FESEM imaging of the as-received undoped and MnO_2-doped 10Sc1CeSZ powders, respectively.

It can be observed that the starting powder mainly consisted of spherical agglomerates/ granules of ~30- 80 μm in diameter (Figure 4.12 (a)), while attritor-milled MnO_2-doped powders were made of irregular-shaped loose aggregates (Figure 4.12 (b-d)). It can be seen that the clusters are broken and the powder is deagglomerated after milling. This shows that the attritor milling was beneficial in reducing the particle size and hence preventing agglomeration from taking place. Closed up FESEM imaging in Figure 4.13 revealed that the average particle size within the agglomerates of all 10Sc1CeSZ powders were less than 100 nm, which is consistent with the calculated average particle size presented in Table 4.2.

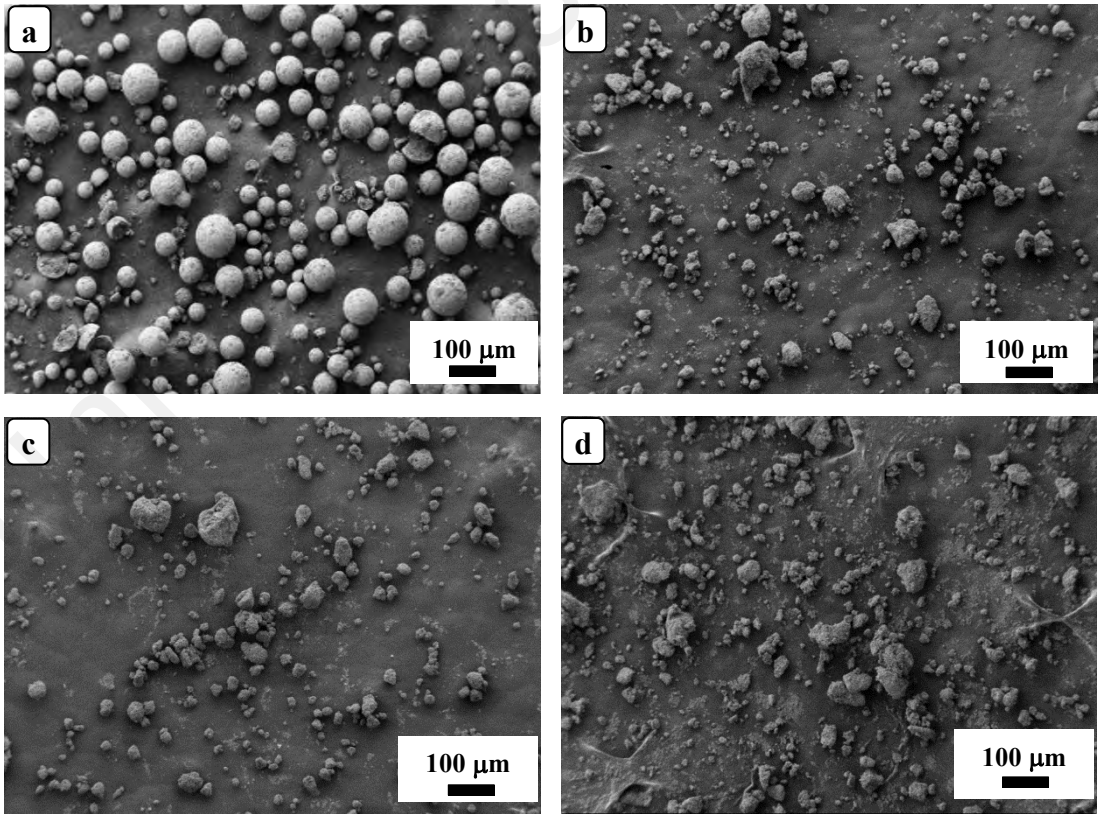

Figure 4.12: FESEM micrographs taken at low magnifications showing agglomerates of the undoped and MnO_2-doped 10Sc1CeSZ powders: (a) undoped, (b) 0.5 wt% MnO_2, (c) 1 wt% MnO_2, (d) 5 wt% MnO_2.

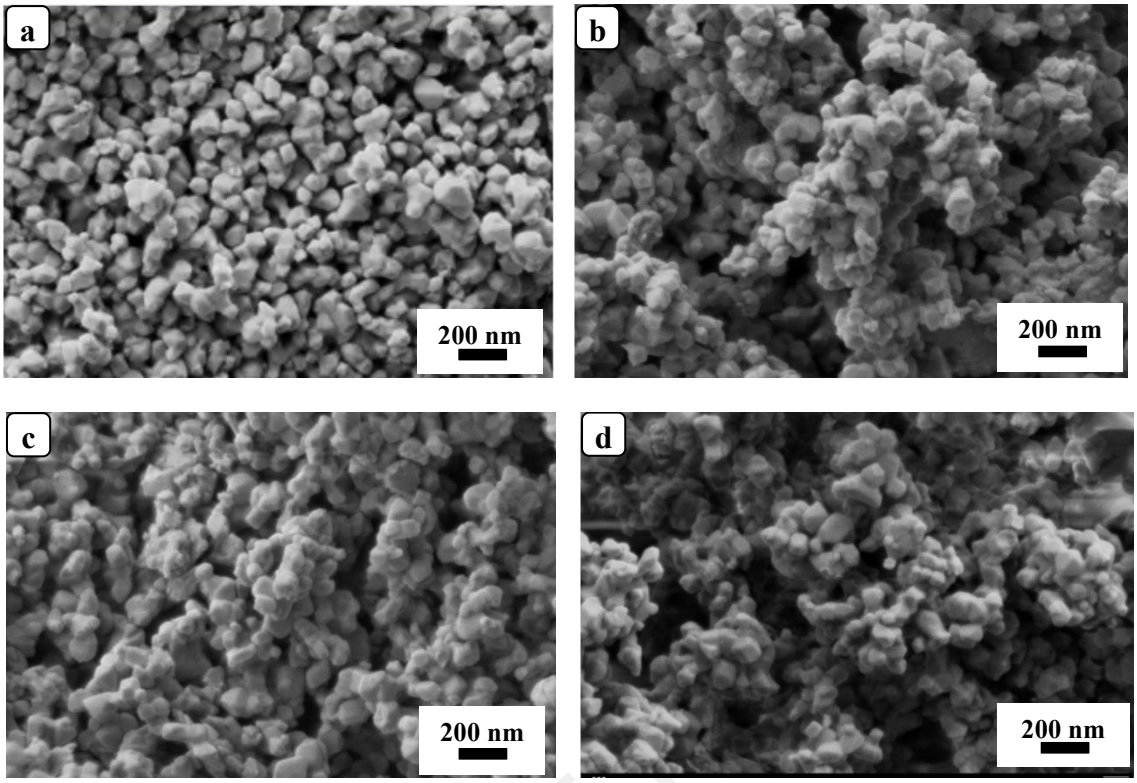

Figure 4.13: Closed up FESEM micrographs showing particle morphologies of the undoped and MnO_2-doped 10Sc1CeSZ powders: (a) undoped, (b) 0.5 wt% MnO_2, (c) 1 wt% MnO_2, (d) 5 wt% MnO_2.

4.3.2: X-Ray Diffraction (XRD) analysis

The XRD plots of undoped and MnO_2-doped 10Sc1CeSZ after sintering at 1400°C to 1550°C for 2 hours are shown in Figure 4.14.

The results indicated that all the XRD signatures for the undoped, 0.5 wt% MnO_2-doped and 1 wt% MnO_2-doped samples conformed to that of cubic zirconia phase (JCPDS file: 01-089-5485). In the case of the 5 wt% MnO_2-doped sample sintered at 1400 °C and 1450 °C, there are three minor secondary XRD peaks observed at $2\theta = 27°$, 35.7° and 53.6°, believed to be that of the tetragonal zirconia phase (JCPDS file: 01-083-1376). However, the tetragonal zirconia phase was not detected for this sample when sintered ≥ 1500°C.

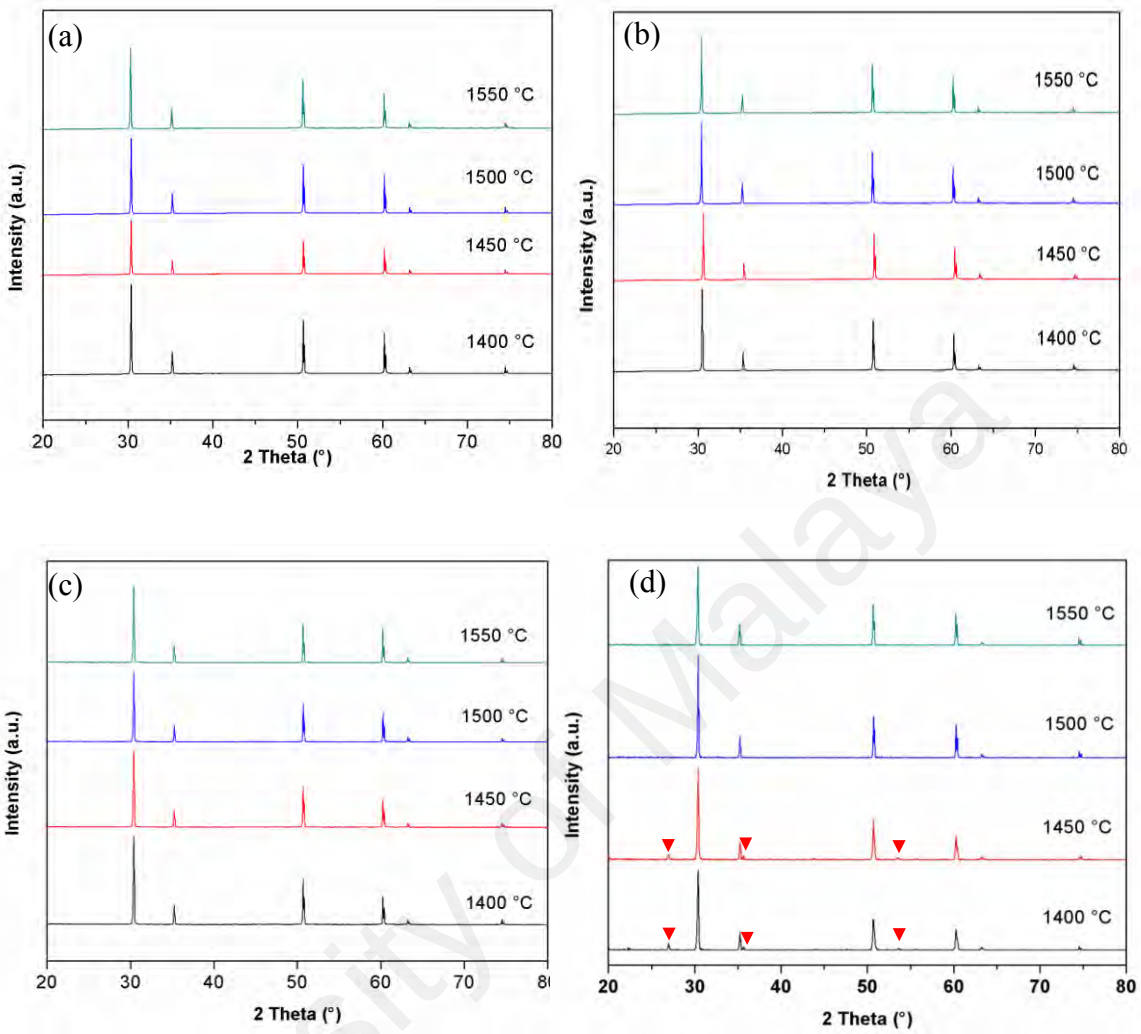

Figure 4.14: The XRD plots of undoped and MnO_2-doped 10Sc1CeSZ sintered samples: (a) undoped, (b) 0.5 wt% MnO_2, (c) 1 wt% MnO_2 and (d) 5 wt% MnO_2 (All the unmarked peaks belong to that of cubic zirconia phase. The marked peaks shown for the 1400°C and 1450°C in (d) belongs to tetragonal peaks.)

It has been reported in the literature (Zhang et al., 2003; Ramesh et al., 2013) that high amount of manganese formed glassy liquid phase at grain boundaries and this could have played a role in destabilizing the cubic phase by drawing out minute amounts of scandia stabilizer from the cubic zirconia grains and hence promoting the formation of the tetragonal phase.

4.3.3: Microstructural evolution

The microstructure evolution of the undoped and MnO_2-doped 10Sc1CeSZ samples sintered at 1400 to 1550°C are shown in Figure 4.15. The grain size calculated based on line intercept method as a function of sintering temperatures is presented in Figure 4.16.

For the undoped samples, the grain size was found to be about 6.7 μm when sintered at 1400-1450°C, and subsequently the grains grew to about 9.9 μm when the sintering temperature increased to 1500-1550°C.

On the other hand, the grain sizes of the 0.5 wt% and 1 wt% MnO_2 additions samples were found to be smaller than the undoped sample i.e. 4.9 μm and 9.0 μm recorded for samples sintered at 1550°C, respectively. In contrast, for the 5 wt% MnO_2-doped sample, the microstructure developed in a similar way to that of the undoped samples up to 1450°C, however as the sintering temperature was increased this was accompanied by a rapid grain growth as shown in Figure 4.16. The average grain sizes measured for this sample were 13.7 μm and 18.6 μm when sintered at 1500°C to 1550°C, respectively.

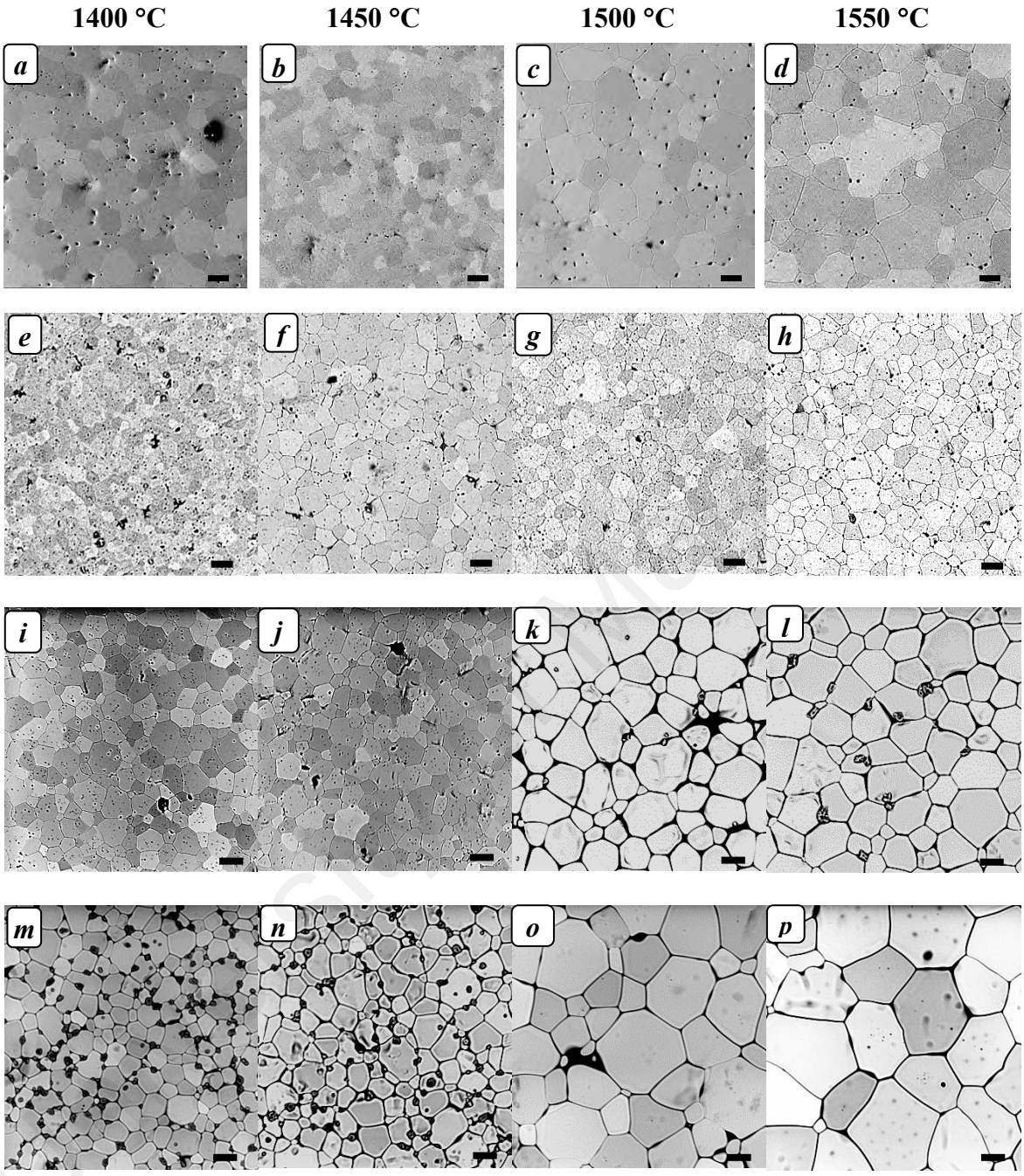

Figure 4.15: Microstructural evolution of 0 wt% MnO_2-doped (a to d), 0.5 wt% MnO_2-doped (e to h), 1 wt% MnO_2-doped (i to *l*) and 5 wt% MnO_2-doped (m to *p*) 10Sc1CeSZ ceramics sintered at various temperatures. The value of the scale bar is 5 µm.

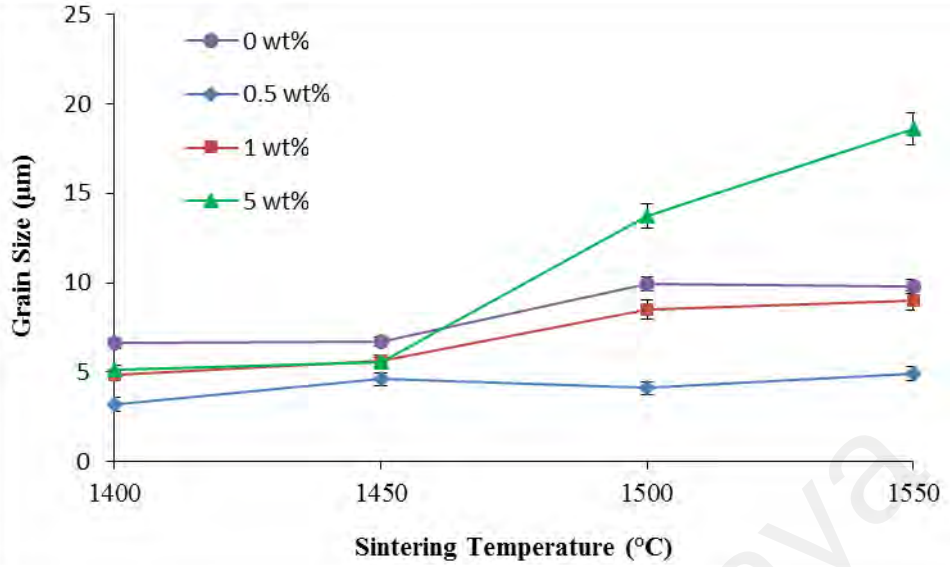

Figure 4.16: The effect of sintering temperatures on the grain size of undoped (0 wt%) and MnO_2-doped 10Sc1CeSZ samples.

The variation of relative density of sintered ceramics with increasing sintering temperatures is shown in Figure 4.17.

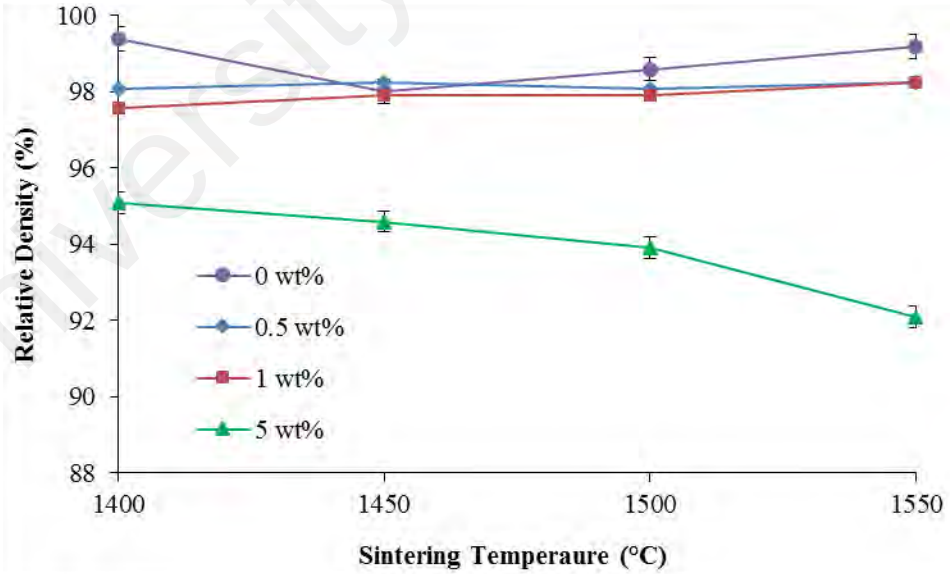

Figure 4.17: The variation of relative density with increasing sintering temperatures for the undoped (0 wt%) and MnO_2-doped 10Sc1CeSZ samples.

The results indicated that the undoped and up to 1 wt% MnO_2-doped samples were able to attain above 97.5% relative density, while the 5 wt% MnO_2-doped zirconia exhibited a lower relative density, about 95%, when sintered at 1400°C, and subsequently declined to 92% when sintered at 1550°C. This observation is in good agreement with the other researchers (Meenaloshini et al., 2008; Ramesh et al., 2008; Ramesh et al., 2011; Khan et al., 2014) who reported that the incorporation of MnO_2 in yttria stabilized zirconia was beneficial in promoting densification at lower sintering temperatures (1250- 1300°C) and may be detrimental to densification when fired at higher sintering temperatures (above 1400°C). On the other hand, the lower relative density exhibited by the 5 wt% MnO_2-doped 10Sc1CeSZ throughout the sintering temperatures experimented could be attributed to the presence of large amount of residual pores located mainly at grain boundary regions, believed to be associated with the melting of large amount of manganese oxide especially at higher sintering temperatures as observed in the SEM micrographs shown in Figure 4.15.

4.3.4: Mechanical properties

The effect of temperatures and dopants on the Vickers hardness, fracture toughness, and elastic modulus of the sintered 10Sc1CeSZ samples are presented in Figure 4.18 to Figure 4.20. The mechanical property trends correlated well with the relative density shown in Figure 4.17.

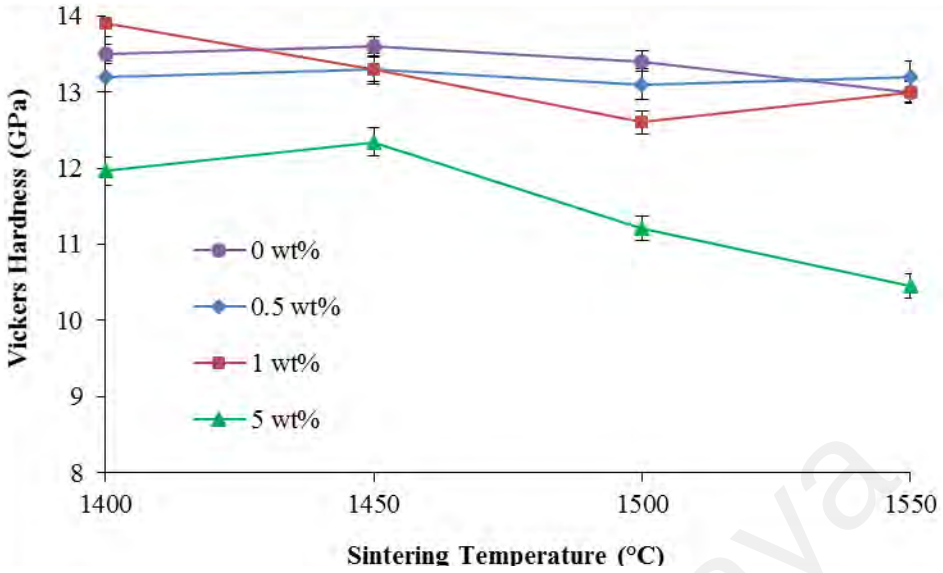

Figure 4.18: The effect of sintering temperatures on the Vickers hardness of undoped (0 wt%) and MnO_2-doped 10Sc1CeSZ samples.

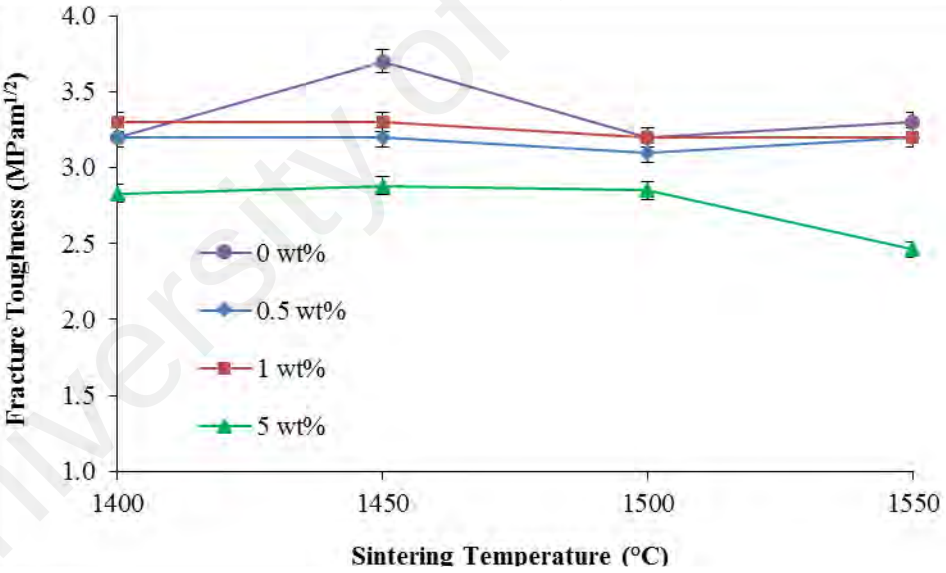

Figure 4.19: The effect of sintering temperatures on the fracture toughness of undoped (0 wt%) and MnO_2-doped 10Sc1CeSZ samples.

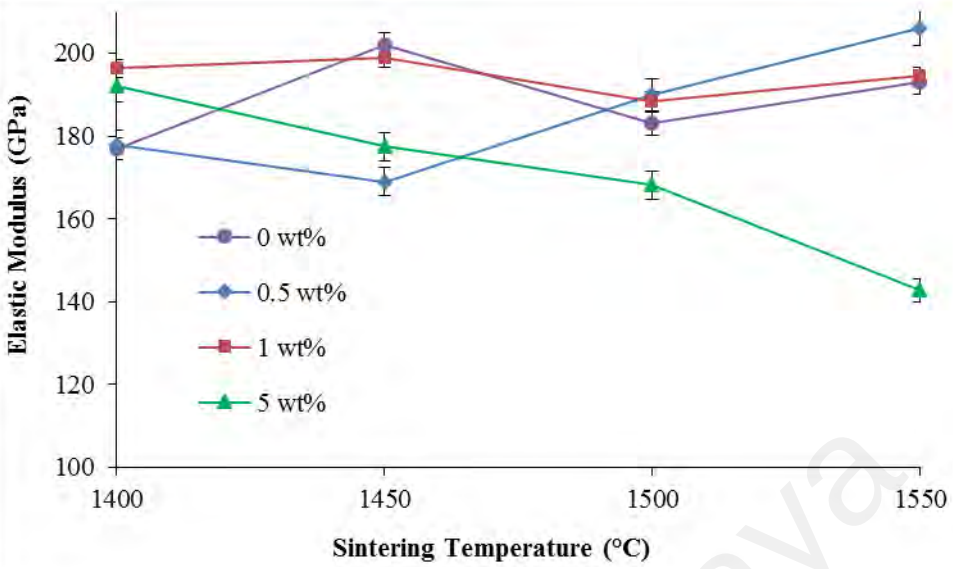

Figure 4.20: The effect of sintering temperatures on the elastic modulus of undoped (0 wt%) and MnO_2-doped 10Sc1CeSZ samples.

It has been found that for undoped and up to 1 wt% MnO_2-doped 10Sc1CeSZ, the Vickers hardness (12.6 – 13.9 GPa) and fracture toughness (~ 3 $MPam^{1/2}$) did not vary significantly with increasing temperatures, while the elastic modulus fluctuated within the range of 169 and 206 GPa. This results showed that the mechanical stability of scandia stabilized zirconia ceramic was not affected by the incorporation of up to 1 wt% of MnO_2, compared to the observation reported by several researchers for up to 1 wt% MnO_2 addition in Y-TZP ceramic (Ramesh et al., 2008; Ramesh et al., 2013; Kwa et al., 2015).

On the other hand, in the case of 5 wt% MnO_2-doped samples, the fracture toughness and Vickers hardness were observed to be lower when compared to the undoped ceramic. The 5 wt% MnO_2-doped zirconia exhibited a low hardness of about 12 GPa when sintered between 1400-1450ºC, before decreasing further with sintering, down to 10.5 GPa when sintered at 1550ºC. The fracture toughness was found to be about 2.8-2.9 $MPam^{1/2}$ when sintered between 1400- 1500ºC, and subsequently decreased to 2.5 $MPam^{1/2}$ at 1550ºC.

Similarly, the elastic modulus of this sample as shown in Figure 4.20 revealed a decreasing trend with increasing sintering temperature and attained a low value of 143 GPa at 1550 ºC. This decline in the mechanical properties is believed to be associated with grain growth when sintered at higher temperatures. Grain coarsening caused an increase in the diffusion distance for matter transport during sintering, thereby reducing the rate of sintering and hence lower densification.

4.3.5: Sintering stages and densification

In this investigation, quenching process was employed to investigate how presence of a liquid phase (if any) or segregation of impurity could affect the grain morphology and grain growth kinetics of 10Sc1CeSZ ceramics doped with varying MnO_2 additions (0, 1, 3, and 5 wt%).

Figure 4.21 shows the low and high magnification FESEM images of the quenched fracture surface of both undoped and MnO_2-doped zirconia ceramic samples, after being heated to 1200 °C with a ramp rate of 10 °C/min. The zirconia compacts were fractured into two pieces after it was rapidly cooled in a bucket of ice cold water.

The fracture surface of the quenched undoped 10Sc1CeSZ sample in Figure 4.21 (1a)- (1b) reveal partial densification had taken place, while the microstructures of MnO_2-doped samples were found to have higher degree of fusion with higher amount of dopant additions. The dissolution of MnO_2 dopant have been found to be beneficial in enhancing the fusion and bonding of zirconia ceramic particles at low sintering temperatures (Ramesh et al., 2011).

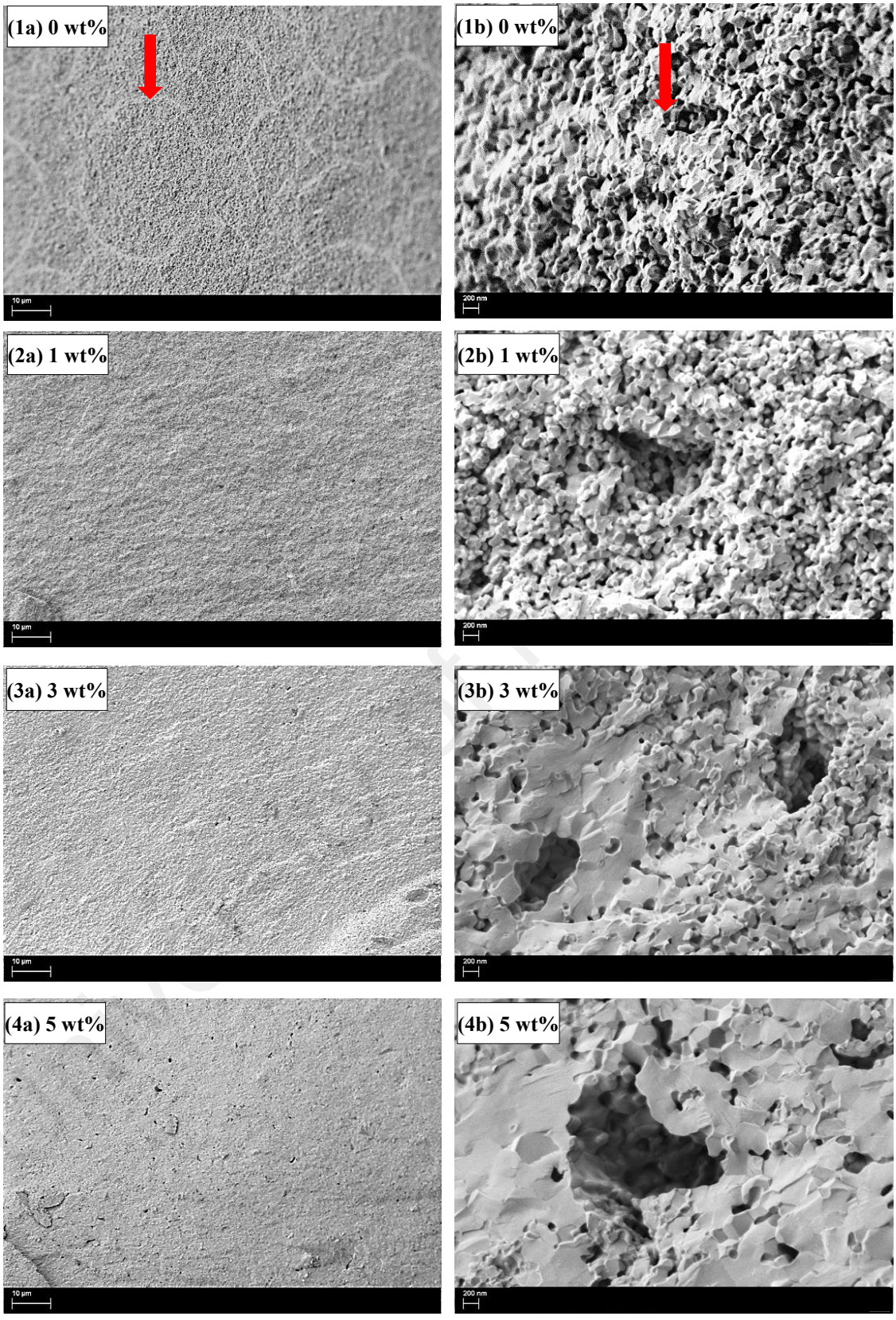

Figure 4.21: FESEM micrographs of undoped and MnO_2-doped 10Sc1CeSZ specimens taken on fracture surfaces at low (a), and high (b) magnifications after quenching at 1200 °C.

An ordered array of continuous ring-shaped lines found on undoped zirconia sample implying local heating at grain boundaries, which can be envisaged as to be responsible for enhanced sintering in both conventional and microwave heating. The particles could be wetted with a liquid phase of minor impurities such as silicon which were segregated to the grain boundaries leading to a faster rate of diffusional transport while restricting grain growth. A small amount of SiO_2 phase is known to accelerate the sintering process by forming a reactive liquid phase and favorably decreases soaking time and temperature of zirconia ceramic processing (De Souza, D. P. F. & De Souza, M. F., 1999; Jong-Heun Lee et al., 2001).

Microstructure observations for 5 wt% MnO_2-doped zirconia samples, as presented in Figure 4.21 (4a) & (4b), show the solidified liquid with large pores, indicating melting and liquid phase sintering has occurred, which led to accelerated grain growth in the final stage of the sintering process. This observation is in agreement with large grain size in the SEM microstructure shown in Figure 4.15 (*m* to *p*). During densification and grain growth, the very large but isolated pores are difficult to remove because of pore agglomerate effect led by grain growth (Francois and Kingery, 1983), which eventually caused a lower final density in 5 wt% MnO_2-doped samples as compared to other lower MnO_2-doped specimens, which is in good agreement with the relative density result depicted in Figure 4.17.

Inclusions containing silicon were detected from the fracture surface of quenched samples in 5 wt% MnO_2-doped sample, as evidenced by the FESEM micrograph and EDS analysis shown in Figure 4.22. The forming of silicon inclusions in yttria-stabilized zirconia was deliberated by Jong-Heun Lee et al. (2000) and was considered as the origin of scavenging. The formation of inclusions with high silicon content suggested that MnO_2 acts as a scavenger in 10Sc1CeSZ ceramics, which reflects that a

considerable amount of siliceous phase was redistributed in an isolated manner, or scavenged by forming a silicon-rich phase such as $ZrSiO_4$, as detected in the XRD plot of 5 wt% MnO_2-doped 10Sc1CeSZ sample in Figure 4.14 (d). This is also in agreement with the observation reported by Chong et al. (2016) on MnO_2-doped 8YSZ.

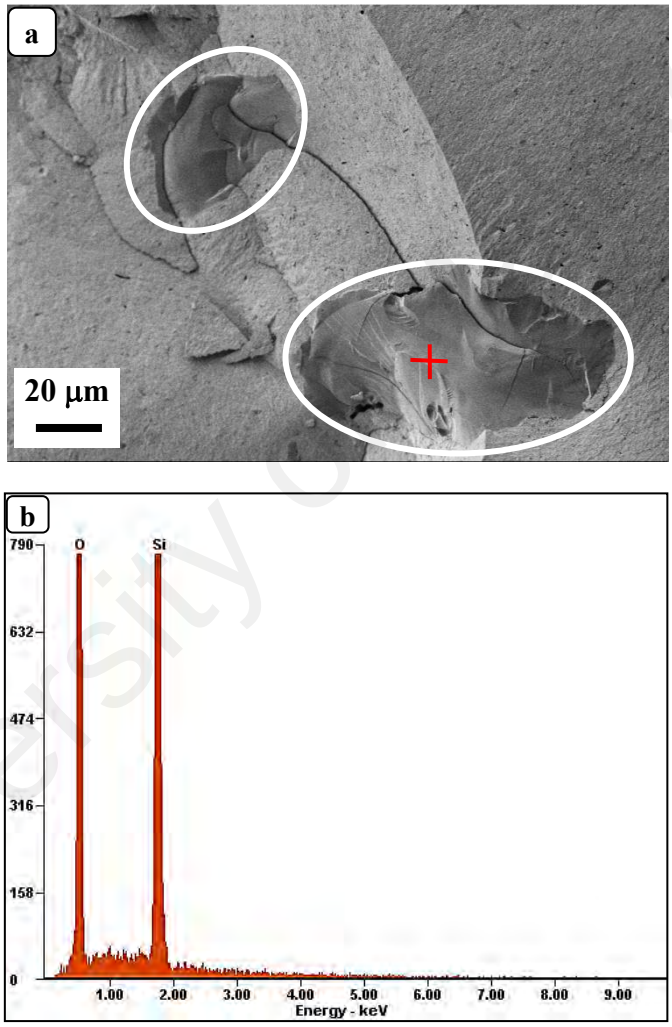

Figure 4.22: (a) FESEM micrograph of fractured surface of 5 wt% MnO_2-doped 10Sc1CeSZ sample after quenching at 1200 °C. The inclusions containing silicon are highlighted in white circles. (b) EDS analysis on the point indicated with a cross marking in (a).

As a conclusion, MnO_2 was found to be an effective additive to scavenge resistive siliceous phase at grain boundaries. A scavenging reaction was suggested to cause the

siliceous phase to be redistributed to an isolated manner to form discrete silicon-containing phase, $ZrSiO_4$. The change in the grain growth kinetics of 10Sc1CeSZ ceramics doped with various ions of different ionic radii and valence has been altered with the build-up of the space charge attributed to the segregation of the aliovalent dopant ions to grain boundaries. Because the Mn^{4+} ion has a null effective charge in the zirconia lattice and has an ionic radius considerably smaller than the Zr^{4+}, a substantial segregation during grain growth could be expected.

4.4: Part 3: Microwave sintering of undoped and MnO_2-doped 10Sc1CeSZ samples

In the previous section, the effect MnO_2 additions on the properties of the 10Sc1CeSZ ceramic was deliberated. This section discusses the effect of microwave sintering on the undoped and MnO_2-doped 10Sc1CeSZ samples and compares with the samples sintered in a conventional furnace under low-temperature regimes. The influence of rapid microwave heating process on the mechanical property and ionic conductivity of the zirconia ceramic was investigated for potential use as electrolyte material in intermediate-temperature SOFC.

4.4.1: Phase analysis

The XRD analysis of the undoped 10Sc1CeSZ samples conventional-sintered and microwave-sintered at 1300- 1350 °C is shown in Figure 4.23. The results revealed the presences of only the cubic phase in the structure. No other secondary phases were detected, thus indicating that both the scandium and cerium has incorporated in the zirconia lattice. This result is in agreement with the findings of several researchers (Zevalkink et al., 2007; Yarmolenko et al., 2009; Grosso & Muccillo, 2013) who

reported only pure cubic phase for samples sintered from 1300 °C and above. It is believed that the incorporation of Sc^{3+} and Ce^{4+} in the zirconia stabilizes the cubic phase and effectively increased the ionic size in the cubic fluorite structure which in turn would create more sites for ionic conduction when the oxygen vacancies are formed within the crystal lattice (Irvine & Connor, 2012).

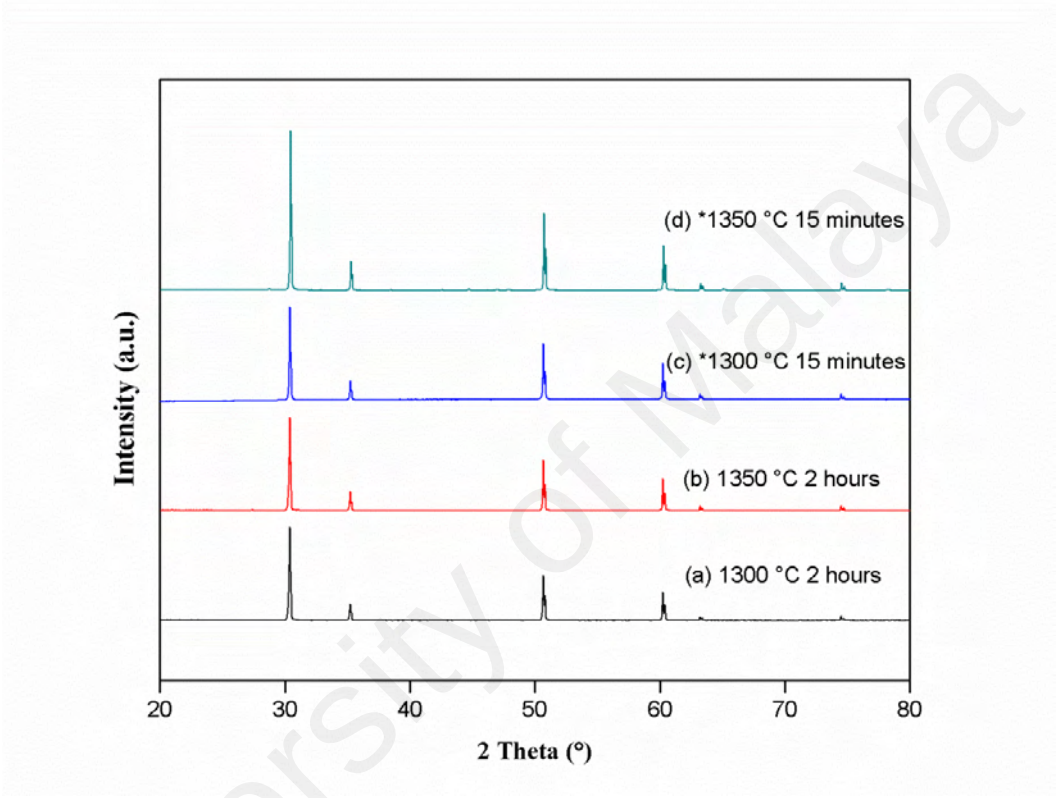

Figure 4.23: The XRD analysis of undoped 10Sc1CeSZ: (a and b) conventional-sintered at 1300- 1350 °C for two hours, and (c and d) microwave- sintered at 1300-1350 °C for 15 minutes.

Figure 4.24 and Figure 4.25 show the XRD plots of samples sintered at 1300 °C and 1350°C using both conventional and microwave sintering techniques, for 0.5 wt% and 1 wt% MnO_2-doped 10Sc1CeSZ samples, respectively. The results indicated that both 0.5 wt% and 1 wt% manganese-doped samples exhibited similar XRD phase contents with undoped samples, and did not vary significantly with different sintering techniques. There are no minor secondary phase signals observed. This result is comparable with the XRD analysis of microwave-sintered undoped 10Sc1CeSZ depicted in Figure 4.23.

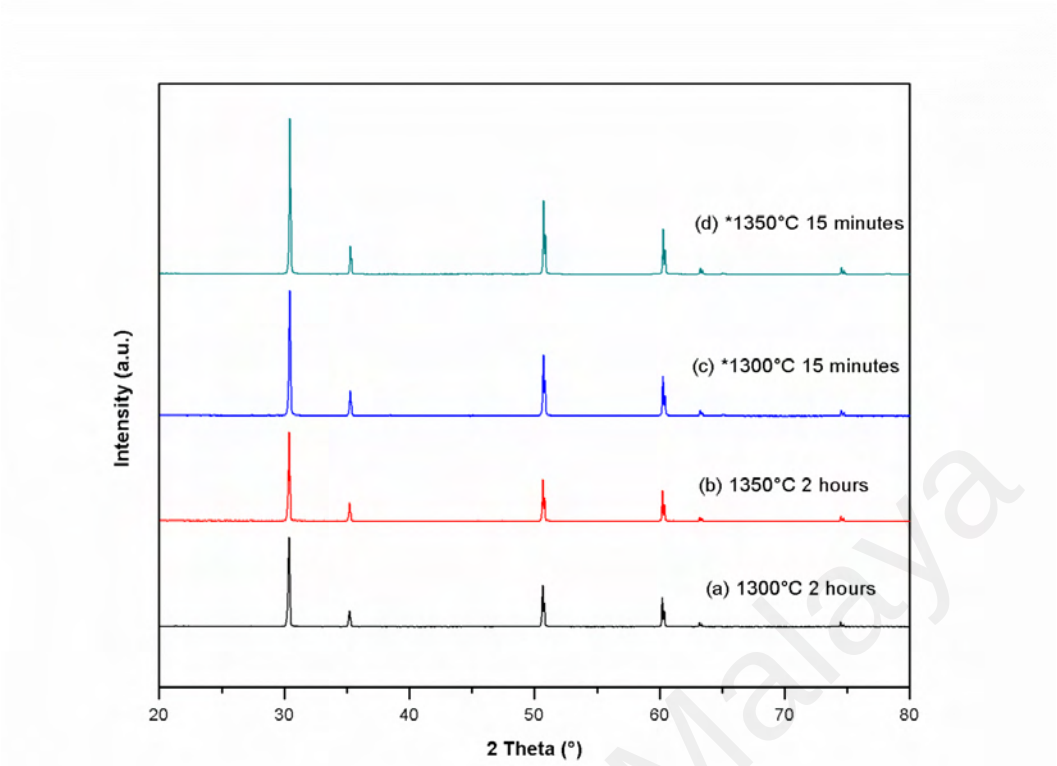

Figure 4.24: The XRD analysis of 0.5 wt% MnO_2-doped 10Sc1CeSZ: (a and b) conventional-sintered at 1300 °C and 1350 °C for two hours, (c and d) microwave sintered at 1300 °C and 1350 °C for 15 minutes.

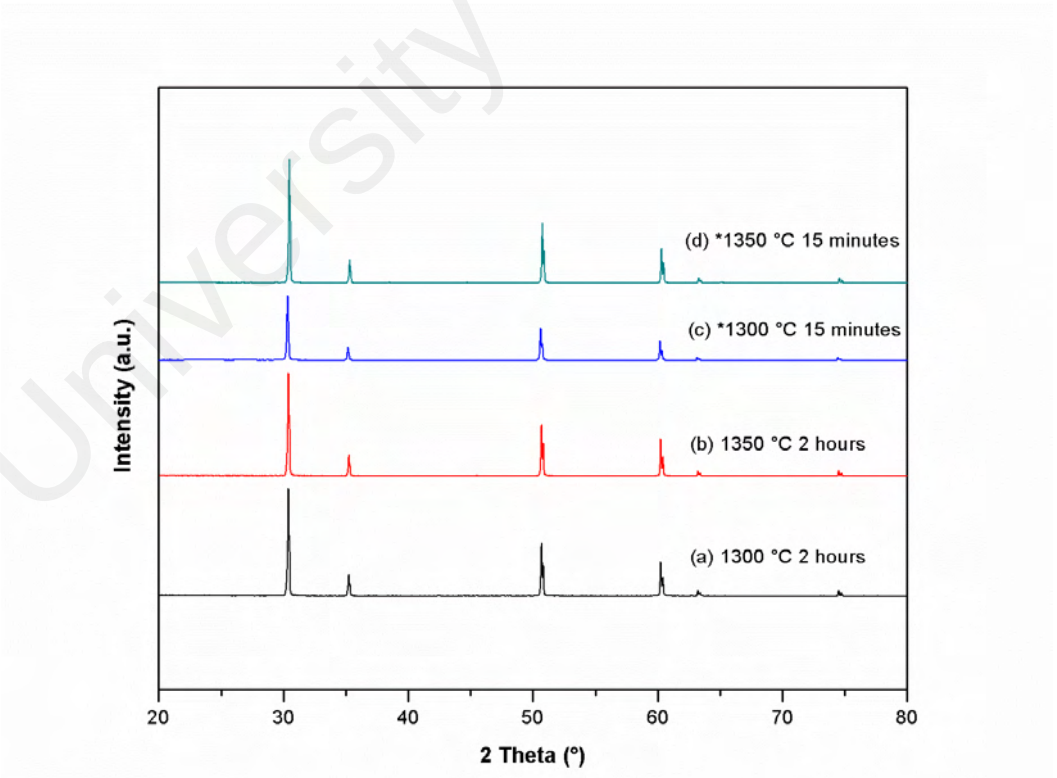

Figure 4.25: The XRD analysis of 1 wt% MnO_2-doped 10Sc1CeSZ: (a and b) conventional-sintered at 1300 °C and 1350 °C for two hours, (c and d) microwave sintered at 1300 °C and 1350 °C for 15 minutes.

4.4.2: Microstructural observation and grain size analysis of undoped 10Sc1CeSZ

SEM micrographs of the undoped 10Sc1CeSZ samples sintered by conventional and microwave methods are shown in Figure 4.26, revealing the presence of equiaxed cubic grains whereas the average grain size of the conventional-sintered samples is shown in Figure 4.27. The results show that the cubic grain size of conventional-sintered zirconia increased with increasing sintering temperature, from 2.9 ± 0.2 μm (1300 °C) to 9.8 ± 0.1 μm (1550 °C). In terms of densification, it was found that all the conventional-sintered samples, regardless of sintering temperatures, exhibited above 97% relative densities as shown in Figure 4.28 (a).

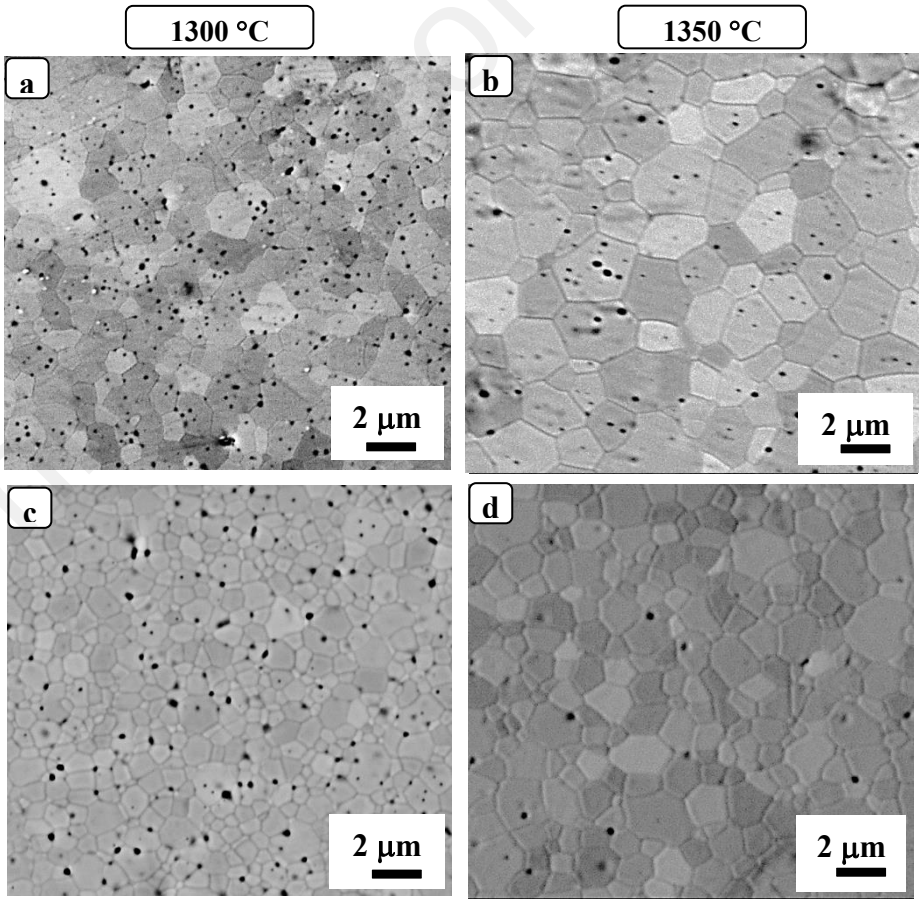

Figure 4.26: Microstructural evolution of undoped 10Sc1CeSZ samples conventional-sintered at (a) 1300 °C, and (b) 1350 °C and microwave-sintered at (c) 1300 °C, and (d) 1350 °C.

The results showed that for every 100 °C increase in sintering temperature, the cubic grain of undoped 10Sc1CeSZ grew at a rate of 3.5 ± 0.2 µm. The grain size obtained in the present work for the conventional-sintered undoped 10Sc1CeSZ sample is slightly higher than the values reported in the literature (Kyrpa, 2013; Yarmolenko et al., 2009). On the other hand, it was found that rapid heating via microwave sintering was effective in suppressing the grain sizes to below 2 µm when sintered at 1300-1350°C and the samples were able to achieve compatible bulk density as with the conventional-sintered undoped 10Sc1CeSZ samples as shown in Table 4.3.

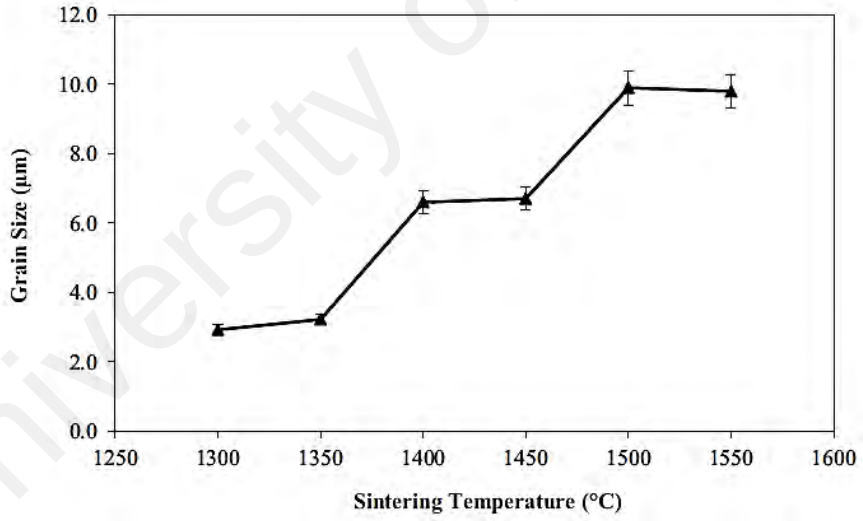

Figure 4.27: The effect of sintering temperatures on the grain size of undoped (0 wt%) 10Sc1CeSZ samples conventional-sintered at 1300-1550 °C.

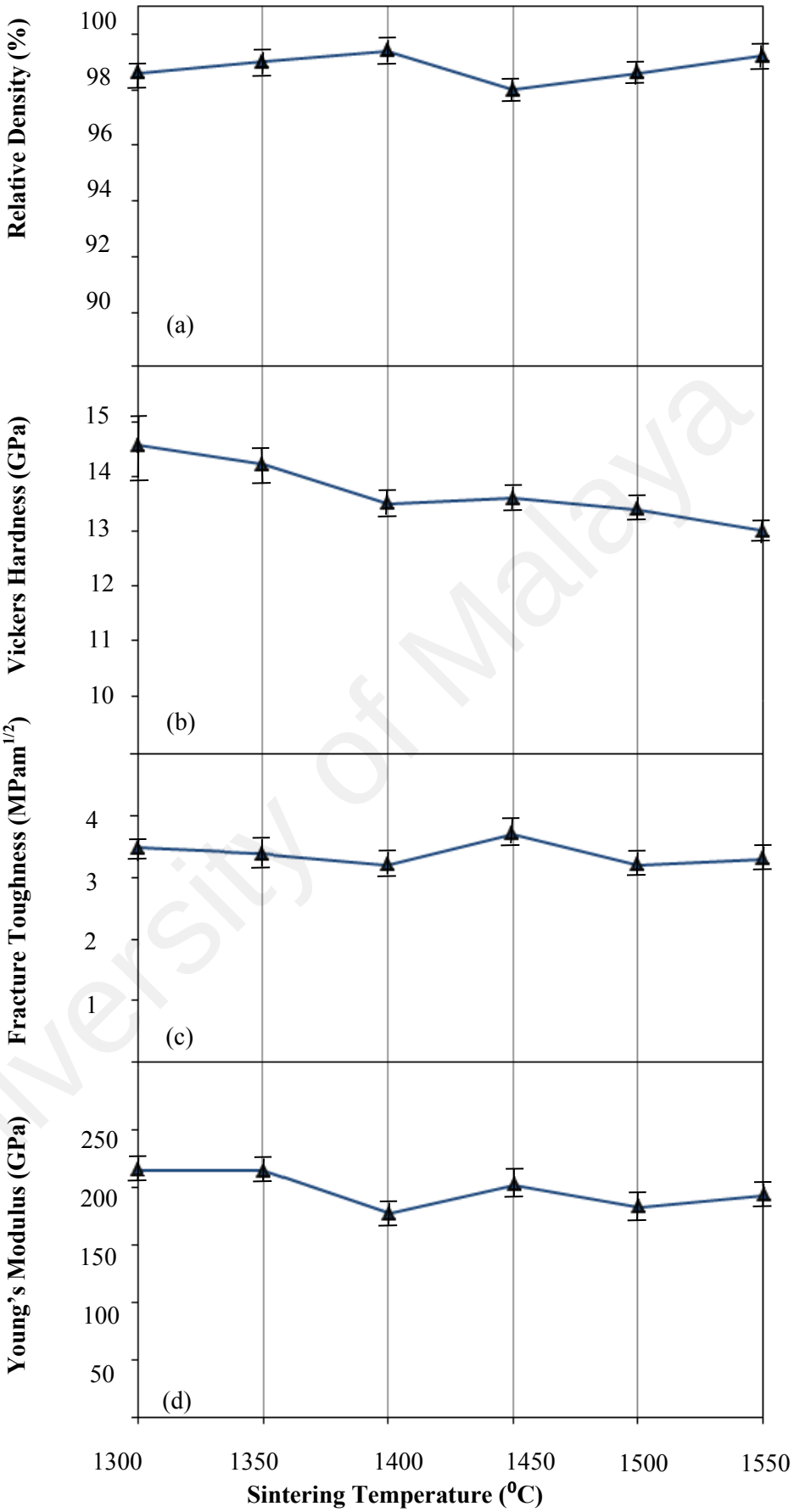

Figure 4.28: The effect of sintering temperatures on the (a) relative density, (b) Vickers hardness, (c) fracture toughness, and (d) Young's modulus of conventional-sintered undoped 10Sc1CeSZ samples.

4.4.3: Microstructural observation and grain size analysis of MnO_2-doped 10Sc1CeSZ

SEM micrographs of the 0.5 and 1 wt% MnO_2-doped 10Sc1CeSZ samples sintered by both conventional and microwave methods are shown in Figure 4.29 and Figure 4.30, respectively. At low sintering regime (1300- 1350 °C), the microstructures of all conventional sintered undoped and MnO_2-doped 10Sc1CeSZ samples were found to be metallographically resembled one another and have an average grain size of 2.4- 4.1 μm, while the microstructures of all microwave sintered samples studied in this work were found to be smaller in size, with an average grain size of less than 2 μm, as shown in Table 4.3- 4.5. This showed that fast firing in the microwave sintering process prevented grain growth from taking place. It is postulated that local dielectric loss at grain boundaries in the microwave can retard grain growth by creating a spatial energy-well that pins the boundary, as proposed by Raj et al. (2011).

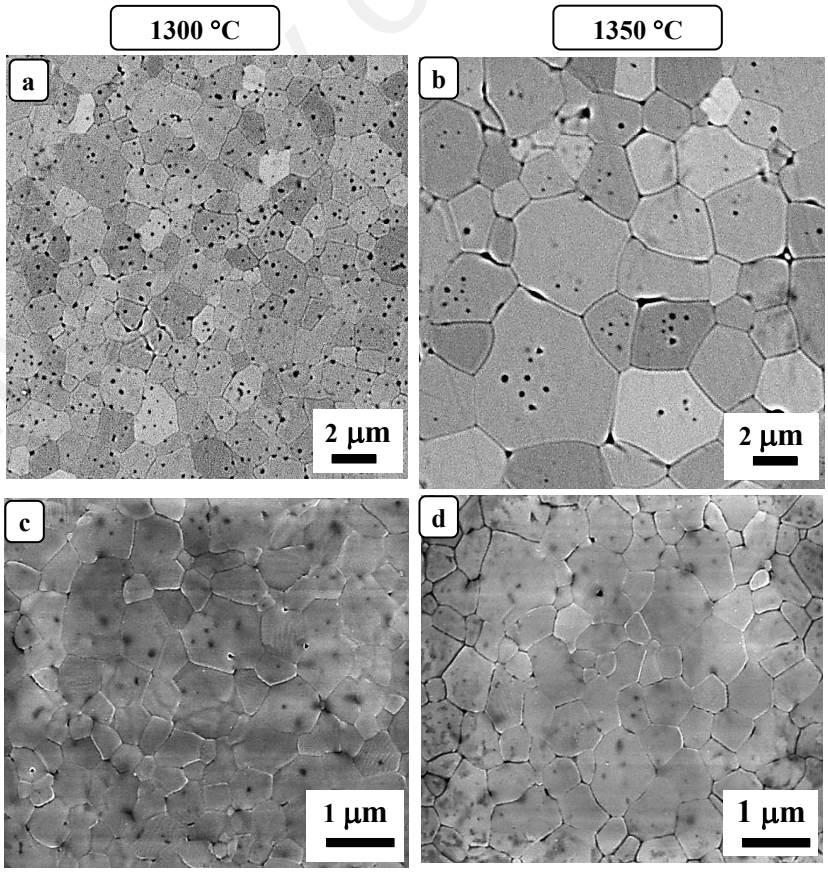

Figure 4.29: Microstructural evolution of 0.5 wt% MnO_2-doped 10Sc1CeSZ samples conventional-sintered at (a) 1300 °C, and (b) 1350 °C and microwave-sintered at (c) 1300 °C, and (d) 1350 °C.

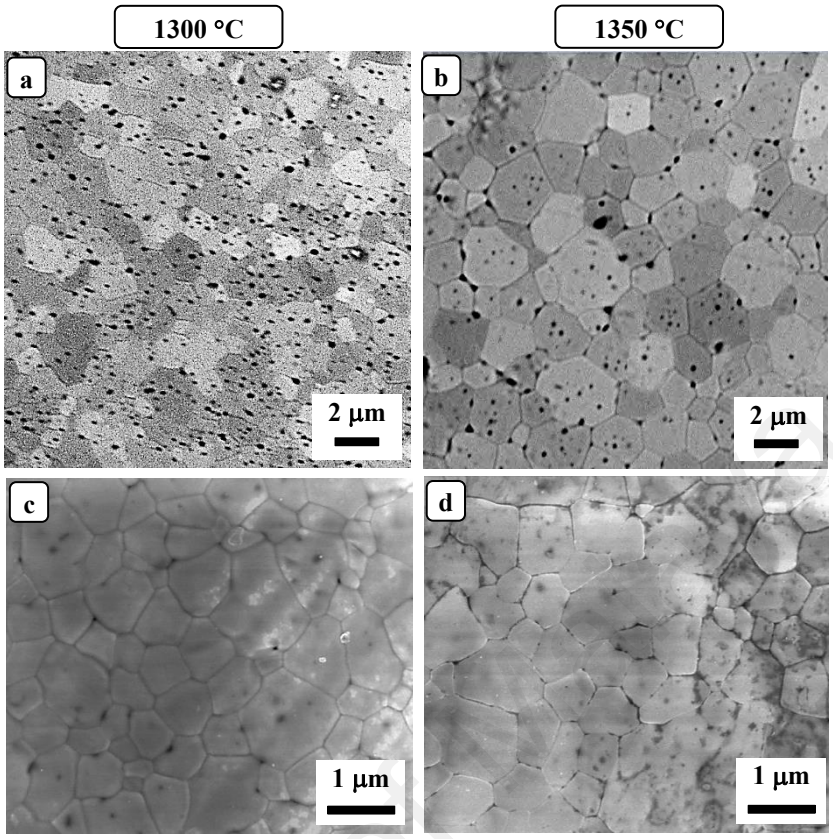

Figure 4.30: Microstructural evolution of 1.0 wt% MnO_2-doped 10Sc1CeSZ samples conventional-sintered at (a) 1300 °C, and (b) 1350 °C and microwave-sintered at (c) 1300 °C, and (d) 1350 °C.

It is also apparent that all the microwave-sintered MnO_2-doped 10Sc1CeSZ samples exhibited a relatively smaller grain size compared to the undoped samples. 0.5 wt% and 1 wt% MnO_2-doped 10Sc1CeSZ samples had an average grain size of 0.8 μm and 1.3 μm, respectively, as compared to 1.8 μm for undoped sample when microwave-sintered at 1350 °C. This is consistent with the results obtained in conventional sintering in which small addition of manganese was found to be able to suppress grain growth.

4.4.4: Mechanical properties of undoped 10Sc1CeSZ

The effect of sintering temperature on the Vickers hardness, fracture toughness, and Young's modulus of the undoped 10Sc1CeSZ samples conventional sintered at 1300 - 1550 °C are presented in Figure 4.28 (b-d). The highest Vickers hardness of 14.6 ± 0.7 GPa was recorded for the 1300 °C conventional-sintered undoped sample. However, as the sintering temperature increased to 1550 °C, this was accompanied by a reduction in the hardness to about 13 GPa ± 0.5 GPa. This trend is in agreement with that reported by Orlovskaya et al. (2010). Higher sintering temperatures produce coarser grains with less grain boundary area per volume and therefore reduce the resistance to localized plastic deformation and results in lower hardness. On the other hand, the microwave sintered samples exhibited comparable hardness, above 13.5 GPa, when sintered at 1300- 1350°C as shown in Table 4.3.

Table 4.3: The properties of microwave-sintered undoped 10Sc1CeSZ

Grain size (µm)	Relative density (%)	Vickers hardness (GPa)	Fracture toughness ($MPam^{1/2}$)	Young's modulus (GPa)
1300 °C /15 min 1.2 ± 0.2	97.5	13.6± 0.4	3.4± 0.2	203.1± 0.5
1350 °C /15 min 1.8 ± 0.1	98.4	14.2± 0.5	3.3± 0.1	198.0± 0.3

The other mechanical properties, i.e. the fracture toughness and Young's modulus of both conventional and microwave sintered samples were found to vary slightly in the range of 3.2- 3.7 $MPa.m^{1/2}$ and 180- 215 GPa, respectively with increasing temperatures as shown in Figure 4.28 and Table 4.3.

These results indicated that fracture toughness and Young's modulus of the ceramic was not affected by the increase in the grain size with increasing sintering temperature. This observation is in contrast to that normally observed for tetragonal zirconia where depletion of the stabilizer (for example, yttria in the case of 3 mol% Y-TZP) would proceed at higher sintering temperatures associated with grain coarsening which in turn promoted transformation toughening to proceed thus enhancing the mechanical properties. In the present work for a fully cubic zirconia, stabilizer depletion could not have taken place under the current sintering profile due to the higher amount of stabilizer present (i.e. 10 mol% scandia). This in turn resulted in a stable cubic grain structure which will not be responsive to transformation toughening. As a result, it is expected that there will not be much changes in the fracture toughness and Young's modulus with increasing grain size or sintering temperature.

4.4.5: Mechanical Properties of MnO_2-doped 10Sc1CeSZ

Table 4.4- 4.5 summarize the properties of conventional-sintered and microwave-sintered MnO_2-doped 10Sc1CeSZ samples at low sintering regimes (1300- 1350 °C), respectively.

Table 4.4: **Properties of 0.5 and 1.0 wt% MnO_2-doped 10Sc1CeSZ samples conventional-sintered at 1300 °C and 1350 °C.**

MnO_2 addition (wt%)	Grain size (µm)	Relative density (%)	Vickers hardness (GPa)	Fracture toughness ($MPam^{1/2}$)	Young's modulus (GPa)
1300 °C /2 hours					
0.5	2.4 ± 0.2	97.9	14.0± 0.3	3.4± 0.1	195.2± 0.5
1.0	3.0 ± 0.3	97.6	14.0± 0.4	3.5± 0.2	200.4± 0.3
1350 °C / 2 hours					
0.5	3.0 ± 0.2	97.7	14.7± 0.4	3.8± 0.2	202.0± 0.4
1.0	4.1 ± 0.1	98.3	14.0± 0.2	3.5± 0.1	205.6± 0.6

Table 4.5: Properties of 0.5 and 1.0 wt% MnO_2-doped 10Sc1CeSZ samples microwave-sintered at 1300 °C and 1350 °C.

MnO_2 addition (wt%)	Grain size (μm)	Relative density (%)	Vickers hardness (GPa)	Fracture toughness ($MPam^{1/2}$)	Young's modulus (GPa)
1300 °C /15 min					
0.5	0.9 ± 0.2	91.3	9.9 ± 0.4	3.1± 0.1	172.5 ± 0.4
1.0	1.1 ± 0.3	92.9	11.6± 0.5	3.1± 0.1	-
1350 °C / 15 min					
0.5	0.8 ± 0.3	92.9	11.3± 0.4	3.1± 0.1	-
1.0	1.3 ± 0.2	94.8	12.4± 0.2	3.2± 0.1	-

There was no significant difference observed between the relative densities of the undoped and MnO_2-doped 10Sc1CeSZ samples under conventional sintering process, whereas the relative densities of MnO_2-doped 10Sc1CeSZ samples were found to be lower than the undoped samples under microwave sintering process. The results show that minor MnO_2 doping appeared to have significant negative influence on the microwave sintering process at low sintering temperature. However, the relative density of the microwave-sintered MnO_2-doped zirconia ceramics were found to increase when the sintering temperature was raised from 1300 °C to 1350 °C; 0.5 wt% MnO_2 addition achieved ~93% relative density while 1 wt% MnO_2 addition obtained a denser structure, ~95 % relative density, when sintered at 1350 °C.

A similar trend is seen with the mechanical properties of the MnO_2-doped zirconia samples. The Vickers hardness of 0.5 wt% and 1 wt% MnO_2-doped zirconia increased to 11.3 GPa (increased by 14%) and 12.4 GPa (increased by 7%), respectively, when the microwave sintering temperature was increased from 1300 °C to 1350 °C. Fracture

toughness of MnO_2-doped zirconia ceramics remains as ~3.1-3.8 $MPam^{1/2}$, regardless of sintering temperatures and sintering techniques.

It is believed that the doping could have influenced the grain boundary kinetics. This could be due to differential densification during rapid microwave sintering of MnO_2-doped 10Sc1CeSZ compacts that lead to the enlargement of the voids or even the generation of crack-like voids in the less dense regions, thus lowering the mechanical properties of the sintered compacts. This is evidenced in the other mechanical properties such as Young's modulus observed in the results shown in Table 4.5. Some obvious crack lines were developed during the fast firing of microwave sintering process that caused the Young's modulus value to drop significantly in microwave-sintered MnO_2-doped samples. Young's modulus was not measured from some MnO_2-doped bar samples due to severe cracks during microwave sintering process. Slender bar samples developed crack lines under inhomogeneous deformation due to differential thermal expansion.

4.4.6: Electrical property evaluation of undoped 10Sc1CeSZ

The Nyquist plots from the impedance data collected over the operating temperature range of 600 °C- 800 °C for the undoped 10Sc1CeSZ samples sintered at 1300 °C and 1350 °C using both conventional and microwave methods are shown in Figure 4.31. The equivalent circuit with parallel resistance-constant phase element (RQ) was used to fit the depressed arcs observed in the impedance spectra.

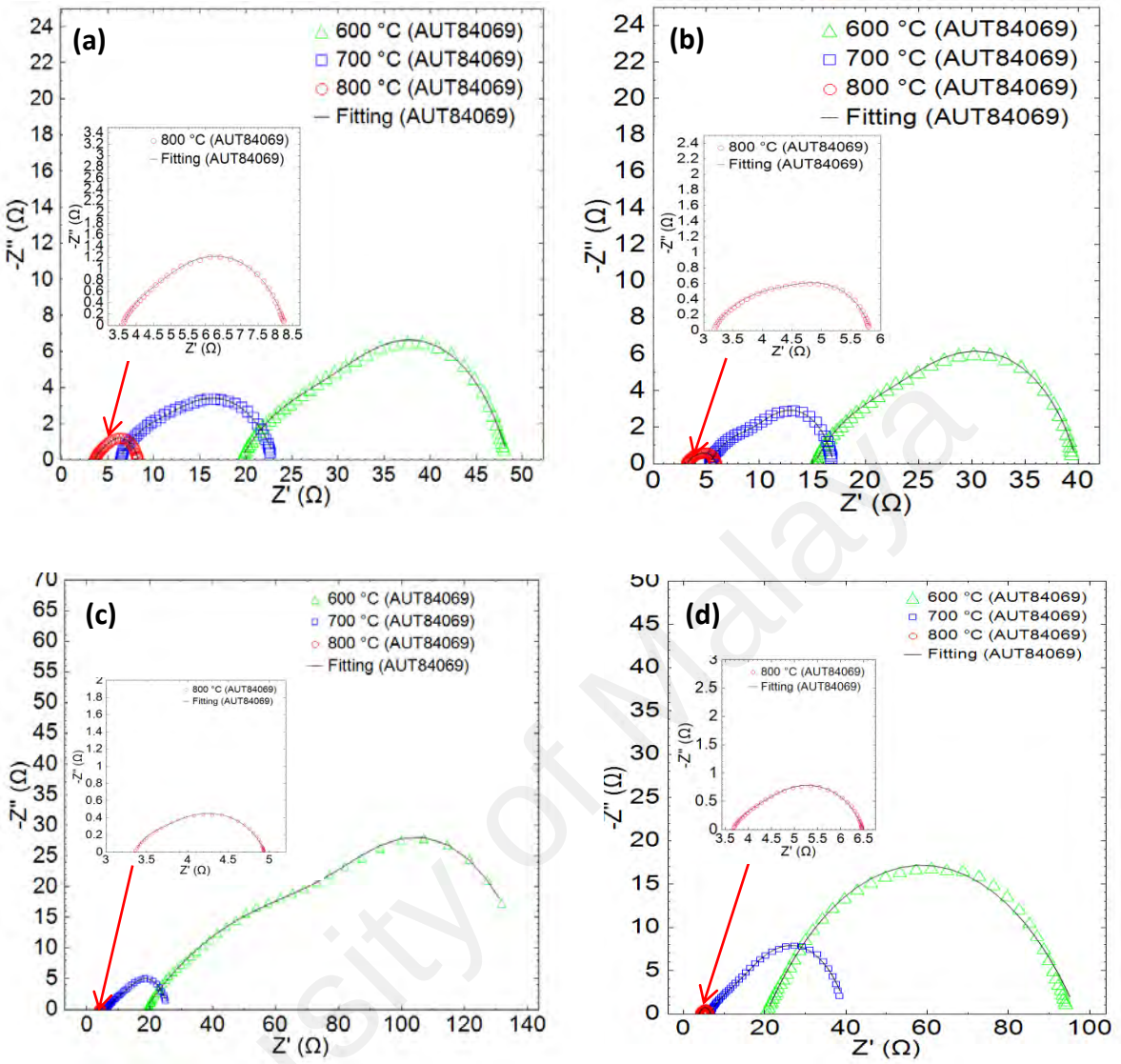

Figure 4.31: Nyquist plots taken at varying temperatures for undoped 10Sc1CeSZ samples conventional-sintered at: (a) 1300°C, (b) 1350°C and microwave-sintered at: (c) 1300°C, (d) 1350°C.

It is visible from the high frequency intercepts, the impedance of the bulk component of all samples tested become smaller with rising operating temperatures. This is postulated as the association energy becomes less significant due to dissociation of oxygen vacancies (O^{2-}) from the cations at higher temperatures, and consequently activation energy for the ionic conduction is predominantly by virtue of oxygen ion migration enthalpy (Irvine & Connor, 2012). Migration energy needed for the free ions

to hop from one crystal site to its next unoccupied lattice site would be readily available from the elevated temperature operations; hence lower activation energy and higher ionic conduction occur with raising temperatures.

Both scandia and zirconia have a ratio of ionic radius of the cation (r_c) and anion (r_a), i.e. r_c/r_a of less than 0.7, thus favored in sixfold coordination in the crystal structure. Lower coordination number elicits the formation of strong anion microdomains eventuated in higher activation energy at lower temperatures, caused by additional ordering energy due to presence of the microdomains of correlated dopant-vacancy clusters (Politova & Irvine, 2004; Preis et al., 2011).

Figure 4.32 shows the temperature dependence electrical conductivities of ceria doped scandia stabilized zirconia, based on the Arrhenius equation. The sample conventional-sintered at 1550 °C and the microwave-sintered at 1350 °C recorded high total ionic conductivity of 0.280 S/cm and 0.314 S/cm when tested at 800 °C, respectively. This is higher compared to the YSZ, the state-of-the-art ceramic electrolyte material used in SOFCs, which exhibited ionic conductivity of 0.164 Scm^{-1} and 0.03 Scm^{-1} at 1000 °C and 800 °C, respectively (Revankar & Majumdar, 2014). Grain boundary impedance which is related to the oxygen vacancy movement through the grain boundaries in the crystals was found to diminish at higher operating temperatures, especially at above 700 °C. This observation is in agreement with that reported by Shi et al. (2012).

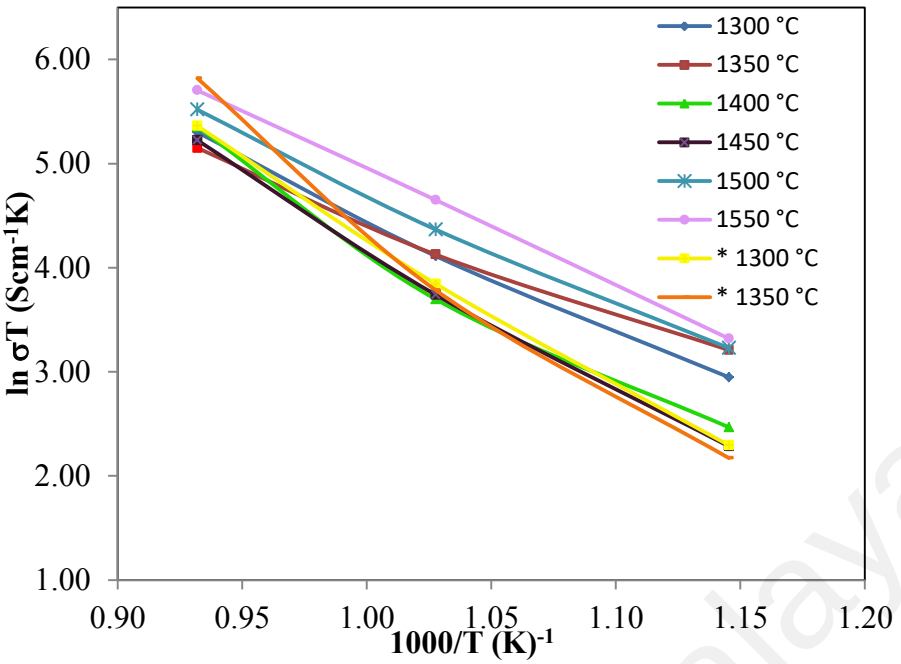

Figure 4.32: Arrhenius plots of the total conductivity of undoped 10Sc1CeSZ as a function of sintering temperatures. The graphs for microwave-sintered samples are represented by *1300 °C and *1350 °C.

Table 4.6 shows the block factor as a function of temperatures for conventional and microwave sintered samples. Fine grained microwave-sintered samples with larger grain boundary area showed larger blocking factors compared to conventional-sintered samples when measured at 600-700 °C, which has led to lower ionic conductivity in microwave-sintered samples, indicating an increased surface free energy change due to larger grain boundary area.

Table 4.6: Block factor (α_R) measured at 600 °C, 700 °C, and 800 °C for undoped 10Sc1CeSZ samples sintered at 1300 °C and 1350 °C through conventional (Conv) and microwave (MW) methods.

Sample	$\alpha_{600°C}$	$\alpha_{700°C}$	$\alpha_{800°C}$
Conv- 1300 °C	0.43	0.46	0.27
Conv- 1350 °C	0.41	0.52	0.34
MW- 1300 °C	0.84	0.60	0.26
MW- 1350 °C	0.79	0.63	0.16

For the microwave sintered samples, a significant improvement in ionic conductivity was observed when the operating temperature was increased to 800 °C. The diminishing blocking effect at grain boundaries implied that the high ionic resistivity of space charge layers adjacent to grain boundaries could be altered with high kinetic mass transport process at high operating temperature. It is postulated that thermally activated creep in fine-grained microwave sintered 10Sc1CeSZ samples occurred at 800°C that can greatly enhance the diffusional transport across the grain boundary and overcome the activation barrier for the mobility of charged particles.

4.4.7: Electrical property evaluation of MnO_2-doped 10Sc1CeSZ

In Figure 4.33- 4.34, a collection of Nyquist plots of 0.5 wt% and 1 wt% MnO_2-doped 10Sc1CeSZ samples recorded over the measuring temperature range of 600-800°C is shown. The impedance spectrums were fitted with the equivalent circuits using parallel resistance-constant phase element (R-Q) in series for the depressed arcs with non-ideal capacitive property. R_{bulk} is the bulk resistance obtained from the high frequency intercepts on the real axis, while the intermediate frequency impedance arc is attributed to the grain-boundary resistance, R_{GB}.

There are no appreciable differences in the bulk and grain boundary resistance observed for both 0.5 wt% and 1 wt% MnO_2-doped zirconia samples sintered using conventional and microwave sintering. The impedance terminates in a large resistance with a low frequency electrode spike for all samples signifying charge build-up at the blocking silver electrode, except for the conventional-sintered samples that showed a slightly larger semicircular plot at high frequency region when measured at 600 °C. The latter indicates that the electrochemical system is kinetically sluggish with significantly

large charge transfer resistance and relatively small mass transfer feature at low operating temperature.

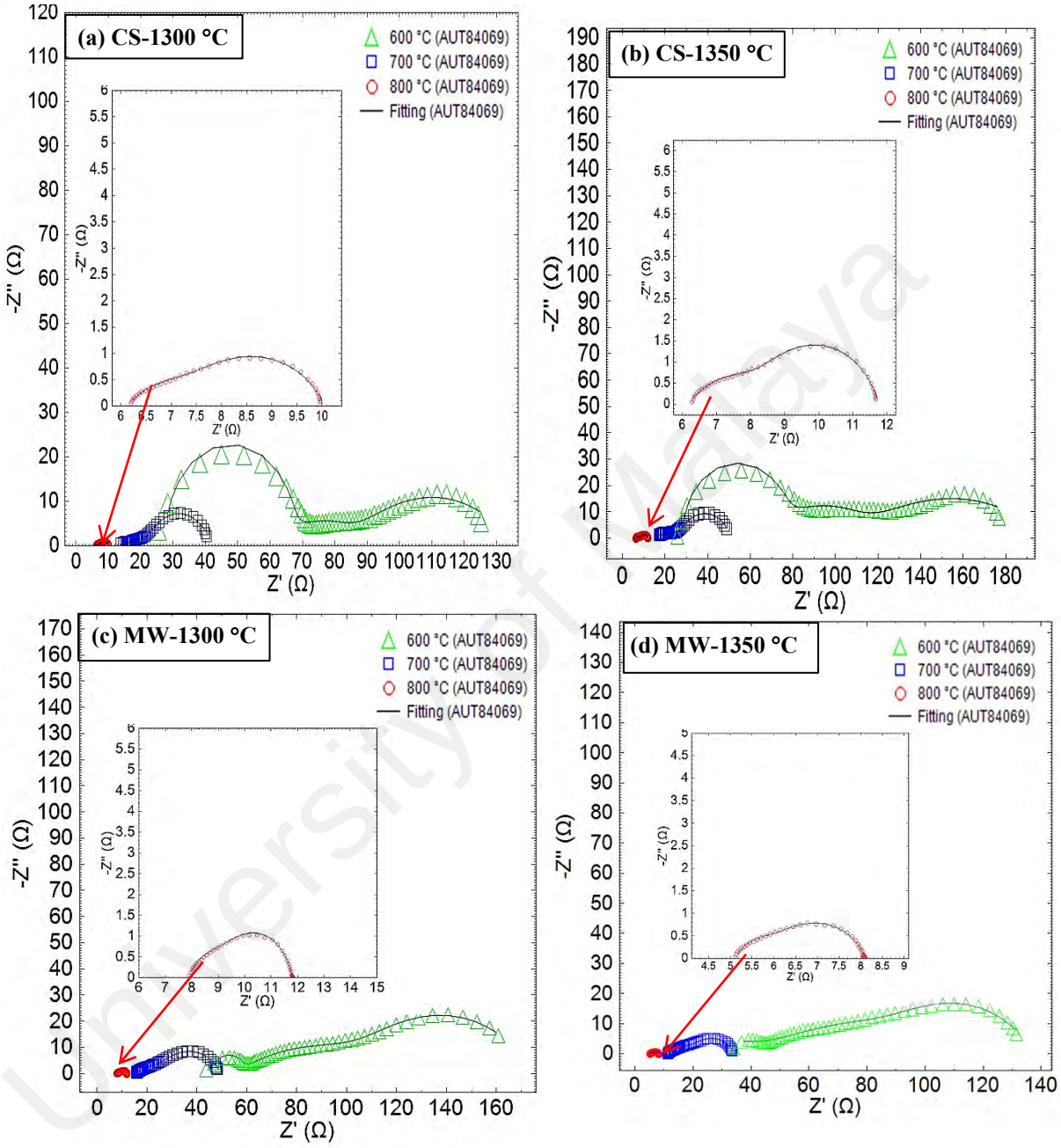

Figure 4.33: Nyquist plots for 0.5 wt% MnO_2-doped 10Sc1CeSZ samples conventional-sintered at (a) 1300 °C, (b) 1350 °C and microwave-sintered at (c) 1300 °C, (d) 1350 °C. The graphs for conventional and microwave-sintered samples are represented by CS and MW, respectively.

Higher capacitive effect observed is ascribed to space charge layer. A space-charge layer is believed to form due to enrichment of dopant cation on the grain boundary surface that causes a depletion of oxygen vacancies (Abdala et al, 2010). Grain

boundary segregation of impurities or dopants is well known to cause a decrease in the total free energy of the system, stem from the compensation of space charges by aliovalent dopants, reduction of strain energy, and lowering of surface tension (Verkerk et al., 1982).

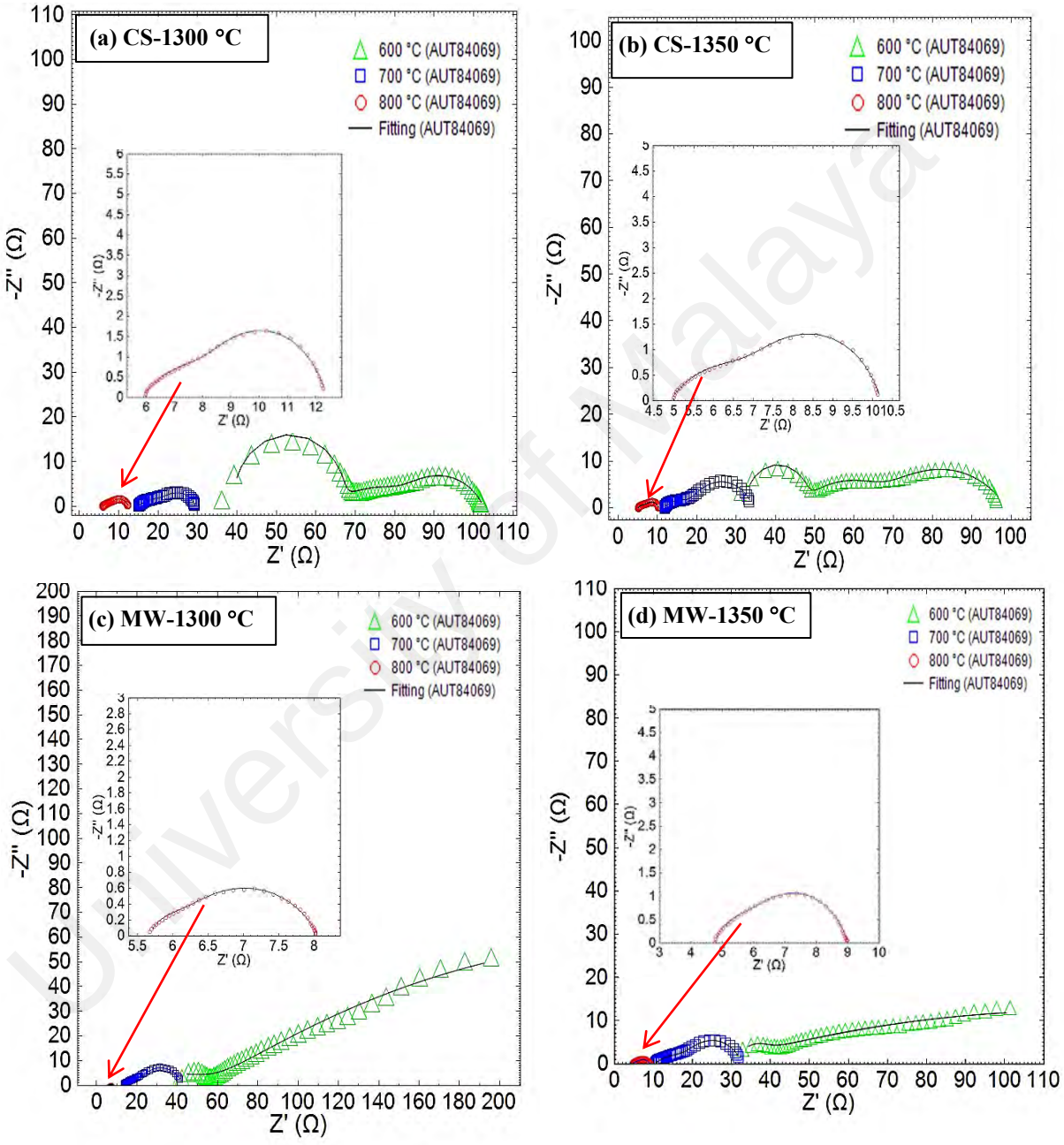

Figure 4.34: **Nyquist plots for 1.0 wt% MnO_2-doped 10Sc1CeSZ samples conventional-sintered at (a) 1300 °C, (b) 1350 °C and microwave-sintered at (c) 1300 °C, (d) 1350 °C. The graphs for conventional and microwave-sintered samples are represented by CS and MW, respectively.**

Figure 4.35- 4.36 shows the Arrhenius plots of MnO_2-doped 10Sc1CeSZ samples sintered at 1300 °C and 1350 °C, respectively, by conventional and microwave sintering. The conductivity of all conventional-sintered and microwave-sintered MnO_2-doped zirconia samples were found to be low at 600 °C, attributed to low mobile oxide ions caused by dopant –defect interaction.

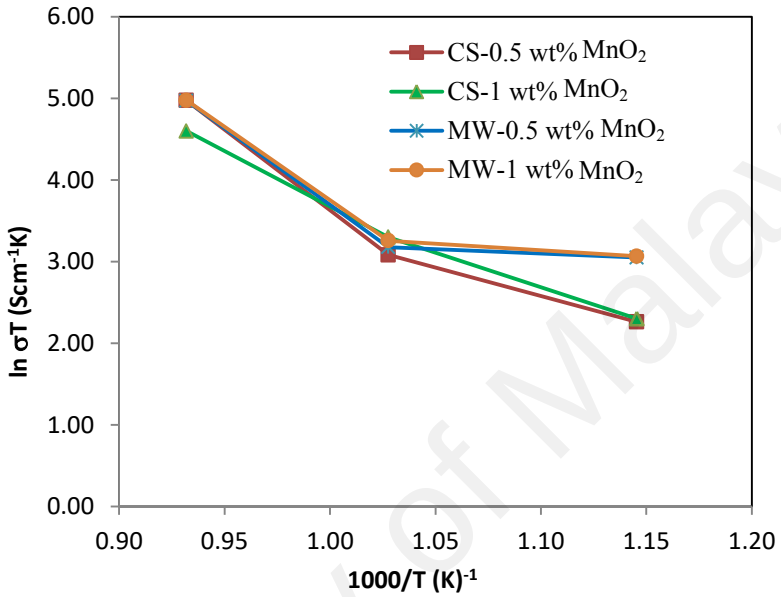

Figure 4.35: Arrhenius plots of the total conductivity of MnO_2-doped 10Sc1CeSZ (sintered at 1300 °C) as a function of sintering temperatures. The graphs for conventional and microwave-sintered samples are represented by CS and MW, respectively.

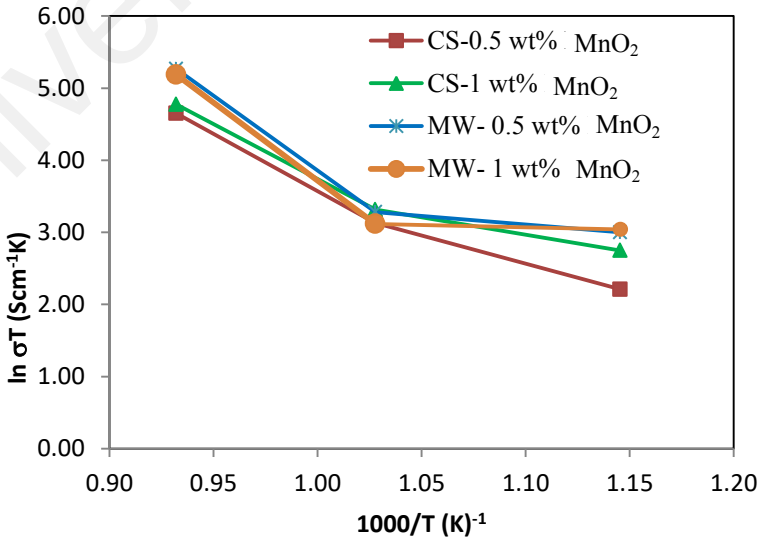

Figure 4.36: Arrhenius plots of the total conductivity of MnO_2-doped 10Sc1CeSZ (sintered at 1350 °C) as a function of sintering temperatures. The graphs for conventional and microwave-sintered samples are represented by CS and MW, respectively.

At 700 °C, as the bulk resistivity decreased due to weaker dopant-vacancy association with increasing operating temperature, a slight improvement on total ionic conductivity exhibited. The effect of spatial inhomogeneous resistivity, which can be explained by different composition of grain boundaries comparing to bulk by the segregation of the dopant or impurity, such as silicon, could cause the formation of new phase in grain boundaries that would affect the transport kinetics of oxygen vacancy in zirconia.

When the operating temperature was increased further, ions have greater thermal energy and able to vibrate more rigorously; also, defect concentrations became higher, a high conductivity of 0.14- 0.18 S/cm was recorded for the microwave-sintered MnO_2-doped zirconia samples when measured at 800 °C, attributed to higher diffusivity for mass transport that reflects the characteristics of the enhanced transport.

Table 4.7-4.8 shows the blocking factor for conventional and microwave-sintered MnO_2-doped 10Sc1CeSZ samples.

Table 4.7: Block factor (α_R) measured at 600 °C, 700 °C, and 800 °C for 0.5 wt% & 1.0 wt% MnO_2-doped 10Sc1CeSZ samples conventional-sintered at 1300 °C and 1350 °C.

MnO_2-doped Sample	**$\alpha_{600°C}$**	**$\alpha_{700°C}$**	**$\alpha_{800°C}$**
0.5 wt%- 1300 °C	0.57	0.32	0.33
0.5 wt%- 1350 °C	0.61	0.51	0.30
1.0 wt%- 1300 °C	0.40	0.32	0.33
1.0 wt%- 1350 °C	0.31	0.41	0.33

Table 4.8: Block factor (α_R) measured at 600 °C, 700 °C, and 800 °C for 0.5 wt% & 1.0 wt% MnO_2-doped 10Sc1CeSZ samples microwave-sintered at 1300 °C and 1350 °C.

MnO_2-doped Sample	$\alpha_{600°C}$	$\alpha_{700°C}$	$\alpha_{800°C}$
0.5 wt%- 1300 °C	0.17	0.47	0.17
0.5 wt%- 1350 °C	0.14	0.53	0.17
1.0 wt%- 1300 °C	0.17	0.49	0.14
1.0 wt%- 1350 °C	0.25	0.53	0.21

The results show that conventional-sintered MnO_2-doped 10Sc1CeSZ exhibited higher grain boundary resistivity at 600 °C, and the blocking effect decreased with increasing measuring temperatures. On the other hand, the microwave-sintered MnO_2-doped samples were dominated by bulk resistance when measured at 600 °C, which is in contrast to the high grain boundary effect exhibited by undoped samples produced under the same microwave sintering conditions. However, this is in good agreement with the mechanical properties presented in Table 4.5, which exhibits inhibited sintering kinetics with low relative density (<95%) for all microwave-sintered MnO_2-doped 10Sc1CeSZ samples that leads to poor contact between grains, causing an extraordinary contribution to the total resistance, and eventually resulted to lower total conductivity.

At 700 °C, the block factors of the microwave-sintered MnO_2-doped samples were found to be in the range of ~0.47- 0.53 indicating that grain boundary partially block ionic transport, while the migration of oxide ion was more thermally active and caused the bulk conductivity to improve remarkably.

Above 700 °C, the grain boundary blocking effect is vanishing small (block factor < 0.3) for all microwave samples tested. The total resistance was dominated by the bulk resistance, signifying enhanced grain boundary diffusivity of oxide ions in scandia stabilized zirconia ceramics at higher operating temperatures.

CHAPTER 5: CONCLUSIONS AND FUTURE WORKS

5.1: Conclusions

Sustainable energy has emerged as the most pressing challenge facing humanity in the 21st century. Systems based on oxide ion conducting cubic stabilized zirconia are used in a variety of technologically important applications, including in SOFCs for the clean energy generation. Hydrogen can be extracted by electrolysis process using hydro, wind, or solar power. The products of the reaction in the cell are water, electricity, and heat. This is a big improvement over internal combustion engines, coal-burning power plants, and nuclear power plants, all of which produce harmful by-products.

The aims of this research work were to evaluate the effect of dopant and sintering on the properties of ceria-doped scandia stabilized zirconia (10Sc1CeSZ). The effect of manganese oxide addition and sintering temperature on the sinterability and the resulting properties of conventionally sintered 10Sc1CeSZ ceramic were investigated over the temperature range of 1400 °C to 1550 °C. The results were also compared with samples sintered by microwave at low temperature regime.

Based on the observations made from the results and discussion in previous sections, the concluding remarks can be drawn as follows:

Regarding the first objective:

(i) Ceria and scandia were incorporated successfully into the zirconia lattice for the 10Sc1CeSZ ceramic samples prepared from commercially available powder, revealed by the pure cubic XRD signatures. On the other hand, rhombohedral and monoclinic minor peaks were detected from the sintered samples prepared from 10Sc1CeSZ powder synthesized via solid state ball milling reaction.

However, the secondary phase signals were found to reduce with increasing sintering temperatures.

(ii) Grains were found to be fully developed in the 10Sc1CeSZ sintered compacts prepared from softly agglomerated fine commercial powder particles and led to minimum relative density of 98%; whereas randomly distributed pores observed in the sintered compacts prepared from synthesized powder revealed that the loose agglomerates consisting of large scandia flakes required high sintering temperatures for the compacts to be densified.

(iii) The sintered compacts prepared from commercial powder demonstrated higher sintering properties as compared to the synthesized compacts, with a high Vickers hardness of 13- 13.5 GPa, elastic modulus of 180- 200 GPa, and an ionic conductivity value of more than 0.1 S/cm at 800 °C. High conductivities were associated with a high concentration of mobile species and relatively low activation energy for ion migration.

Regarding the second objective:

(i) MnO_2 has been found to be able to induce changes in sintering temperature, hardness, fracture toughness, elastic modulus and electrical conductivity of 10Sc1CeSZ ceramics.

(ii) The cubic phase stability of 10Sc1CeSZ was not disrupted with lower dopant contents of up to 1 wt% MnO_2 throughout the sintering regime employed.

(iii) The additions of up to 1 wt% MnO_2 was found to be beneficial in suppressing the grain growth of cubic zirconia without affecting the mechanical properties of the 10Sc1CeSZ ceramic.

(iv) The addition of high amount of MnO_2 (5 wt%) was found to be detrimental as it affected the cubic phase stability of the zirconia matrix and resulted in grain growth when sintered at higher temperatures.

(v) The inhibited sintering kinetics exhibited by the heavily-doped MnO_2 10Sc1ceSZ ceramics was accompanied by deterioration of the Vickers hardness, fracture toughness, and elastic modulus of the zirconia.

(vi) A higher degree of solidified liquid with large pores was detected with higher MnO_2 dopant concentrations.

(vii) Substantial segregation of silica-rich impurity into discrete silica rich inclusions, $ZrSiO_4$ implied that MnO_2 acted as scavenger in the 10Sc1CeSZ ceramics.

(viii) The doping studies demonstrated that the addition of dopants allows the control and optimization of properties. Apart from the intentional added dopant/ sintering aids, the impact of the unintentionally added impurities and the forming of isolated inclusions were found to destabilize the cubic zirconia and deteriorate the mechanical and electrical performance of the ceramic.

Regarding the third objective:

(i) Microwave sintering employed in this research has been revealed to be beneficial in producing a highly dense 10Sc1CeSZ zirconia ceramic, characterized by having fine grain size below 2 μm coupled with equivalent mechanical properties as that obtained from the high temperature (1550 °C) conventional-sintered sample. The results demonstrated that it is possible to rapid sinter 10Sc1CeSZ using microwave energy at low sintering temperatures.

(ii) Undoped and 0.5-1.0 wt% MnO_2-doped 10Sc1CeSZ sintered samples exhibited similar pure cubic phase contents when sintered at 1300-1350 °C, and did not vary

with both sintering techniques, indicating minor MnO_2 doping did not disrupt phase stability at low temperature regime.

(iii) The grain size of undoped and the MnO_2-doped 10Sc1CeSZ samples obtained after microwave sintering was smaller than those conventionally-sintered samples, ascribed to local dielectric loss at grain boundaries that produce Joule heating and retard grain growth by creating a spatial energy-well that pins the boundary.

(iv) For the undoped zirconia samples, it was suggested that a small amount of silicon phase that was segregated to the grain boundaries formed an ordered array of continuous ring-shaped melting lines. This implied that local heating occurred at grain boundaries of the undoped samples and led to a faster diffusional transport rate while restricting grain growth during sintering.

(v) High Vickers hardness of 13.6-14.2 GPa, fracture toughness of 3.3-3.4 $MPam^{1/2}$, elastic modulus of 198-203 GPa were recorded for the undoped 10Sc1CeSZ samples microwave-sintered at 1350-1350 °C for 15 minutes, whereas minor MnO_2 doping appeared to have significant negative influence on the low temperature microwave sintering process.

(vi) Grain boundary resistivities contribution diminishing at higher operating temperature for all the undoped 10Sc1CeSZ samples sintered through conventional and microwave methods, leading to a high ionic conductivity of 0.314 S/cm recorded at 800 °C for the microwave-sintered (1350 °C) zirconia. The fine-grained microwave-sintered samples showed larger blocking factors compared to conventional sintered samples when measured at 600-700 °C, ascribed to larger volumetric fraction of the more resistive grain boundary. It is postulated that thermally activated creep occurred at 800 °C that can greatly

enhance the grain boundary diffusivity and overcome the activation barrier for the mobility of oxygen ions.

(vii) This research has demonstrated the beneficial effect of rapid sintering via microwave in promoting densification of 10Sc1CeSZ at lower temperatures and sintering times wherein the sintered bodies able to achieve high ionic conductivity without sacrificing the cubic phase and mechanical properties for the SOFC application.

5.2: Future work

Microwave sintering investigated in this research has been demonstrated as a promising rapid heating technique for 10Sc1CeSZ zirconia ceramic at low temperature regime. Future research would encompass further works on low temperature rapid sintering routes and a clearer understanding of the conduction mechanism of the zirconia ceramic doped with various sintering aids or stabilizers, which should include:

1. Microwave sintering of zirconia ceramics could be investigated with other atmospheres such as oxygen deficient environment or inert atmosphere to further reduce the sintering temperatures.

2. Sintering process based on rapid heating techniques to explore the use other energy source such as infrared radiation heating to produce finer microstructure with enhanced electrical and mechanical properties.

3. Two-step or hybrid sintering which involves an initial pre-coarsening step prior to densification could lead to some improvement of the microstructural homogeneity to reduce inhomogeneous deformation caused by differential thermal expansion in the sintered zirconia ceramics with high dopant concentrations.

4. To further understand and model the relationship between zirconia ceramics' performance and its chemical or structural properties, combine experimental and atomistic computer modelling studies (molecular dynamics simulations) may be performed to elucidate the conduction mechanisms of ionic conductors and to identify the driving force or other factors influencing microwave densification.

5. More detailed characterization can be done using various advanced characterization techniques such as transmission electron microscopy for structural and morphology analysis, Auger electron spectroscopy for depth elemental profiling, high resolution neutron diffraction for high penetration depth can be used to provide fresh insight into complex 3D oxide structure, and Secondary Ion Mass Spectroscopy (SIMS) can be used to determine the diffusion coefficient of Mn in 10Sc1CeSZ involving bulk and grain boundary diffusion.

6. Applying nanotechnology to prepare nanostructured zirconia materials using 3D nanoprinting or electrospinning techniques to increase the electrolyte performance.

REFERENCES

Abdala, P. M., Custo, G. S., & Lamas, D. G. (2010). Enhanced ionic transport in fine-grained scandia-stabilized zirconia ceramics. *Journal of Power Sources*, *195*(11), 3402-3406.

Agrawal, D. (2006). Microwave sintering of ceramics, composites and metallic materials, and melting of glasses. *Transactions of the Indian Ceramic Society*, *65*(3), 129-144.

ASTM Standard (2004). E112-96 (2004)e2: Standard test methods for determining average grain size.

ASTM Standard (2008). C1327-08: Standard Test Method for Vickers Indentation Hardness of Advanced Ceramics.

ASTM Standard (2008). D3663-03: Standard Test Method for Surface Area of Catalysts and Catalyst Carriers.

ASTM Standard (2009). E1876-09: Standard Test Method for Dynamic Young's Modulus, Shear Modulus, and Poisson's Ratio by Impulse Excitation of Vibration. West Conshohocken, PA: ASTM International.

Badwal, S. P. S., & Foger, K. (1996). Solid oxide electrolyte fuel cell review. *Ceramics International*, *22*(3), 257-265.

Badwal, S. P. S., Ciacchi, F. T., & Milosevic, D. (2000). Scandia–zirconia electrolytes for intermediate temperature solid oxide fuel cell operation. *Solid State Ionics*, *136*, 91-99.

Badwal, S. P. S. (2001). Stability of solid oxide fuel cell components. *Solid State Ionics*, *143*(1), 39-46.

Bai, B., Sammes, N. M., & Smirnova, A. L. (2008). Physical and electrochemical characterization of Bi_2O_3-doped scandia stabilized zirconia. *Journal of Power Sources*, *176*(1), 76-81.

Barsoukov, E., & Macdonald, J. R. (Eds.). (2005). *Impedance spectroscopy: theory, experiment, and applications*. John Wiley & Sons.

Barsoum, M., & Barsoum, M. W. (2002). *Fundamentals of ceramics*. CRC press.

Baur, E., & Preis, H. (1937). About fuel chains with fixed conductors. *Journal of Applied Electrochemistry and Physical Chemistry* , *43* (9), 727-732.

Beekmans, N. M., & Heyne, L. (1976). Correlation between impedance, microstructure and composition of calcia-stabilized zirconia. *Electrochimica Acta*, *21*(4), 303-310.

Behling, N. H. (2012). *Fuel cells: current technology challenges and future research needs*. Newnes.

Bhattacharya, M., & Basak, T. (2016). A review on the susceptor assisted microwave processing of materials. *Energy*, *97*, 306-338.

Biresselioglu, M. E., & Yelkenci, T. (2016). Scrutinizing the causality relationships between prices, production and consumption of fossil fuels: A panel data approach. *Energy*, *102*, 44-53.

Birnboim, A., Gershon, D., Calame, J., Birman, A., Carmel, Y., Rodgers, J., ... & Semenov, V. E. (1998). Comparative study of microwave sintering of zinc oxide at 2.45, 30, and 83 GHz. *Journal of the American Ceramic Society*, *81*(6), 1493-1501.

Bohnke, O., Gunes, V., Kravchyk, K. V., Belous, A. G., Yanchevskii, O. Z., & V'Yunov, O. I. (2014). Ionic and electronic conductivity of 3mol% Fe_2O_3-substituted cubic yttria-stabilized ZrO_2 (YSZ) and scandia-stabilized ZrO_2 (ScSZ). *Solid State Ionics*, *262*, 517-521.

Borodianska, H., Demirskyi, D., Sakka, Y., Badica, P., & Vasylkiv, O. (2012). Grain boundary diffusion driven spark plasma sintering of nanocrystalline zirconia. *Ceramics International*, *38*(5), 4385-4389.

Borrell, A., Salvador, M. D., Rayón, E., & Peñaranda-Foix, F. L. (2012). Improvement of microstructural properties of 3Y-TZP materials by conventional and non-conventional sintering techniques. *Ceramics International*, *38*(1), 39-43.

Boukamp, B. A., Raming, T. P., Winnubst, A. J. A., & Verweij, H. (2003). Electrochemical characterisation of 3Y-TZP–Fe_2O_3 composites. *Solid State Ionics*, *158*(3), 381-394.

Brandon, N. P., Blake, A., Corcoran, D., Cumming, D., Duckett, A., El-Koury, K., ... & Matthews, C. (2004). Development of metal supported solid oxide fuel cells for operation at 500–600 C. *Journal of Fuel Cell Science and Technology*, *1*(1), 61-65.

Breval, E., Cheng, J. P., Agrawal, D. K., Gigl, P., Dennis, M., Roy, R., & Papworth, A. J. (2005). Comparison between microwave and conventional sintering of WC/Co composites. *Materials Science and Engineering: A*,*391*(1), 285-295.

Cha, S. W., Colella, W., & Prinz, F. B. (2006). *Fuel cell fundamentals* (Vol. 2). New York: John Wiley & Sons.

Chandrasekaran, S., Ramanathan, S., & Basak, T. (2012). Microwave material processing—a review. *AIChE Journal*, *58*(2), 330-363.

Charpentier, P., Fragnaud, P., Schleich, D. M., & Gehain, E. (2000). Preparation of thin film SOFCs working at reduced temperature. *Solid State Ionics*, *135*(1), 373-380.

Chen, F., Jin, D., Tyeb, K., Wang, B., Han, Y. H., Kim, S., ... & Zhang, L. (2015). Field assisted sintering of graphene reinforced zirconia ceramics. *Ceramics International*, *41*(4), 6113-6116.

Chiba, R., Ishii, T., & Yoshimura, F. (1996). Temperature dependence of ionic conductivity in (1− x) ZrO_2−(x− y) Sc_2O_3− yYb_2O_3 electrolyte material. *Solid State Ionics*, *91*(3), 249-256.

Chong, F. D., Tan, C. Y., Singh, R., Muchtar, A., Somalu, M. R., Ng, C. K., ... & Tan, Y. M. (2016). Effect of manganese oxide on the sinterability of 8mol% yttria-stabilized zirconia. *Materials Characterization*, *120*, 331-336.

Cologna, M., Rashkova, B., & Raj, R. (2010). Flash Sintering of Nanograin Zirconia in< 5 s at 850 C. *Journal of the American Ceramic Society*, *93*(11), 3556-3559.

Colomer, M. T., Guglieri, C., Díaz-Moreno, S., Maczka, M., Boada, R., & Chaboy, J. (2016). Effect of titania doping and sintering temperature on titanium local environment and electrical conductivity of YSZ. *Journal of Alloys and Compounds*, *689*, 512-524.

Conrad, H., & Yang, D. (2011). Dependence of the sintering rate and related grain size of yttria-stabilized polycrystalline zirconia (3Y-TZP) on the strength of an applied DC electric field. *Materials Science and Engineering: A*, *528*(29), 8523-8529.

Cook, B. (2002). Introduction to fuel cells and hydrogen technology. *Engineering science and education journal, 11*(6), 205-216.

Das, S., Mukhopadhyay, A. K., Datta, S., & Basu, D. (2009). Prospects of microwave processing: An overview. *Bulletin of Materials Science*, *32*(1), 1-13.

Dasari, H. P., Ahn, J. S., Ahn, K., Park, S. Y., Hong, J., Kim, H., ... & Lee, J. H. (2014). Synthesis, sintering and conductivity behavior of ceria-doped scandia-stabilized zirconia. *Solid State Ionics*, *263*, 103-109.

De Florio, D. Z., & Muccillo, R. (2004). Effect of boron oxide on the cubic-to-monoclinic phase transition in yttria-stabilized zirconia. *Materials Research Bulletin*, *39*(10), 1539-1548.

De Florio, D. Z., Fonseca, F. C., Muccillo, E. N. S., & Muccillo, R. (2004). Materiais cerâmicos para células a combustível (Ceramic materials for fuel cells). *Cerâmica*, *50*(316), 275-290.

De Jonghe, L. C., & Rahaman, M. N. (2003). Sintering of ceramics. *Handbook of advanced ceramics*, *1*, 187-264.

De Souza, D. P. F., & De Souza, M. F. (1999). Liquid phase sintering of RE_2O_3: YSZ ceramics Part I Grain growth and expelling of the grain boundary glass phase. *Journal of materials science*, *34*(16), 4023-4030.

Demirskyi, D., Borodianska, H., Grasso, S., Sakka, Y., & Vasylkiv, O. (2011). Microstructure evolution during field-assisted sintering of zirconia spheres. *Scripta Materialia*, *65*(8), 683-686.

Dey, A., Gupta, A. D., Basu, D., Ambashta, R. D., Wattal, P. K., Kumar, S., ... & Mazumder, S. (2013). A comparative study of conventionally sintered,

microwave sintered and hot isostatic press sintered NZP and CZP structures interacted with fluoride. *Ceramics International*, *39*(8), 9351-9359.

Doshi, R., Richards, V. L., Carter, J. D., Wang, X., & Krumpelt, M. (1999). Development of solid oxide fuel cells that operate at 500° C. *Journal of The Electrochemical Society*, *146*(4), 1273-1278.

Du, Y., Stevenson, A. J., Vernat, D., Diaz, M., & Marinha, D. (2016). Estimating Joule heating and ionic conductivity during flash sintering of 8YSZ. *Journal of the European Ceramic Society*, *36*(3), 749-759.

Elyassi, B., Sahimi, M., & Tsotsis, T. T. (2009). Inorganic Membranes. *Encyclopedia of Chemical Processing*, 1-16.

Evans, A. G., & Charles, E. A. (1976). Fracture toughness determinations by indentation. *Journal of the American Ceramic society*, *59*(7-8), 371-372.

Fergus, J. W. (2006). Electrolytes for solid oxide fuel cells. *Journal of Power Sources*, *162*(1), 30-40.

Figueiredo, F. M. L., & Marques, F. M. B. (2013). Electrolytes for solid oxide fuel cells. *Wiley Interdisciplinary Reviews: Energy and Environment*, *2*(1), 52-72.

Flegler, A. J., Burye, T. E., Yang, Q., & Nicholas, J. D. (2014). Cubic yttria stabilized zirconia sintering additive impacts: A comparative study. *Ceramics International*, *40*(10), 16323-16335.

Francois, B., & KINGERY W. D. (1983). *Physical Metallurgy*, edited by Cohn, R. W. & Haasan, P., 3rd ed. Elsevier Science Publishers BV pp. 499–525.

Gao, Z., Mao, Z., Wang, C., & Liu, Z. (2010). Development of trimetallic Ni–Cu–Zn anode for low temperature solid oxide fuel cells with composite electrolyte. *International journal of hydrogen energy*, *35*(23), 12897-12904.

German, R. M., Suri, P., & Park, S. J. (2009). Review: liquid phase sintering. *Journal of Materials Science*, *44*(1), 1-39.

Gödickemeier, M., Michel, B., Orliukas, A., Bohac, P., Sasaki, K., Gauckler, L., ... & Frei, O. (1994). Effect of intergranular glass films on the electrical conductivity of 3Y-TZP. *Journal of materials research*, *9*(05), 1228-1240.

Goodenough, J. B. (2003). Oxide-ion electrolytes. *Annual review of materials research*, *33*(1), 91-128.

Grosso, R. L., & Muccillo, E. N. S. (2013). Sintering, phase composition and ionic conductivity of zirconia–scandia–ceria. *Journal of Power Sources*, *233*, 6-13.

Grosso, R. L., Tertuliano, A. J., Machado, I. F., & Muccillo, E. N. S. (2016). Structural and electrical properties of spark plasma sintered scandia-and dysprosia-stabilized zirconia. *Solid State Ionics*, *288*, 94-97.

Grove, W. R. (1839). XXIV. On voltaic series and the combination of gases by platinum. *The London and Edinburgh Philosophical Magazine and Journal of Science*, *14*(86), 127-130.

Guo, X. (2003). Roles of alumina in zirconia for functional applications. *Journal of the American Ceramic Society*, *86*(11), 1867-1873.

Guo, C. X., Wang, J. X., He, C. R., & Wang, W. G. (2013). Effect of alumina on the properties of ceria and scandia co-doped zirconia for electrolyte-supported SOFC. *Ceramics International*, *39*(8), 9575-9582.

Haering, C., Roosen, A., Schichl, H., & Schnöller, M. (2005). Degradation of the electrical conductivity in stabilised zirconia system: Part II: scandia-stabilised zirconia. *Solid State Ionics*, *176*(3), 261-268.

Haile, S. M. (2003). Fuel cell materials and components. *Acta Materialia*, *51*(19), 5981-6000.

Hart, N., Brandon, N., & Shemilt, J. (2000). Environmental evaluation of thick film ceramic fabrication techniques for solid oxide fuel cells. *Materials and Manufacturing Processes*, *15*(1), 47-64.

Hassan, A. A. E., Menzler, N. H., Blass, G., Ali, M. E., Buchkremer, H. P., & Stöver, D. (2002). Influence of alumina dopant on the properties of yttria-stabilized zirconia for SOFC applications. *Journal of materials science*, *37*(16), 3467-3475.

Heel, A., Vital, A., Holtappels, P., & Graule, T. (2009). Flame spray synthesis and characterisation of stabilised ZrO2 and CeO2 electrolyte nanopowders for SOFC applications at intermediate temperatures. *Journal of electroceramics*, *22*(1-3), 40-46.

Hirano, M., Oda, T., Ukai, K., & Mizutani, Y. (2003). Effect of Bi_2O_3 additives in Sc stabilized zirconia electrolyte on a stability of crystal phase and electrolyte properties. *Solid State Ionics*, *158*(3), 215-223.

Hiwatashi, K. (2009). *U.S. Patent No. 7,569,292*. Washington, DC: U.S. Patent and Trademark Office.

Hoffmann, P., & Dorgan, B. (2012). *Tomorrow's energy: hydrogen, fuel cells, and the prospects for a cleaner planet*. MIT press.

Holland, B. J., Zhu, J. G., & Jamet, L. (2007). Fuel cell technology and application. *University of Technology. Sydney*.

Huang, Y. L., Lee, Y. C., Tsai, D. C., Huang, R. H., & Shieu, F. S. (2014). Phase stability and microstructure of manganese-doped calcia-stabilized zirconia heat treated in a reducing atmosphere. *Ceramics International*, *40*(1), 2373-2379.

Irvine, J. T., Sinclair, D. C., & West, A. R. (1990). Electroceramics: characterization by impedance spectroscopy. *Advanced Materials*, *2*(3), 132-138.

Irvine, J. T., & Connor, P. (Eds.). (2012). *Solid oxide fuels cells: facts and figures: past present and future perspectives for SOFC technologies*. Springer Science & Business Media.

Jacobson, A. J. (2009). Materials for solid oxide fuel cells. *Chemistry of Materials*, *22*(3), 660-674.

Ji, W., Parker, B., Falco, S., Zhang, J. Y., Fu, Z. Y., & Todd, R. I. (2017). Ultra-fast firing: Effect of heating rate on sintering of 3YSZ, with and without an electric field. *Journal of the European Ceramic Society*, *37*(6), 2547-2551.

Joshi, A. V., Steppan, J. J., Taylor, D. M., & Elangovan, S. (2004). Solid electrolyte materials, devices, and applications. *Journal of electroceramics*, *13*(1-3), 619-625

Kazlauskas, S., Kežionis, A., Šalkus, T., & Orliukas, A. F. (2012). Sintering of oxygen ion conductive ceramics and their electrical properties. *Lithuanian Journal of Physics*, *52*(3).

Kee, R. J., Zhu, H., Sukeshini, A. M., & Jackson, G. S. (2008). Solid oxide fuel cells: operating principles, current challenges, and the role of syngas. *Combustion Science and Technology*, *180*(6), 1207-1244.

Kesapragada, S. V., Bhaduri, S. B., Bhaduri, S., & Singh, P. (2003). Densification of LSGM electrolytes using activated microwave sintering. *Journal of power sources*, *124*(2), 499-504.

Kharton, V. V., Figueiredo, F. M., Navarro, L., Naumovich, E. N., Kovalevsky, A. V., Yaremchenko, A. A., ... & Frade, J. R. (2001). Ceria-based materials for solid oxide fuel cells. *Journal of Materials Science*, *36*(5), 1105-1117.

Khan, M. M., Ramesh, S., Bang, L. T., Wong, Y. H., Ubenthiran, S., Tan, C. Y., ... & Misran, H. (2014). Effect of Copper Oxide and Manganese Oxide on Properties and Low Temperature Degradation of Sintered Y-TZP Ceramic.*Journal of Materials Engineering and Performance*, *23*(12), 4328-4335.

Kim, M. J., Ahn, J. S., Kim, J. H., Kim, H. Y., & Kim, W. C. (2013). Effects of the sintering conditions of dental zirconia ceramics on the grain size and translucency. *The journal of advanced prosthodontics*, *5*(2), 161-166.

Kirubakaran, A., Jain, S., & Nema, R. K. (2009). A review on fuel cell technologies and power electronic interface. *Renewable and Sustainable Energy Reviews*, *13*(9), 2430-2440.

Kishimoto, H., Sakai, N., Yamaji, K., Horita, T., Xiong, Y. P., Brito, M. E., & Yokokawa, H. (2009). Destabilization of cubic-stabilized zirconia electrolyte induced by boron oxide under reducing atmosphere. *Journal of materials science*, *44*(2), 639-646.

Kondoh, J., Tomii, Y., & Kawachi, K. (2003). Changes in Aging Behavior and Defect Structure of Yttria-Fully-Stabilized ZrO_2 with Sc_2O_3 Doping. *Journal of the American Ceramic Society*, *86*(12), 2093-2102.

Kravchyk, K. V., Bohnke, O., Gunes, V., Belous, A. G., Pashkova, E. V., Le Lannic, J., & Gouttefangeas, F. (2012). Ionic and electronic conductivity of 3mol% Fe_2O_3-substituted cubic Y-stabilized ZrO_2. *Solid State Ionics*, *226*, 53-58.

Kubrin, R., Blugan, G., & Kuebler, J. (2017). Influence of cerium doping on mechanical properties of tetragonal scandium-stabilized zirconia. *Journal of the European Ceramic Society*. 37, 1651-1656.

Kumar, B., & Thokchom, J. S. (2008). Space Charge-Mediated Ionic Transport in Yttria-Stabilized Zirconia–Alumina Composite Membranes. *Journal of the American Ceramic Society*, *91*(4), 1175-1181.

Kumar, A., Jaiswal, A., Sanbui, M., & Omar, S. (2016). Scandia stabilized zirconia-ceria solid electrolyte (xSc1CeSZ, 5< x< 11) for IT-SOFCs: Structure and conductivity studies. *Scripta Materialia*, *121*, 10-13.

Kushi, T., Sato, K., Unemoto, A., Amezawa, K., & Kawada, T. (2009). Investigation of high temperature elastic modulus and internal friction of SOFC electrolytes using resonance method. *ECS Transactions*, *25*(2), 1673-1677.

Kwa, S. M., Ramesh, S., Bang, L. T., Wong, Y. H., Chew, W. J., Tan, C. Y., ... & Teng, W. D. (2015). Effect of sintering holding time on the properties and low-temperature degradation behaviour of manganese oxide-doped Y-TZP ceramic. *Journal of Ceramic Processing Research*, *16*(2), 193-198.

Kyrpa, O. L. (2013). On the temperature dependence of oxygen ionic conductivity of 10Sc1CeSZ electrolytes. The National Academy of Sciences of Ukraine.

Laguna-Bercero, M. A., Skinner, S. J., & Kilner, J. A. (2009). Performance of solid oxide electrolysis cells based on scandia stabilised zirconia. *Journal of Power Sources*, *192*(1), 126-131.

Lee, J. H., Mori, T., Li, J. G., Ikegami, T., Komatsu, M., & Haneda, H. (2000). Improvement of Grain-Boundary Conductivity of 8 mol% Yttria-Stabilized Zirconia by Precursor Scavenging of Siliceous Phase. *Journal of the electrochemical society*, *147*(7), 2822-2829.

Lee, J. H., Mori, T., Li, J. G., Ikegami, T., Drennan, J., & Kim, D. Y. (2001). Scavenging of Siliceous Grain-Boundary Phase of 8-mol%-Ytterbia-Stabilized Zirconia without Additive. *Journal of the American Ceramic Society*, *84*(11), 2734-2736.

Lee, D. S., Kim, W. S., Choi, S. H., Kim, J., Lee, H. W., & Lee, J. H. (2005). Characterization of ZrO_2 co-doped with Sc_2O_3 and CeO_2 electrolyte for the application of intermediate temperature SOFCs. *Solid State Ionics*, *176*(1), 33-39.

Lee, J. S., Lerch, M., & Maier, J. (2006). Nitrogen-doped zirconia: A comparison with cation stabilized zirconia. *Journal of Solid State Chemistry*, *179*(1), 270-277.

Lefeuvre, S., Federova, E., Gomonova, O., & Tao, J. (2010). Microwave Sintering of Micro-and Nano-Sized Alumina Powder. *Advances in Modeling of Microwave sintering*, 8-9.

Lei, Z., & Zhu, Q. (2007). Phase transformation and low temperature sintering of manganese oxide and scandia co-doped zirconia. *Materials Letters*, *61*(6), 1311-1314.

Li, G., & Ren, R. (2011). Preparation of YSZ-TZP solid electrolytes by gel-casting technology. *Journal of Environmental Sciences*, *23*, S170-S172.

Liu, Y., Tan, X., & Li, K. (2006). Mixed conducting ceramics for catalytic membrane processing. *Catalysis Reviews*, *48*(02), 145-198.

Liu, M., He, C., Wang, J., Wang, W. G., & Wang, Z. (2010). Investigation of (CeO_2) x $(Sc_2O_3)(0.11-x)(ZrO_2)$ 0.89(x=0.01–0.10) electrolyte materials for intermediate-temperature solid oxide fuel cell. *Journal of Alloys and Compounds*, *502*(2), 319-323.

Lvovich, V. F. (2012). *Impedance spectroscopy: applications to electrochemical and dielectric phenomena*. John Wiley & Sons.

Mahapatra, M. K., Singh, P., & Misture, S. T. (2012). Manganese induced modifications in yttria stabilized zirconia. *Applied Physics Letters*, *101*(13), 131606.

Mahato, N., Banerjee, A., Gupta, A., Omar, S., & Balani, K. (2015). Progress in material selection for solid oxide fuel cell technology: A review. *Progress in Materials Science*, *72*, 141-337.

Maiti, S., Pastor, M., Sundaram, R. S., Ravichandran, J., Kumar, A., Biswas, K., & Manna, I. (2009). Synthesis and characterization of nanocrystalline dysprosia stabilized zirconia based electrolyte for intermediate-temperature solid oxide fuel cell. *Journal of Alloys and Compounds*, *475*(1), 587-591.

Maurya, R., Gupta, A., Omar, S., & Balani, K. (2016). Effect of sintering on mechanical properties of ceria reinforced yttria stabilized zirconia. *Ceramics International*, *42*(9), 11393-11403.

Mazaheri, M., Hesabi, Z. R., Golestani-Fard, F., Mollazadeh, S., Jafari, S., & Sadrnezhaad, S. K. (2009). The effect of conformation method and sintering technique on the densification and grain growth of nanocrystalline 8 mol% Yttria-Stabilized Zirconia. *Journal of the American Ceramic Society*, *92*(5), 990-995.

Meenaloshini, S., Ramesh, S., Sopyan, I., & Teng, W. D. (2008). Densification Studies of Tetragonal Zirconia with Manganese as Sintering Additive. In *Int. Conf. Constr. Build. Technol* (Vol. 17, pp. 187-196).

Mekhilef, S., Saidur, R., & Safari, A. (2012). Comparative study of different fuel cell technologies. *Renewable and Sustainable Energy Reviews*, *16*(1), 981-989.

Mendelson, M. I. (1969). Average grain size in polycrystalline ceramics. *Journal of the American Ceramic Society*, *52*(8), 443-446.

Menezes, R. R., & Kiminami, R. H. G. A. (2008). Microwave sintering of alumina–zirconia nanocomposites. *Journal of Materials Processing Technology*, *203*(1), 513-517.

Mizutani, Y., Kawai, M., Nomura, K., Nakamura, Y., & Yamamoto, O. (1999). Characteristics of substrate type SOFC using Sc-doped zirconia electrolytes.*Vol. 99-19*, 185-192.

Morales, M., Roa, J. J., Capdevila, X. G., Segarra, M., & Piñol, S. (2010). Mechanical properties at the nanometer scale of GDC and YSZ used as electrolytes for solid oxide fuel cells. *Acta materialia*, *58*(7), 2504-2509.

Mori, M., Liu, Y., Ma, S., Hashimoto, S. I., & Takei, K. (2008). Investigation of Li dopant as a sintering aid for ScSZ electrolyte for IT-SOFC. *Journal of the Korean Ceramic Society*, *45*(12), 760-765.

Muccillo, R., & Muccillo, E. N. S. (2013). An experimental setup for shrinkage evaluation during electric field-assisted flash sintering: application to yttria-stabilized zirconia. *Journal of the European Ceramic Society*, *33*(3), 515-520.

Munir, Z. A., Anselmi-Tamburini, U., & Ohyanagi, M. (2006). The effect of electric field and pressure on the synthesis and consolidation of materials: a review of the spark plasma sintering method. *Journal of Materials Science*, *41*(3), 763-777.

Naik, K. S., Sglavo, V. M., & Raj, R. (2014). Field assisted sintering of ceramic constituted by alumina and yttria stabilized zirconia. *Journal of the European Ceramic Society*, *34*(10), 2435-2442.

Nath, S., Basu, B., & Sinha, A. (2006). A comparative study of conventional sintering with microwave sintering of hydroxyapatite synthesized by chemical route. *Trends in Biomaterials & Artificial Organs*, *19*(2), 93-98.

Nernst, W. (1901). *U.S. Patent No. 685,730*. Washington, DC: U.S. Patent and Trademark Office.

Niihara, K., Morena, R., & Hasselman, D. P. H. (1982). Evaluation ofK Ic of brittle solids by the indentation method with low crack-to-indent ratios.*Journal of Materials Science Letters*, *1*(1), 13-16.

Oghbaei, M., & Mirzaee, O. (2010). Microwave versus conventional sintering: a review of fundamentals, advantages and applications. *Journal of Alloys and Compounds*, *494*(1), 175-189.

Olevsky, E. A., Kandukuri, S., & Froyen, L. (2007). Consolidation enhancement in spark-plasma sintering: Impact of high heating rates. *Journal of Applied Physics*, *102*(11), 114913.

Omar, S., Bin Najib, W., Chen, W., & Bonanos, N. (2012). Electrical Conductivity of 10 mol% Sc_2O_3– 1 mol% M_2O_3–ZrO_2 Ceramics. *Journal of the American Ceramic Society*, *95*(6), 1965-1972.

Orera, A., & Slater, P. R. (2009). New Chemical Systems for Solid Oxide Fuel Cells. *Chemistry of Materials*, *22*(3), 675-690.

Ormerod, R. M. (2003). Solid oxide fuel cells. *Chemical Society Reviews*, *32*(1), 17-28.

Orlovskaya, N., Lukich, S., Subhash, G., Graule, T., & Kuebler, J. (2010). Mechanical properties of 10mol% Sc 2 O 3–1mol% CeO 2–89mol% ZrO 2 ceramics. *Journal of Power Sources*, *195*(9), 2774-2781.

Padmavathi, C., Upadhyaya, A., & Agrawal, D. (2011). Effect of microwave and conventional heating on sintering behavior and properties of Al–Mg–Si–Cu alloy. *Materials chemistry and physics*, *130*(1), 449-457.

Peck, D. H., Choi, Y. H., Woo, S. K., Song, R. H., Wackerl, J., & Markus, T. (2007). Fabrication of Porous Structure with Scandia Stabilized Zirconia Electrolyte for Solid Oxide Fuel Cell. *ECS Transactions*, *7*(1), 2187-2195.

Perry, M. L., & Fuller, T. F. (2002). A historical perspective of fuel cell technology in the 20th century. *Journal-Electrochemical Society*, *149*(7), S59-S67.

Piva, R. H., Piva, D. H., & Morelli, M. R. (2017). Thermal stability and phase transformation in fully indium oxide (InO 1.5) stabilized zirconia. *Materials Characterization*, *123*, 58-66.

Politova, T. I., & Irvine, J. T. S. (2004). Investigation of scandia–yttria–zirconia system as an electrolyte material for intermediate temperature fuel cells—influence of yttria content in system $(Y_2O_3)_x(Sc_2O_3)_{(11-x)}(ZrO_2)_{89}$. *Solid State Ionics*, *168*(1), 153-165.

Preis, W., Waldhäusl, J., Egger, A., Sitte, W., De Carvalho, E., & Irvine, J. T. S. (2011). Electrical properties of bulk and grain boundaries of scandia-stabilized zirconia co-doped with yttria and ceria. *Solid State Ionics*, *192*(1), 148-152.

Raj, R., Cologna, M., & Francis, J. S. (2011). Influence of externally imposed and internally generated electrical fields on grain growth, diffusional creep, sintering and related phenomena in ceramics. *Journal of the American Ceramic Society*, *94*(7), 1941-1965.

Rajeswari, K., Hareesh, U. S., Subasri, R., Chakravarty, D., & Johnson, R. (2010). Comparative evaluation of spark plasma (SPS), microwave (MWS), two stage sintering (TSS) and conventional sintering (CRH) on the densification and micro structural evolution of fully stabilized zirconia ceramics. *Science of Sintering*, *42*(3), 259-267

Rajeswari, K., Suresh, M. B., Hareesh, U. S., Rao, Y. S., Das, D., & Johnson, R. (2011). Studies on ionic conductivity of stabilized zirconia ceramics (8YSZ) densified through conventional and non-conventional sintering methodologies. *Ceramics International*, *37*(8), 3557-3564.

Ramesh, S., Meenaloshini, S., Tan, C. Y., Chew, W. K., & Teng, W. D. (2008). Effect of manganese oxide on the sintered properties and low temperature degradation of Y-TZP ceramics. *Ceramics International*, *34*(7), 1603-1608.

Ramesh, S., Amiriyan, M., Meenaloshini, S., Tolouei, R., Hamdi, M., Pruboloksono, J., & Teng, W. D. (2011). Densification behaviour and properties of manganese oxide doped Y-TZP ceramics. *Ceramics International*, *37*(8), 3583-3590.

Ramesh, S., Chew, W. K., Tan, C. Y., Purbolaksono, J., Noor, A. M., Hassan, M. A., ... & Teng, W. D. (2013). Influence of Manganese on the Sintering Properties of Tetragonal Zirconia. *Ceram. Silik*, *57*, 28-32.

Revankar, S. T., & Majumdar, P. (2014). *Fuel cells: principles, design, and analysis*. CRC Press.

Rosten, R., Koski, M., & Koppana, E. (2006). A Guide to the Calculation of Theoretical Densities of Crystal Structures for Solid Oxide Fuel Cells. *Journal of Undergraduate Materials Research*, *2*, 38-41.

Sarat, S., Sammes, N., & Smirnova, A. (2006). Bismuth oxide doped scandia-stabilized zirconia electrolyte for the intermediate temperature solid oxide fuel cells. *Journal of Power Sources*, *160*(2), 892-896.

Shackelford, J. F., Han, Y. H., Kim, S., & Kwon, S. H. (2016). *CRC Materials Science and Engineering Handbook*. CRC press.

Shi, H., Ran, R., & Shao, Z. (2012). Wet powder spraying fabrication and performance optimization of IT-SOFCs with thin-film ScSZ electrolyte.*international journal of hydrogen energy*, *37*(1), 1125-1132.

Shimazu, M., Yamaji, K., Isobe, T., Ueno, A., Kishimoto, H., Katsumata, K. I., ... & Okada, K. (2011). Stability of Sc_2O_3 and CeO_2 co-doped ZrO_2 electrolyte during the operation of solid oxide fuel cells: Part II the influences of Mn, Al and Si. *Solid State Ionics*, *204*, 120-128.

Singh, K. L., Sharma, P., Singh, A. P., Kumar, A., & Sekhon, S. S. (2016). Structural and Electrical Analysis of Microwave Processed YSZ Electrolytes for SOFC Prepared by Co-precipitation Method. *JOM*, 1-5.

Singhal, S. C. (2000). Advances in solid oxide fuel cell technology. *Solid State Ionics*, *135*(1), 305-313.

Singhal, S. C., & Kendall, K. (Eds.) (2003). *High-temperature solid oxide fuel cells: fundamentals, design and applications*. Elsevier Science Ltd, ISBN 1-85617-387-9, Oxford, UK.

Śnieżek, E., Szczerba, J., Stoch, P., Prorok, R., Jastrzębska, I., Bodnar, W., & Burkel, E. (2016). Structural properties of MgO–ZrO 2 ceramics obtained by conventional sintering, arc melting and field assisted sintering technique. *Materials & Design*, *99*, 412-420.

Souto, P. M. D., Menezes, R. R., & Kiminami, R. H. G. A. (2007). Microwave hybrid sintering of mullite powders. *American Ceramic Society Bulletin*, *86*(1), 9201-9206.

Stambouli, A. B., & Traversa, E. (2002). Solid oxide fuel cells (SOFCs): a review of an environmentally clean and efficient source of energy. *Renewable and Sustainable Energy Reviews*, *6*(5), 433-455.

Steele, B. C., & Heinzel, A. (2001). Materials for fuel-cell technologies. *Nature*, *414*(6861), 345-352.

Sun, C., & Stimming, U. (2007). Recent anode advances in solid oxide fuel cells. *Journal of Power Sources*, *171*(2), 247-260.

Sun, C., Hui, R., & Roller, J. (2010). Cathode materials for solid oxide fuel cells: a review. *Journal of Solid State Electrochemistry*, *14*(7), 1125-1144.

Sutton, W. H. (1989). Microwave processing of ceramic materials. *American Ceramic Society Bulletin*, *68*(2), 376-386.

Taroco, H. A., Santos, J. A. F., Domingues, R. Z., & Matencio, T. (2011). *Ceramic materials for solid oxide fuel cells*. INTECH Open Access Publisher.

Tejuca, L. G., & Fierro, J. L. G. (Eds.). (2000). *Properties and applications of perovskite-type oxides*. CRC Press.

Thridandapani, R. R., Folz, D. C., & Clark, D. E. (2015). Effect of electric field (2.45 GHz) on sintering behavior of fully stabilized zirconia. *Journal of the European Ceramic Society*, *35*(7), 2145-2152.

Ukai, K., Mizutani, Y., Kume, Y., & Yamamoto, O. (2001). Current status of SOFC development using scandia doped Zirconia. *SOFC VII*, *375*.

Verkerk, M. J., Middelhuis, B. J., & Burggraaf, A. J. (1982). Effect of grain boundaries on the conductivity of high-purity ZrO_2-Y_2O_3 ceramics. *Solid State Ionics*, *6*(2), 159-170.

Voltsihhin, N., Rodríguez, M., Hussainova, I., & Aghayan, M. (2014). Low temperature, spark plasma sintering behavior of zirconia added by a novel type of alumina nanofibers. *Ceramics International*, *40*(5), 7235-7244.

Wang, L., Zhou, J., Liu, G., Ouyang, S., & Liu, H. (2007). Structure and properties of microwave sintering ZnO ceramics. *Ferroelectrics*, *356*(1), 185-188.

West, A. R. (2007). *Solid state chemistry and its applications*. John Wiley & Sons.

Wincewicz, K. C., & Cooper, J. S. (2005). Taxonomies of SOFC material and manufacturing alternatives. *Journal of Power Sources*, *140*(2), 280-296.

Yarmolenko, S., Sankar, J., Bernier, N., Klimov, M., Kapat, J., & Orlovskaya, N. (2009). Phase stability and sintering behavior of 10mol% Sc_2O_3–1mol% CeO_2–ZrO_2 ceramics. *Journal of Fuel Cell Science and Technology*, *6*(2), 021007.

Yokokawa, H., Sakai, N., Horita, T., & Yamaji, K. (2001). Recent developments in solid oxide fuel cell materials. *Fuel cells, 1*(2), 117-131.

Yuan, X. Z. R., Song, C., Wang, H., & Zhang, J. (2009). *Electrochemical impedance spectroscopy in PEM fuel cells: fundamentals and applications*. Springer Science & Business Media.

Zevalkink, R., Hunter, A., Swanson, M., Johnson, C., Kapat, J., & Orlovskaya, N. (2007). Processing and Characterization of Sc2O3-CeO2-ZrO2 Electrolyte Based Intermediate Temperature Solid Oxide Fuel Cells. In *MRS Proceedings* (Vol. 972, pp. 0972-AA03). Cambridge University Press.

Zhang, T., Kong, L., Zeng, Z., Huang, H., Hing, P., Xia, Z., & Kilner, J. (2003). Sintering behavior and ionic conductivity of Ce0. 8Gd0. 2O1. 9 with a small amount of MnO2 doping. *Journal of solid state electrochemistry*, *7*(6), 348-354.

Zhang, C., Li, C. J., Zhang, G., Ning, X. J., Li, C. X., Liao, H., & Coddet, C. (2007). Ionic conductivity and its temperature dependence of atmospheric plasma-sprayed yttria stabilized zirconia electrolyte. *Materials Science and Engineering: B*, *137*(1), 24-30.

Zhang, Y., Malzbender, J., Mack, D. E., Jarligo, M. O., Cao, X., Li, Q., ... & Stöver, D. (2013). Mechanical properties of zirconia composite ceramics. *Ceramics International*, *39*(7), 7595-7603.

Zhao, C., Vleugels, J., Groffils, C., Luypaert, P. J., & Van der Biest, O. (2000). Hybrid sintering with a tubular susceptor in a cylindrical single-mode microwave furnace. *Acta Materialia*, *48*(14), 3795-3801.

LIST OF PUBLICATIONS AND PAPERS PRESENTED

Publications:

1. **Effects of sintering on the mechanical and ionic properties of ceria-doped scandia stabilized zirconia ceramic,** (2016) *Ceramics International*, Vol. 42(13) 14469-14474.
2. **Effect of manganese oxide on the densification and properties of ceria-doped scandia stabilized zirconia**, (2016) *Journal of Ceramic Processing Research*, Vol. 17(5), 443-447.
3. **Microwave sintering of ceria-doped scandia stabilized zirconia as electrolyte for solid oxide fuel cell**, (2016) *International Journal of Hydrogen Energy*, Vol. 41(32), 14184-14190.
4. **Effect of manganese oxide on the sinterability of 8 mol% yttria-stabilized zirconia**, (2016) *Materials Characterization*, Vol. 120, 331-336.

Conference Presentation:

- **Microwave sintering of ceria-doped scandia stabilized zirconia electrolyte for solid oxide fuel cell**, (2015) *5th International Conference of Fuel Cell and Hydrogen Technology 2015* (ICFCHT 2015).

Awards:

- **GOLD MEDAL & KASS BEST INVENTION AWARD. Rapid sintering of an ageing resistant zirconia for fuel cell and machinery applications**. *28th International Invention, Innovation & Technology Exhibition 2017 (ITEX 2017).*